UNIVERSITY OF Southampton

University of Southampton Research Repository
ePrints Soton

Copyright © and Moral Rights for this thesis are retained by the author and/or other copyright owners. A copy can be downloaded for personal non-commercial research or study, without prior permission or charge. This thesis cannot be reproduced or quoted extensively from without first obtaining permission in writing from the copyright holder/s. The content must not be changed in any way or sold commercially in any format or medium without the formal permission of the copyright holders.

When referring to this work, full bibliographic details including the author, title, awarding institution and date of the thesis must be given e.g.

AUTHOR (year of submission) "Full thesis title", University of Southampton, name of the University School or Department, PhD Thesis, pagination

http://eprints.soton.ac.uk

UNIVERSITY OF SOUTHAMPTON
FACULTY OF ENGINEERING, SCIENCE & MATHEMATICS
OPTOELECTRONICS RESEARCH CENTRE

Distributed Optical Fibre Sensors Based on the Coherent Detection of Spontaneous Brillouin Scattering

by

Mohammed Nasser Al Ahbabi

BS California University (Distinction)
MSc University of Southampton (Distinction)

Thesis submitted for the degree of Doctor of Philosophy

June 2005

UNIVERSITY OF SOUTHAMPTON

ABSTRACT

FACULTY OF ENGINEERING, SCIENCE & MATHEMATICS
OPTOELECTRONICS RESEARCH CENTRE

Doctor of Philosophy

Distributed Optical Fibre Sensors Based on the Coherent Detection of Spontaneous Brillouin Scattering

by Mohammed Nasser Al Ahbabi

This thesis reports on the progress that has been made improving the sensing performance of a distributed temperature and strain optical fibre sensor based on the coherent detection of spontaneous Brillouin scattering.

A coherent Brillouin sensor previously developed at the ORC was optically reconfigured and optimised to improve the signal to noise. The optimised sensor combined with a new microwave detection system providing high spatial resolution capabilities, was demonstrated as a temperature sensor. The system was also used to spatially resolve the Brillouin spectra in special fibres designed to suppress stimulated Brillouin scattering for use in high power fibre lasers.

In combined temperature and strain sensing, in which both the frequency and power of the Brillouin signal are spatially resolved, the accuracy achieved in both temperature and strain measurements are largely determined by the accuracy of the power measurement. As a result, alternative techniques avoiding the Brillouin power measurement were experimentally investigated and compared. Brillouin frequency and power based technique was found to provide the best results.

The sensing range is greatly dependent on input pulse energy. The pulse width is governed by the required spatial resolution and the pulse peak power is limited by the onset of nonlinear effects. The nonlinear effects were investigated and it was found that modulation instability had the lowest threshold, when using standard single mode fibre and operating in the anomalous dispersion regime. Modulation instability can be avoided by using fibres with negative dispersion at 1550nm and this was demonstrated.

To further improve the sensing range and the sensor's performance, the use of Raman amplification was investigated utilising different Raman pump configurations. Using frequency measurements only, a temperature resolution of 5 °C over a 150km sensing range with 50m spatial resolution was achieved using a counter-propagating Raman pump. Using co-propagating Raman pump the temperature resolution was 1.7 °C with 20m spatial resolution at 100km. Measuring both the power and frequency of the Brillouin signal, a simultaneous temperature and strain measurement was performed over 50km; temperature and strain resolutions of 3.5 °C and 85$\mu\varepsilon$ with 5m spatial resolution were achieved, respectively, using co-propagating Raman pump which has the advantage of requiring access to just one end of the sensing fibre.

Contents

List of Figures

List of Tables

Declaration of Authorship

I, *Mohammed N. Alahbabi*, declare that the thesis entitled
'*Distributed Optical Fibre Sensors Based on the Coherent Detection of Spontaneous Brillouin Scattering*'
and the work presented in it are my own. I confirm that:

- this work was done wholly or mainly while in candidature for a research degree at this University;
- where any part of this thesis has previously been submitted for a degree or any other qualification at this University or any other institution, this has been clearly stated;
- where I have consulted the published work of others, this is always clearly attributed;
- where I have quoted from the work of others, the source is always given. With the exception of such quotations, this thesis is entirely my own work;
- I have acknowledged all main sources of help;
- where the thesis is based on work done by myself or jointly with others, I have made clear exactly what was done by others and what I have contributed myself;
- parts of this work have been published:
  Refer to Appendix A (List of Publications).

Signed:
Date:

Acknowledgements

I would first of all like to express my sincere thanks to my supervisor Dr. Trevor Newson for his continued support and encouragement since my MSc course. His valuable discussions and suggestions have contributed greatly to the accomplishment of this work.

Special thanks go to my colleagues Nicholas P. Lawrence and Dr. Yuh Tat Cho who assisted in the lab work. I am also grateful to different members of the Optoelectronics Research Centre (ORC) for their discussions and useful feedback. These include Prof. Robert Eason, Prof. Peter Smith, Dr. Eleanor Tarbox, Dr. Xian Feng, Dr. Stuart Russell, Dr. Gilberto Brambilla, Dr. Jayanta Sahu, Dr. Alexander Boyland, Vladimir Hernandez-Solis and other members of the ORC who assisted in various capacities, especially the resources room staff. My thanks also go to Dr. Arthur Hartog and Dr. Peter Wait - (SENSA) for their contribution to one of my journal publications.

The cooperation with the following companies through my studentship is highly appreciated: CORNING OPTICAL FIBRE, SENSA and FIBRE CORE.

Last and most importantly, I would like to thank my wonderful family, including my wife and my children (Jamal, Abdulla, Sara, Fares, and Zayed) for their moral support, encouragement and patience.

Abbreviations

AOM	Acousto-optic Modulator
ASE	Amplified Spontaneous Emission
BPF	Band Pass Filter
BG	Bragg Grating
BOCDA	Brillouin Optical Correlation Domain Analysis
BOTDA	Brillouin Optical Time Domain Analysis
BOTDR	Brillouin Optical Time Domain Reflectometry
CBS	Coherent Brillouin Sensor
CD	Coherent Detection
CRN	Coherent Rayleigh Noise
CW	Continuous Wave
EDFA	Erbium Doped Fibre Amplifier
ELO	Electrical Local Oscillator
EOM	Electro-optic Modulator
ESA	Electrical Spectrum Analyzer
DD	Direct Detection
DOFS	Distributed Optical Fibre Sensors
DTS	Distributed Temperature Sensor
FUT	Fibre Under Test
FWM	Four Wave Mixing
IF	Intermediate Frequency
LEAF	Large Effective Area Fibre
LO	Local Oscillator
LPR	Landau Placzek Ratio
MCF	MetroCore Fibre
MDS	Microwave Detection System
MI	Modulation Instability
NA	Numerical Aperture
NZ-DSF	Nonzero-Dispersion Shifted Fibre
OSA	Optical Spectrum Analyzer
OTDR	Optical Time Domain Reflectometry

PC	Personal Computer
RF	Radio Frequency
RIN	Relative Intensity Noise
SBS	Stimulated Brillouin Scattering
SPM	Self-Phase Modulation
SRS	Stimulated Raman Scattering
SMF	Single Mode Fibre
WDM	Wavelength Division Multiplexer
YIG	Yttrium Iron Garnet

List of Symbols

A_{eff}	Effective core area
α_B	Brillouin scattering coefficient
α_R	Rayleigh scattering coefficient
$C_{r,b}$	Constant for SRS and SBS threshold power
c	Speed of light in vacuum
D	Dispersion parameter
h	Planck's constant
G	Modulation instability gain
g_b	Brillouin gain coefficient
g_r	Raman gain coefficient
f_a	Acoustic frequency
K_T^P	Temperature coefficient of Brillouin power
K_T^ν	Temperature coefficient of Brillouin frequency
K_ε^P	Strain coefficient of Brillouin power
K_ε^ν	Strain coefficient of Brillouin frequency
$K_{\nu T}^{P1}$	Temperature coefficient of Brillouin frequency-peak one
$K_{\nu T}^{P2}$	Temperature coefficient of Brillouin frequency-peak two
$K_{\nu\varepsilon}^{P1}$	Strain coefficient of Brillouin frequency-peak one
$K_{\nu\varepsilon}^{P2}$	Strain coefficient of Brillouin frequency-peak two
K_{RT}^P	Temperature coefficient of Raman power
$\triangle\nu$	Measured Brillouin frequency shift
$\triangle\nu_r$	Pump and Raman anti-Stokes frequency difference
$\triangle P$	Power change
$\triangle T$	Temperature change
$\triangle\varepsilon$	Strain change
$\triangle\nu^{P1}$	Frequency shift of peak one
$\triangle\nu^{P2}$	Frequency shift of peak two
$\triangle T_R$	Temperature change determined by Raman measurement
$\triangle P_R$	Change of Raman power
K	Polarisation factor

k	Boltzmann constant
L	Length of fibre
L_{eff}	Effective length
L_w	Walk-off length
P_s	Probe signal
P_p	Pump signal
P_b	Brillouin backscattered power
P_o	Launched power
P_B^{th}	SBS power threshold
P_R^{th}	SRS power threshold
P_{spm}^{th}	SPM power threshold
α	Loss coefficient
p	Photoelastic coefficient
λ	Wavelength
λ_a	Acoustic wavelength
λ_{bs}	Brillouin scattering wavelength
λ_g	Grating wavelength
λ_p	Pump wavelength
λ_s	Stokes wavelength
λ_{as}	Anti-Stokes wavelength
$\triangle\lambda$	Change of wavelength
S	Capture fraction
n	Refractive index
n_2	Nonlinear refractive index
ρ	Density of silica
β_T	Equilibrium isothermal compressibility
ϕ_{NL}	Nonlinear Phase shift
ϕ_{max}	Maximum phase shift
κ	Broadening factor
k_p	Wave number of weak perturbation
γ	Nonlinear parameter describing n_2
ν_o	Pump frequency
ν_b	Brillouin frequency shift
υ_a	Acoustic velocity
υ_g	Group velocity
β_2	Broadening parameter
δP	Power error
$\delta\nu$	Frequency error
δT	Temperature resolution
$\delta\varepsilon$	Strain resolution
$\delta\nu^{P1}$	Frequency error of peak one

$\delta\nu^{P2}$	Frequency error of peak two
ω	Frequency ($\omega = 2\pi f$)
W	Pulse width
$Sgn(x)$	(*Sgn(x) is +1 if x is positive, -1 if x is negative, and 0 if x is 0*)

Chapter 1

Introduction

1.1 Introduction and Research Objectives

Whilst the role of optical fibres in the telecommunication industry is well known, the technology has extended to another important application, such as optical fibre sensing. Owing to the properties of fibres, providing a wide range of design possibilities, Optical Fibre Sensors (OFS) have become an increasingly popular choice as reliable sensors. The advantages that these types of sensors offer are enormous, e.g. electromagnetic immunity, extremely small size, ruggedness and overall offering very high sensitivities. Distributed Optical Fibre Sensors (DOFS) perform an efficient means of obtaining multi-point measurements compared to discrete sensors. Recently, Brillouin based distributed sensors have gained increasing popularity, due to their advantages compared to Raman based sensors. Such popularity has emerged from their ability to measure both temperature and strain simultaneously and their possible use in long range sensing applications. In most sensing applications, dynamic range is one of the most important aspects, since it determines the maximum observable sensing length. However, the sensing range in spontaneous Brillouin based sensors has been limited by some factors, such as the weak nature of the Brillouin signal (∼nW), silica fibre double pass loss (∼0.40dB/km at 1550nm), nonlinear effects that limit the input power and fundamental detection noise.

The principal aim of this research into spontaneous Brillouin based temperature/strain sensors is to address such limiting factors in order to surpass previous achievements in sensing range, measurands resolution, spatial resolution and overall sensing performance, using a simplified Coherent Brillouin Sensor (CBS). The work described in this thesis is based primarily on the author's own research in collaboration and discussion with members of research groups of the ORC at the University of Southampton. Any material adopted from other sources to make this work more comprehensive is clearly referenced.

1.1.1 Thesis Outline

The thesis outline is as follows: Chapter two provides an overview and a literature review of the background to this research. A brief introduction to OTDR based distributed optical fibre sensors and their scattering mechanisms is given. The principles of Brillouin based sensors are reviewed with emphasis given to spontaneous Brillouin scattering and its detection methods. Major Brillouin sensing techniques, applications and fundamental limitations are described. The chapter concludes with a summary of recent progress in measuring distributed temperature/strain using Brillouin based sensors.

Chapter three describes the work that has been done to simplify and optimise the previously constructed CBS and its microwave detection system. Factors that limit the system's performance are investigated. The results of using the optimised microwave detection system for high spatial resolution temperature measurements and the characterisation of special fibres designed to suppress SBS are reported.

Chapter four presents the results of investigating and comparing three different techniques for measuring temperature and strain simultaneously: Brillouin frequency and power based techniques, frequency shifts of Brillouin multiple peaks and the combined spontaneous Raman and Brillouin based techniques. The relative advantages of such techniques are identified and reported.

Chapter five provides analysis of the nonlinear effects that limit the performance of spontaneous Brillouin based sensors. A brief introduction and comparison of the threshold power of stimulated Raman scattering, stimulated Brillouin scattering, self-phase

modulation, four wave mixing and modulation instability is presented. Modulation instability was found to have the lowest threshold and it is theoretically and experimentally investigated in more detail in this chapter.

Chapter six includes the results of using optical Raman amplification with the CBS to enhance the sensors's range and accuracy. Different configurations of the Raman pump were investigated and compared. Distributed temperature measurements up to 150km based on the analysis of the frequency shift, along with simultaneous temperature and strain measurements based on analysis of both the Brillouin frequency and power over a range of 50km, are also reported in this chapter.

Chapter seven summarises the research and provides recommendations for possible future work.

Chapter 2

Distributed Optical Fibre Sensors

2.1 Introduction

The unique capability of distributed optical fibre sensors allows a single length of fibre to be used as a sensing element for continuous monitoring of the measurands as opposed to an array of discrete sensors which increase the sensor's complexity and cost. This chapter outlines the principles on which DOFS are based. A literature review highlights their main characteristics with particular emphasis being given to Brillouin based optical sensors. Different types of Brillouin based sensor are briefly reviewed along with their sensing applications. The sensing principle of measuring distributed temperature/strain based on spontaneous Brillouin scattering using coherent detection is highlighted. Factors that affect the performance of Brillouin based sensors are reviewed, and the recent progress which has been made towards their realisation concludes this chapter.

2.2 Overview of Optical Fibre Sensors

The principle of operation in the ever expanding field of OFS is that the light beam is changed by the phenomenon that is being measured. The measurand can be a physical, chemical or biological parameter, and optical fibre sensors have been demonstrated for a wide range of measurements [1]. The properties of the optical signal that can be modulated are diverse, i.e. power, frequency, phase, and state of polarisation. Silica-based OFS have several advantages over other sensing technologies, the most important being:

- They can be applied under adverse environmental conditions, like strong electro magnetic fields, very high voltages, nuclear radiation, explosive media and high temperatures.
- Potentially high sensitivity over a large bandwidth and the ability to interface with a wide range of measurands in a discrete and/or distributed manner.
- Flexible geometries, allowing the design of a whole range of sensors with tremendous information carrying capacity.

The applications of OFS are numerous and have shown scientific potential and economic competitiveness with rival sensing technologies. Both discrete and distributed optical fibre sensors have been successfully demonstrated. In discrete or quasi-distributed sensing, a large number of sensing points may be used, but measurements can only be made at discrete points. On the other hand, distributed optical fibre sensors allow continuous monitoring of the measurand as a function of distance. The work in this thesis is based on a fully distributed sensor.

2.3 Principle of Distributed Optical Fibre Sensors

The concept of many distributed optical sensors operates under the powerful principle of Optical Time Domain Reflectometry (OTDR)[2]. OTDR itself is a diagnostic procedure used to measure fibre splice/loss or to locate breaks along the fibre length. In this procedure, a pulse of light is transmitted down the fibre and the Rayleigh light, which is backscattered within the numerical aperture of the fibre, is measured. The time between sending the pulse of light into the fibre and detecting the backscattered light provides a measure of the distance along the fibre. The basic components of such sensors are a light source, an optical fibre serving as a sensing element and appropriate signal processing electronics. In general, the characteristics of the pulse sources depend on the desired sensing range, spatial resolution and nonlinear thresholds. The bandwidth, sensitivity, linearity and dynamic range of the detection system are carefully selected and designed to be compatible with the pulse widths used and the levels of the backscattered light. Typically, the backscattered light is weak in nature and has a great deal of associated noise, hence some averaging and data processing is required to extract the measurand information. The length of the sensing fibre normally places a constraint on the maximum repetition rate of the laser because a second pulse is only launched after the backscattered signal from the first pulse has been collected. For example, a 100km length of fibre would limit the maximum repetition rate to 1kHz, and this would govern the time taken to average a large number of traces.

The main scattering mechanisms exploited for DOFS are Rayleigh, Raman and Brillouin scattering. In contrast to Rayleigh, there is a difference in frequency between the incident light and the scattered Raman and Brillouin light. Components which gain energy in the scattering process and therefore have a higher frequency are referred to as anti-Stokes, and those which lose energy and have lower frequency are referred to as Stokes. Figure 2.1 illustrates schematically the major scattering light spectra in silica based fibre.

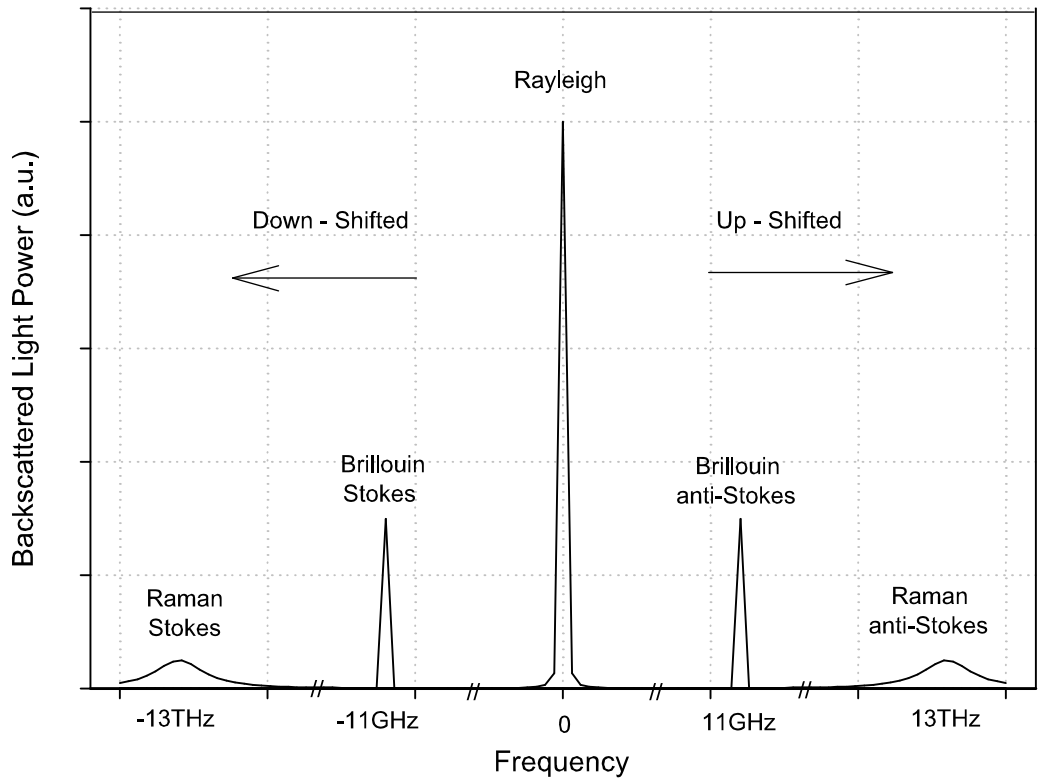

Figure 2.1: *Schematic diagram showing spontaneous light scattering spectra of Rayleigh, Brillouin and Raman in silica-based fibre at 1550nm, not drawn to scale.*

At 1550nm, the Brillouin components are ∼15dB less than the Rayleigh signal and separated from it by ∼11GHz. The Raman components are over an order of magnitude less than the Brillouin components and separated from the Rayleigh signal by about 13THz.

2.3.1 Rayleigh Scattering

Rayleigh scattering is intrinsic to the fibre material itself and is present along the entire length of the fibre. It results from random inhomogeneities in the density and compositional variations that are frozen into optical fibres during the fabrication process. These variations cause refractive index fluctuations, resulting in a fraction of the scattered light within the numerical aperture of the fibre being guided in the opposite direction to that of the incident light. Rayleigh scattering is characterised by an attenuation co-

efficient α which is proportional to λ^{-4} [3], for standard single mode fibre at 1550nm, ($\alpha \cong 4.56 \times 10^{-5} \mathrm{m}^{-1}$) equivalent to fibre loss of (~0.20dB/km). This Rayleigh scattering is the enabling mechanism for OTDR systems, which have been commercially exploited as a fibre diagnostic tool for detection of damage and fibre attenuation. However, such scattering of light in standard silica based fibre is not sensitive to factors such as temperature and strain. Figure 2.2(a) shows a schematic diagram of a typical Rayleigh scattering process in a silica fibre.

2.3.2 Raman Scattering

Inelastic scattering processes such as Raman result from the interaction between incident light and the molecular vibrational modes that exist in the molecular structure of the medium, and have an energy that can be expressed in terms of phonons [4]. In this process, the incident photon undergoes a change in energy, either losing or accepting energy; hence Raman Stokes and anti-Stokes signals are generated respectively. Figure 2.2(b) illustrates the process of Raman scattering in a silica fibre.

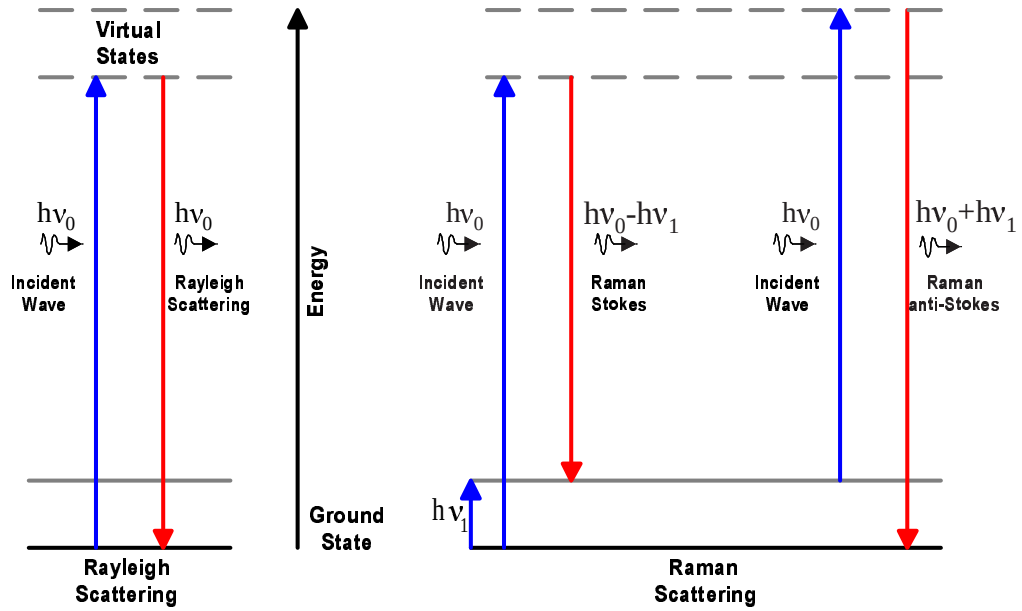

(a) *Rayleigh scattering.* (b) *Raman Stokes and anti-Stokes scattering.*

Figure 2.2: *Molecular vibration energy levels: diagram for both (a) Rayleigh (b) Raman scattering. Where ν_0 and ν_1 are the incident and shifted frequency, respectively, and h is Planck's constant.*

Raman scattering in silica glass occurs over a wide range of frequencies, due to the fact that the molecules in a glass lattice are non-crystalline in nature, leading to different vibrational energies for different groups of molecules within the glass structure. This important property of Raman scattering allows the Stokes and anti-Stokes to have a broadband nature. In fact, Raman scattering can extend over a large wavelength range, up to ∼230nm from the incident wavelength, with the peak occurring at ∼100nm [5]. In contrast to Rayleigh scattering, Raman scattering can be used to measure temperature in a distributed way. The temperature dependence of the anti-Stokes Raman signal, in particular, arises from the thermal population of the lattice vibrational energy states or phonons, where the population density of the energy levels is governed by the phonon distribution, which varies with increasing/decreasing temperature. In fact, it is this thermal sensitivity that permits the use of the ratio of anti-Stokes to the Stokes power to provide an absolute temperature measurement, as given by [3]:

$$R(T) = \left[\frac{\lambda_s}{\lambda_{as}}\right]^4 e^{-(\frac{h\Delta\nu_r}{kT})} \tag{2.1}$$

Where λ_s and λ_{as} are Raman Stokes and anti-Stokes wavelengths respectively, c is the speed of light, h is Planck's constant, $\Delta\nu_r$ is the frequency separation between the Raman anti-Stokes and pump, k is the Boltzmann constant and T is temperature in Kelvin. The sensitivity of Raman power to temperature can be obtained from equation 2.1 and is given by:

$$\frac{1}{R(T)}\frac{dR(T)}{dT} = \frac{h\Delta\nu_r}{kT^2} \tag{2.2}$$

Using equation 2.2 with $\Delta\nu_r$=13.5THz and T=293K, the percentage change in Raman power due to a temperature change K_{RT}^P is approximately 0.80%/K.

2.3.3 Brillouin Scattering

Spontaneous Brillouin scattering results from the interaction between an incoming incident light wave and thermally generated acoustic waves in the medium. It can be considered to be the diffraction of light from the refractive index variations caused by the acoustic waves. The thermally generated acoustic waves occur over a wide range of frequencies determined by discrete phonon energies. However due to the one-dimensional guiding nature of optical fibres, it is only frequencies satisfying the Bragg condition that give rise to Brillouin scattering. Figure 2.3 illustrates the process of Brillouin scattering from an acoustic wave.

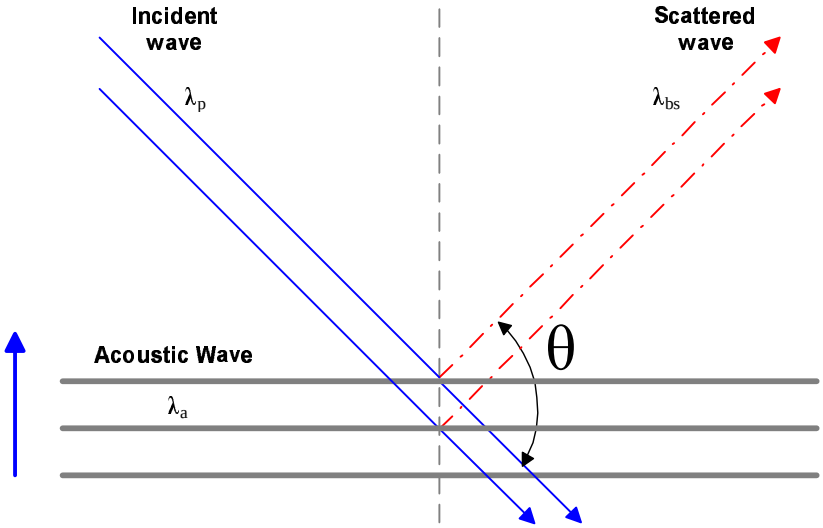

Figure 2.3: *Process of Brillouin scattering (λ_{bs}) as a result of interaction between the acoustic wave (λ_a) with incident light (λ_p).*

In fact, it is only when the incoming optical wave is phase matched to the acoustic wave that Bragg reflection occurs, satisfying equation 2.3 and resulting in spontaneous Brillouin scattering with a frequency shift that is dependent on the scattering angle. This can be seen by analyzing the Bragg diffracted wave vectors of the three involved waves shown in Figure 2.3, given by:

$$2n\lambda_a \sin\frac{\theta}{2} = \lambda_p \tag{2.3}$$

Where n is the refractive index in the fibre, λ_a is the acoustic wavelength, λ_p is the pump wavelength, θ is the angle between the incident and Brillouin scattered lights λ_{bs}

(Figure 2.3). The acoustic wave λ_a can be expressed as follows:

$$\lambda_a = \frac{\upsilon_a}{f_a} \tag{2.4}$$

Where υ_a is the acoustic velocity[1]. From equations 2.3 and 2.4 we can obtain an expression for the acoustic frequency f_a, which satisfies the Bragg condition:

$$f_a = \frac{2n}{\lambda_p}\upsilon_a \sin\frac{\theta}{2} \tag{2.5}$$

Equation 2.5 gives a quantitative value for the frequency shift experienced by the light scattered from the acoustic waves. The frequency shift depends on the velocity of the acoustic wave, the angle between the incident and scattered light and the fibre refractive index. In optical fibre, only scattering in either the forward or backward directions is guided. As a result, the acoustic frequency f_a is maximised when the light is scattered in the backward direction with respect to the direction of the incident wave, i.e. when $\theta = 180°$. The Brillouin frequency shift ν_b is equivalent to the acoustic frequency f_a, hence equation 2.5 becomes [7]:

$$\nu_b = \frac{2n}{\lambda_p}\upsilon_a \tag{2.6}$$

Using typical values for silica fibres, such as n =1.45, and υ_a = 5960m/s, pump wavelength λ_p =1550nm, the shift is approximately ∼11GHz, which makes separation of the Brillouin from the Rayleigh signal more difficult compared to the Raman scattering frequency shift ∼13THz. It is worth mentioning that, above a certain threshold power, the backscattered light experiences a rapid increase in power due to energy transfer from an incident pump beam. This scattering is no longer spontaneous, and is known as stimulated Brillouin scattering. Both stimulated and spontaneous Brillouin scattering have become the basis for the next generation of distributed temperature/strain sensors, in which Brillouin frequency and/or power are used to determine the measurands.

[1] Acoustic wave velocity in silica ≅5960 m/s [6]

For Continuous Wave (CW) light and a source with a linewidth narrower than the Brillouin signal bandwidth, the Brillouin signal of the probe, as a function of frequency ν offset from the ν_0, is typically referred to as Brillouin gain, represented by a Lorentzian shape and given by [7]:

$$g_B(\nu) = g_b \frac{(0.5\triangle\nu_b)^2}{(\nu - \nu_b)^2 + (0.5\triangle\nu_b)^2} \tag{2.7}$$

Where $\triangle\nu_b$ is Brillouin gain linewidth, typically $\simeq$35MHz in silica based fibre at 1550nm [8], ν_b is the Brillouin frequency shift given by equation 2.6 and g_b is the Brillouin gain coefficient occurring at ν=ν_b, given by [7]:

$$g_b = \frac{2\pi n^7 p^2}{c\lambda^2 \rho \upsilon_a \triangle\nu_b} \tag{2.8}$$

Where p is the average photoelastic coefficient and ρ is the material density. Using equation 2.8 with typical parameter values of fused silica fibre at 1550nm, $g_b \cong 5 \times 10^{-11}$m/W [7]. The Brillouin gain spectrum in standard SMF obtained at 1550nm is plotted in Figure 2.4 using equation 2.7.

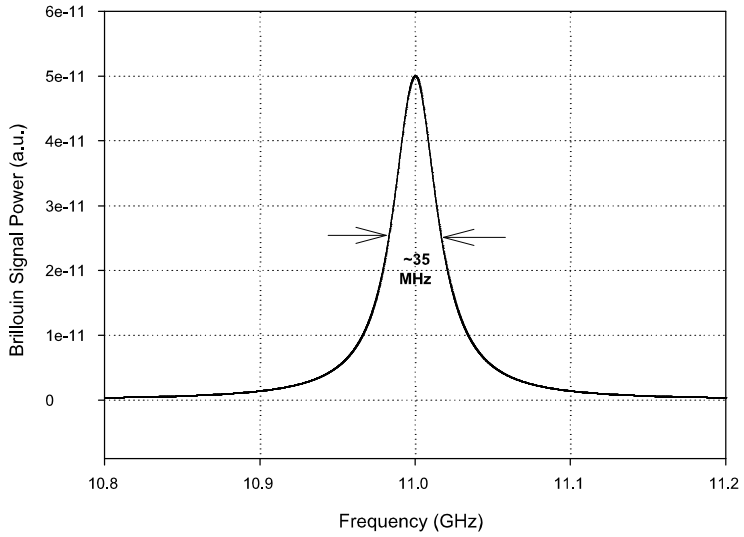

Figure 2.4: *Brillouin gain spectrum in silica based fibre at 1550nm.*

The three parameters that characterise a Brillouin gain spectrum are the Brillouin gain coefficient, Brillouin linewidth and the Brillouin frequency shift. In standard SMF, the

Brillouin spectrum has one peak with a Lorentzian function shape. Multiple peaks are found in fibres with a multi-compositional core structure [9]. The Brillouin gain coefficient, frequency shift, linewidth and power are dependent on the compositional material of the fibre and the physical influences. However, there are two fundamental parameters, namely the Brillouin frequency shift and power change that need to be considered for distributed temperature/strain measurements along the fibre. The Brillouin linewidth does not vary with strain and exhibits only a small temperature dependence ∼-0.1MHz/ °C [10], therefore it would be of limited use for temperature/strain measurements.

2.3.4 Comparison Between Brillouin and Raman Scattering for DOFS

The strong motivation for using distributed Brillouin based sensors over the more established Raman based sensors stems from the several advantages that Brillouin based sensors offer:

- Brillouin backscattered light is over an order of magnitude larger than Raman scattering; hence a longer sensing range and better sensing performance are possible.
- Brillouin based sensors allow simultaneous temperature and strain measurements along tens of kilometres of sensing range.
- The small frequency difference ∼11GHz between the Brillouin backscattered signal and its pump allows use of the low loss window (around 1550nm) and incorporation of EDFAs for optical amplification.
- Another advantage of the small frequency separation is that the ratio of Rayleigh and Brillouin backscattered light provides good compensation for splice and fibre losses and avoids the complication of measuring both fibre losses at pump and shifted frequencies, as in Raman based sensors.
- The Brillouin backscattered signal has a small gain bandwidth, hence can be recovered by an optical heterodyne detection method resulting in more convenient signal processing.

To obtain more insights into such comparisons, the following table summarises the key properties of spontaneous Brillouin and Raman scattering for silica fibre at 1550nm.

Table 2.1: *Key properties of spontaneous Brillouin and Raman scattering for silica fibre at 1550nm [7] [8][11] [12][13][14].*

Parameter Change	**Brillouin**	**Raman**
Gain bandwidth	∼20-100MHz	∼5THz
Gain coefficient	$\sim 5\times10^{-11}$m/W	$\sim 7\times10^{-14}$m/W
Frequency shift	∼11GHz	∼13THz
Scattered power weaker than Rayleigh	∼15dB	∼30dB
Power change with temperature	∼0.30%/ °C	∼0.80%/ °C
Frequency shift with temperature	∼1.1MHz/ °C	-
Power change with strain	$\sim -9 \times 10^{-4}\%/\mu\varepsilon$	-
Frequency shift with strain	~ 0.048MHz$/\mu\varepsilon$	-

Due to the small frequency difference (∼11GHz), a narrow linewidth source is needed to allow the Brillouin signal to be resolved from the Rayleigh signal, and this requires narrow and efficient optical filtering to separate the two signals. The sensitivity of Raman power to temperature is higher than Brillouin power sensitivity to temperature. However, the strength of the Brillouin signal compensates for the difference. In general, the Brillouin based sensors can provide greater sensing performance, and have proved to be of practical significance compared to Raman based sensors. The work in this thesis is based fully on Brillouin based sensors.

2.4 Brillouin Based Distributed Temperature/Strain Sensors

Brillouin based distributed optical sensors have attracted considerable research interest due to their advantages compared to Raman based sensors. This section reviews temperature/strain Brillouin based sensors in more detail, with emphasis given to spontaneous Brillouin scattering based sensors.

2.4.1 Introduction

Recently, the dependence of Brillouin power and frequency on temperature/strain has been used as the basis for distributed temperature/strain optical sensors. These dependencies resulted from the variation in the refractive index and acoustic velocity of fused silica with temperature/strain [6]. Typically there is a linear increase in refractive index with temperature and strain. However, it is the contribution from the variation in acoustic velocity that dominates Brillouin scattering. These linear dependencies enable the monitoring of temperature/strain in a wide range of sensing applications.

2.4.2 Brillouin Based Sensor Applications

Distributed optical fibre sensors based on Brillouin scattering can measure variables in a distributed way over large areas. The sensors can be used for measuring temperature, strain, fibre loss, splice/bend loss, and fibre break along a link of fibre. However, temperature and strain are the most important measurands. These qualitative measurements can be used in a large number of applications, for example:

- **Structural Monitoring:** For detecting structural cracks, such as in buildings, dams, bridges, mines, and tunnels. Structures require this kind of monitoring, as do vehicles and machines (such as aircraft, ships, high-speed trains, or space shuttles). Such measurements rely on high spatial resolution rather than long range.

- **Chemical/Processing industries:** For monitoring in nuclear power plants, electrical generators, power transformers, pressure vessels and boilers. Other applications such as power lines, oil wells and pipelines can also make use of these long range sensors.

- **Communications Networks:** For the monitoring of defects, such as loss and sudden temperature/strain rises along active transmission fibre cables, strain in submarine optical cable, earthquake damage and frozen cables.

In general, different sensing applications may require different tolerances on the sensing range, measurement response time and measurand/spatial resolutions. As a result, diversity in sensing applications has led to the need for a wide range of Brillouin sensing techniques to satisfy different sensing requirements.

2.4.3 Brillouin Based Sensing Techniques

The main regimes that are used to measure distributed temperature and strain are spontaneous Brillouin scattering and stimulated Brillouin scattering. Brillouin Optical Time Domain Reflectometry (BOTDR) [15], which in principle is similar to conventional Rayleigh OTDR, exploits spontaneous Brillouin scattering and requires access to only one end of the sensing fibre. The position of measurands in the fibre is determined by using the time interval between launching the pulsed light and observing the backscattered light; the spatial resolution is determined by the pulse width and detection bandwidth. Other techniques, such as Brillouin Optical Time Domain Analysis (BOTDA) and Brillouin Optical Correlation Domain Analysis (BOCDA), exploit stimulated Brillouin scattering and generally rely on access to both ends of the sensing fibre. Distributed sensors based on BOTDA were described by Horiguchi *et al*. in 1990 [16]. Such techniques explore the interaction between a pulse source and a counter-propagating CW source. Power is transferred between the two waves, provided their frequency difference is equal to the Brillouin shift ($\sim$11GHz). By measuring the frequency difference between the two lasers, it is possible to determine the Brillouin frequency shift as a function of either temperature or strain along the sensing fibre. The spatial information is

determined by the time delay before the pulse interacts with the CW light. The system may be operated in either the Brillouin gain mode [17], where the CW signal acts as a probe, or in the Brillouin loss mode, where the CW signal becomes the pump and amplifies the probe pulse [18]. The latter may provide a longer sensing range, due to the probe pulse being amplified. This technique has a few drawbacks. Access to both ends of the sensing fibre is necessary, which is an obvious disadvantage in many sensing applications, but more importantly it is only able to measure the Brillouin frequency shift and provides little useful information related to Brillouin power. Hence, simultaneous temperature and strain measurements at long sensing range have proven to be difficult [19]. Furthermore the measurement is dependent on an integrated Brillouin gain along the fibre, and so accurate measurements are only feasible as single hot point measurements.

In both BOTDR and BOTDA, when the pulse width is reduced to less than ∼10ns, the Brillouin spectrum becomes wider and reduces the accuracy of the Brillouin frequency shift measurement [20]. The BOCDA technique was developed to overcome such problems and to measure Brillouin frequency shift with very high spatial resolution (sub-metre) [21]. The principle of BOCDA is based on the interaction of the CW probe and pump signals along the sensing fibre. This is achieved by spatially controlling the frequency difference between the two light sources. As a result, the SBS interaction is confined to a certain position within the fibre and this position is determined by monitoring the correlation peak. The Brillouin gain is maximised where the pump and probe light is in phase and the distributed measurement is performed by varying the modulation frequency of the laser diode. This technique is only capable of measuring Brillouin frequency shift over a relatively short sensing range, i.e. tens of metres, and because it is only a frequency measurement, it is not able to separately resolve temperature and strain. It is obvious that for a single ended long range simultaneous temperature and strain measurement, BOTDR based on spontaneous Brillouin scattering is considered to be the best candidate to fill this sensing requirement.

2.4.4 Spontaneous Brillouin Based Sensors

In spontaneous Brillouin based sensors, the range and measurand resolution depends on the peak power of the pulsed source and the Brillouin SNR at the receiver. However, the maximum launched pulse power is limited by the onset of nonlinear effects in the sensing fibre. The spatial resolution in these sensors depends on the pulse width and the receiver bandwidth. The power profile of the Brillouin signal with distance is governed by the time delay between the launched probe pulse and the arrival of the backscattered signal. With the assumption that the loss experienced by the backscattered signal and the forward pulse are equal, the Brillouin power profile along a length of sensing fibre can be given as follows:

$$P_B(L) = 0.5 P_o W \alpha_B S v_g e^{(-2\alpha_R L)} \tag{2.9}$$

Where P_o is the launched probe power, W is the probe pulse width, v_g is the group velocity, α_B and α_R are the Brillouin and Rayleigh scattering coefficients, respectively. S is the capture fraction, which determines the amount of scattered light collected within the numerical aperture of the optical fibre and given by:

$$S = \frac{(NA)^2}{4n^2} \tag{2.10}$$

Where NA is the fibre numerical aperture and n is the fibre core refractive index. The Brillouin scattering coefficient can be expressed by [22]:

$$\alpha_B = \frac{8\pi^3 n^8 p^2 kT}{3\lambda_o^4 \rho v_a^2} \tag{2.11}$$

Where n is the refractive index, p is the photoelastic coefficient ($\sim$0.286), k is the Boltzmann constant (1.38×10^{-23}J/K), T is the temperature of the fibre (298K), ρ is the density of silica (2330kg/m^3), v_a is the acoustic velocity and λ_o is the incident wavelength (1550nm). Using equation 2.11 for silica based fibre, $\alpha_B \cong 1.17 \times 10^{-6}\text{m}^{-1}$. The slope of the logarithm of Brillouin power is equal to the double pass loss coefficient

(∼0.40dB/km at 1550nm), and the smallest distance between two scattering points that can be resolved represents the sampling resolution. To compensate for variations in the Brillouin power due to fluctuations in the input power or to fibre attenuation, and bend/splice loss along the sensing fibre, the measured Brillouin power trace is typically normalised by either a Brillouin trace recorded at room temperature or by the Rayleigh backscattered signal, which experiences almost the same loss as the Brillouin signal. This ratio is known as the Landau-Placzek Ratio (LPR) [12][22]:

$$LPR = \frac{P_R}{P_B} = \frac{T_f(\rho \upsilon_a^2 \beta_T - 1)}{T} \tag{2.12}$$

Where P_R and P_B are the Rayleigh and Brillouin powers, respectively. T_f is the fictive temperature (temperature at which the glass can reach the state of thermal equilibrium), and β_T is the equilibrium isothermal compressibility of the melt at the fictive temperature. Either Brillouin power change or frequency shift may be used to measure temperature/strain, provided one parameter is well defined. For absolute measurement of temperature/strain, Brillouin frequency shift measurements are typically referenced to room temperature and zero strain. The Brillouin power and frequency dependence on temperature and strain have been experimentally measured and determined to be $K_T^\nu = 1.1\text{MHz}/^\circ\text{C}$ and $K_\varepsilon^\nu = 0.048\text{MHz}/\mu\varepsilon$, which are temperature and strain coefficients governing frequency shifts, respectively [13], $K_T^P = 0.30\%/^\circ\text{C}$ and $K_\varepsilon^P = -9.03 \times 10^{-4}\%/\mu\varepsilon$ are the coefficients for power variations with respect to temperature and strain respectively [12] [14]. These coefficients are summarised in Table 2.1. Due to the linear variations of Brillouin frequency ν and power P with temperature T and strain ε respectively, the Brillouin frequency shift and power change are given by [23]:

$$\Delta\nu = K_\varepsilon^\nu \Delta\epsilon + K_T^\nu \Delta T \tag{2.13}$$

$$\Delta P = K_\varepsilon^P \Delta\epsilon + K_T^P \Delta T \tag{2.14}$$

These equations can be expressed in matrix form and if the determinant, $(K_\varepsilon^\nu K_T^P - K_\varepsilon^P K_T^\nu)$ of the matrix is non-zero (using the above values $K_\varepsilon^\nu K_T^P / K_\varepsilon^P K_T^\nu \approx$-15), then both temperature and strain can be uniquely determined from the inverse matrix, provided that both Brillouin frequency shift and power change can be adequately resolved. The temperature and strain changes are given by:

$$\triangle T = \frac{K_\varepsilon^\nu \triangle P - K_\varepsilon^P \triangle \nu}{K_\varepsilon^\nu K_T^P - K_\varepsilon^P K_T^\nu} \tag{2.15}$$

$$\triangle \varepsilon = \frac{K_T^P \triangle \nu - K_T^\nu \triangle P}{K_\varepsilon^\nu K_T^P - K_\varepsilon^P K_T^\nu} \tag{2.16}$$

The corresponding errors in the derived temperature and strain measurements are given by:

$$\delta T = \frac{\mid K_\varepsilon^P \delta\nu \mid + \mid K_\varepsilon^\nu \delta P \mid}{\mid K_\varepsilon^\nu K_T^P - K_\varepsilon^P K_T^\nu \mid} \tag{2.17}$$

$$\delta \varepsilon = \frac{\mid K_T^P \delta\nu \mid + \mid K_T^\nu \delta P \mid}{\mid K_\varepsilon^\nu K_T^P - K_\varepsilon^P K_T^\nu \mid} \tag{2.18}$$

Where $\delta\upsilon$ and δP are the measured RMS errors on the Brillouin frequency and power, respectively. The magnitude value of the determinant in equations 2.17 and 2.18 is important, since it determines the temperature and strain errors due to any errors in Brillouin frequency and power; i.e. the larger the determinant absolute value, the smaller the calculated errors. However, this determinant value may vary with different sensing fibres, since the measurand coefficients depend on the characteristics of fibres.

Due to the relatively small values of Brillouin power coefficients with temperature and strain along with the weak Brillouin signal (∼nW) and fibre double pass loss, the Brillouin frequency shift and power change need to be measured accurately; hence a detection system with high accuracy is crucial for practical long range simultaneous temperature and strain measurements.

2.4.5 Detection Methods in Spontaneous Brillouin Scattering

Two distinct detection methods used to extract temperature/strain information from the spontaneous Brillouin scattering signal are the Direct Detection (DD) and Coherent Detection (CD) methods.

2.4.5.1 Direct Detection

In the DD of spontaneous Brillouin scattering, Brillouin power is used as a basis for temperature measurement, with the assumption that strain effects on Brillouin power are negligible; therefore knowledge of the Brillouin frequency shift is not required. In such a detection method, optical filtering is typically used to separate the Brillouin from the Rayleigh backscatter signals. A stable interferometer such as Fabry-Perot [12][13] Mach-Zehnder [24] or fibre Bragg grating [25] may be used. When the Brillouin power is separated from the Rayleigh signal, the LPR is typically used to measure the absolute temperature along the sensing fibre. It is possible to measure temperature and strain simultaneously in DD using a Mach-Zehnder interferometer, where Brillouin components are positioned on the slope of the interferometer transfer function. However, the technique is limited in sensing range and accuracy [26]. It is worth mentioning that for temperature measurement only, DD has the advantages of straightforward optical electronics design, simple signal processing and relatively low cost. However, the difficulty in performing simultaneous temperature and strain measurements is considered to be a disadvantage. The CD method on the other hand offers simultaneous measurement of temperature and strain and provides longer dynamic range and better sensing performance.

2.4.5.2 Coherent Detection

In such a detection method, a heterodyne detection of spontaneous Brillouin scattering is employed to provide simultaneous measurements of Brillouin frequency shift and power change; hence temperature and strain may be separated unambiguously. This method involves mixing the backscattered signal with an optical Local Oscillator (LO), which

brings the beat frequency to within the bandwidth of a conventional heterodyne receiver [27]. Different techniques for achieving this principle have been reported, namely frequency shifted pulses using Brillouin lasers [28], where pulses are emitted at the Stokes frequency, the use of a high frequency electro-optic phase modulator driven by a mechanical generator to create 11GHz sidebands [29], and the use of an Acousto-Optic Modulator (AOM) frequency translator ring to create a tuneable frequency shift in the ∼11GHz range [15]. The best performance to date has been obtained by mixing the source used to generate the Brillouin signal with the Brillouin scattering signal. This creates a beat frequency of around ∼11GHz and can be detected and analysed using a fast optical detector and microwave electronics. The Brillouin spectrum along the sensing fibre is typically built from a number of time-domain traces measured at the desired frequency. By fitting a Lorentzian function to each spectrum, it is possible for the Brillouin frequency shift and power change to be determined at each point along the sensing fibre; hence distributed temperature and/or strain variation along the sensing fibre may be obtained. Figure 2.5 illustrates schematically typical measurand effects on a Brillouin gain spectrum spatially resolved along a sensing fibre using the CD method.

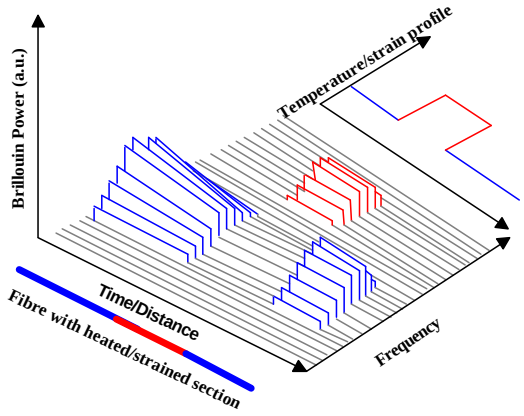

Figure 2.5: *Schematic diagram of the resulting output of the Brillouin coherent detection method.*

The CD method tends to suffer from polarisation noise and involves more electronic components compared to DD. However, it offers an improvement to the SNR in a situation where the principal noise source is detector noise. Furthermore the ∼11GHz beat signal can be far more effectively filtered electronically than can be achieved with optical filters. These factors translate to a significant improvement in sensing range and measurand resolution. It is this detection method that the thesis will investigate.

2.5 Factors Limiting the Performance of Spontaneous Brillouin Based Sensors

2.5.1 Introduction

Due to the nature of optical fibres and Brillouin scattering, spontaneous Brillouin based sensors suffer from some fundamental limitations, such as noise, weakness of Brillouin signal, fibre loss and nonlinear effects. A Brillouin signal is typically a weak signal, and the double pass loss of the fibre further reduces the signal, especially in long range sensing. Hence, noise is a major limiting factor. To strengthen the backscattered light, a high power signal needs to be launched into the fibre. However, the phenomenon of nonlinearity limits the power. This section briefly describes some of the main limitations affecting the performance in coherent detection of spontaneous Brillouin scattering based sensors, and highlights techniques to reduce their effect.

2.5.2 Noise and Fibre Loss

Noise is the undesired disturbance that masks the received signal and hence degrades the sensing system performance. In distributed optical fibre sensors based on the coherent detection of spontaneous Brillouin scattering, the noise source is typically a combination of electrical and optical noise. Thermal noise, shot noise and quantum noise are forms of electrical noise typically associated with sensor detection systems. In general, electrical noise may be reduced by signal averaging. Optical noise sources are Coherent Rayleigh Noise (CRN), Polarisation Noise, random Relative Intensity Noise (RIN) and Amplified Spontaneous Emission (ASE) noise[2]. Apart from RIN, these types of optical noise cannot be reduced by signal averaging.

[2] ASE noise occurs if optical amplifiers are employed in the sensing system.

Coherent Rayleigh noise appears as fluctuations in the Rayleigh backscatter power trace and it is a major source of noise when using a narrow linewidth source. This noise degrades measurand resolution through the Brillouin power normalisation process, i.e. LPR, and/or if there is a nonlinear contamination on the Brillouin signal by the broadened Rayleigh signal. The effect of CRN on the Rayleigh trace using two different sources is compared and shown in Figure 2.6.

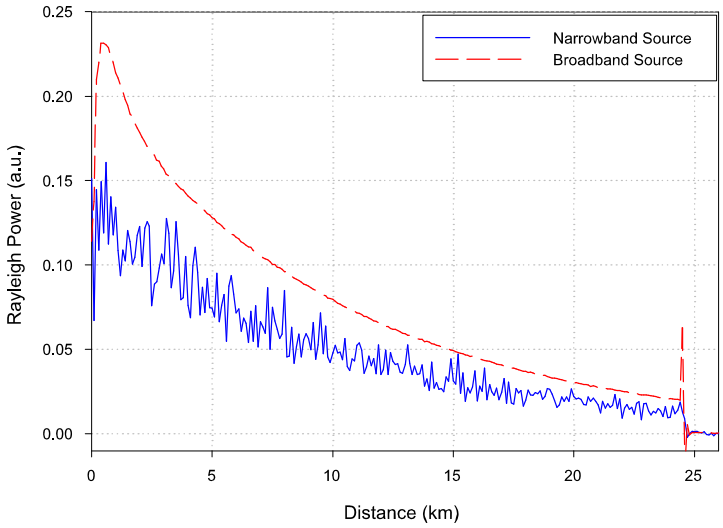

Figure 2.6: *The coherent Rayleigh noise effect on the Rayleigh trace, measured using two sources with different linewidths and powers.*

Conventional signal averaging techniques cannot be used effectively to reduce CRN. However, the use of a broadband pulse source, or averaging over a large number of different frequencies, significantly minimises the noise. This technique is called Frequency Shift Averaging (FSAV) [30].

Polarisation noise on the other hand appears as fluctuations in the Brillouin power trace if parts of the system components have polarisation dependent loss. This noise occurs in coherent detection because a standard single mode fibre has low birefringence, with poorly defined, possibly changing axes, which means that the state of polarisation is not preserved down the fibre length. As a result, there are differential changes in the state of polarisation of the Brillouin signal and of the local oscillator which cause such noise. Figure 2.7 shows the effect of polarisation noise on a Brillouin backscattered trace in two conditions, obtained using coherent detection.

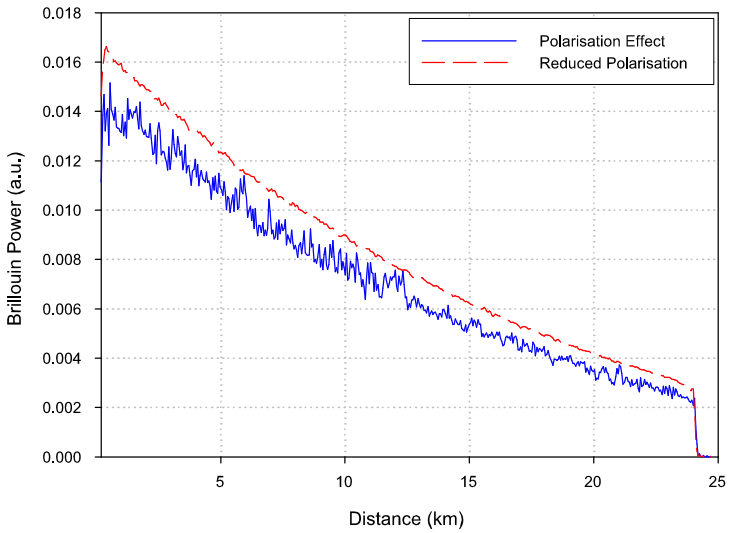

Figure 2.7: *Polarisation noise effect on Brillouin trace with/without polarisation scrambler measured at different levels of input power.*

Polarisation noise has a significant effect on measurement accuracy in CD based sensors and cannot be reduced by simple signal averaging. However, the noise may be reduced significantly by randomising the polarisation state of the light in one or both of the probe and reference sources. Using FSAV technique may also reduce the noise [31].

The RIN noise appears as random fluctuations in the output intensity of semiconductor injection lasers. Such fluctuations translate into an optical intensity noise. In a CD based sensor, RIN is assumed to mostly emanate from the optical LO, due to its high power, compared to the level of backscattered light. ASE noise occurs in sensing systems that employ EDFAs or Raman amplifiers. The need for EDFAs resulted from the fact that most narrow linewidth signal sources required for Brillouin based sensors have low output power of a few ∼mW or less. Raman amplifiers may be used in long range DOFS to amplify the weak backscattered signal (Chapter 6). Typically, the bandwidth of EDFA and Raman ASE are ∼5nm and ∼100nm, respectively. The broad signals contaminate the Brillouin signal by generating noise signals at beat frequency through various mixing processes, namely ASE beats with itself (ASE-ASE), with the local oscillator (ASE-LO), with the probe and Rayleigh signals (ASE-Signal). In general, some of the ASE noise components such as ASE-ASE may be reduced by employing narrow bandwidth optical filters such as the Bragg gratings. The ASE-probe beat noise cannot be reduced by narrow-band filtering and, in this sense, is inherent to optical amplifiers.

The total measurement time depends on the time taken to collect or process a single trace, multiplied by the number of averages required to achieve the required SNR. Typically there is a trade-off between the data averaging time and sensor performance, which depends greatly on the type of sensing application. However, high repetition rates and fast data acquisition systems reduce measurement time significantly. Due to the need for optical amplification at both the transmission and receiving ends of the fibre sensor, and to make use of the low loss window, the chosen wavelength is typically optimised for the third window (1550nm). However, even when operating at this wavelength, round trip fibre loss (∼0.40dB/km) is unavoidable. For example, for 100km sensing fibre, the Brillouin signal is reduced by around 40dB. Fibre loss is therefore a major factor limiting the sensing range. In Chapter 6, a new Raman amplification technique to help overcome this limitation is described.

2.5.3 Nonlinear Effects

In a BOTDR based distributed fibre sensor, the backscattered signal is proportional to the pulse energy within the sensing fibre. The pulse energy depends on the pulse width and peak power. However, the desired spatial resolution limits the pulse width. In spite of the availability of high peak power sources, the maximum peak power that can be launched is limited by the need to avoid nonlinear effects. Above a certain power threshold, nonlinear effects distort the backscattered traces, either directly or via changes in pump depletion and/or probe spectral broadening. Such distortions produce errors in measurements. The main nonlinear effects that need consideration are Stimulated Raman Scattering (SRS), Stimulated Brillouin Scattering (SBS), Self-Phase Modulation (SPM), Four Wave Mixing (FWM), and Modulation Instability (MI). The signal limitations these nonlinear effects have on sensing performance are investigated in more detail in Chapter 5.

2.6 Recent Progress in Brillouin Based Distributed Temperature/Strain Sensors

A great deal of research effort has focused on simplifying and improving the performance of Brillouin based distributed temperature/strain sensors. In the last 15 years or so, different techniques and methods have resulted in significant improvement in sensing range, spatial resolution and measurand resolution. The techniques and corresponding results were previously reviewed in some detail by Maughan [32] and more recently by Cho [33]. The key results for both long sensing range and short sensing range combined with high spatial resolution using the three main Brillouin sensing techniques (described in 2.4.3) are highlighted in the following section:

The longest temperature sensing range was achieved using BOTDR, based on Brillouin frequency shift measurements [27]. For simultaneous measurement of temperature and strain, the best result was obtained by measuring simultaneously the spontaneous Brillouin frequency shift and power change based on the BOTDR technique [34]. In the BOTDA technique, which is based only on the measurement of the Brillouin frequency shift and requires access to both ends of the sensing fibre, it was claimed that a temperature resolution of 1 °C with spatial resolution of 5m over a range of 32km was achieved [35], but this result is based on the assumption that only one portion of the fibre is heated. For a short range with very high spatial resolution, the best result was obtained using BOCDA. In BOCDA, the research focussed on improving the accuracy with which the Brillouin frequency shift could be measured for applications, such as monitoring civil structures or chemical plants, which require short sensing lengths and high spatial resolution (<1m). Recent results in this respect were obtained by Hotate [36]. Table 2.2 summarises the key results in both short and long range distributed temperature/strain Brillouin based sensors.

Table 2.2: *Key results and progress in Brillouin based sensing since 1990.*

Year	**Technique**	**Temperature** (^{o}C)	**Strain** ($\mu\varepsilon$)	**Spatial Resolution** (m)	**Sensing Range** (km)	**Ref.**
1999	BOTDR (Frequency)	3	-	20	57	[27]
1999	BOTDR (Frequency and Power)	4	100	20	30	[34]
1993	BOTDA (Frequency)	1	-	5	32	[35]
2001	BOCDA (Frequency)	-	70	0.04	8.0×10^{-3}	[37]

From Table 2.2, it can be seen that the longest sensing range of single or combined measurands was obtained using the BOTDR based sensor. However, these measurements are limited in spatial resolution. BOTDA technique has demonstrated a limited sensing range and only one measurand can be measured at one time. Current BOCDA technique is also limited to a single measurand with very short sensing range. As a result, it is difficult to achieve long range simultaneous temperature and strain measurements using BOTDA and BOCDA techniques.

It is the aim of this work to reduce the effect of factors that still limit BOTDR sensing performance, in order to surpass current results with respect to sensing range, measurands and spatial resolution, and overall sensing performance, which may lead to long range distributed temperature/strain sensors of competitive commercial value.

2.7 Conclusions

Due to their unique advantages, OFS have become an increasing popular choice compared to other sensing technologies. The scattering mechanisms in the optical fibre allow DOFS to be used efficiently in a large number of sensing applications. Due to the strength of Brillouin signal and sensitivity to both temperature and strain, Brillouin based sensors have gained popularity over Raman based sensors. The coherent detection of spontaneous Brillouin scattering provides higher dynamic range, simultaneous measurement of temperature and strain and better sensing performance compared to direct detection. The investigation reported in this thesis is confined to a distributed optical fibre sensor for measuring temperature and strain using coherent detection of spontaneous Brillouin signal, subsequently referred to as either the Coherent Brillouin Sensor (CBS) or simply the sensor. It is the principal aim of this work to address factors that limit the sensor performance such as noise, fibre loss and nonlinear effects. The next chapters report on optimisation and sensing improvements achieved during the course of this research.

Bibliography

[1] A. J. Rogers, Ed., *Application of Optical Fiber Sensors: Technical and Market Trends*, ser. Proceedings of SPIE, vol. 4074, no. 2, May 2000.

[2] M. K. Barnoski and S. M. Jensen, "Fiber Waveguides: A Novel Technique for Investigating Attenuation Characteristics," *Applied Optics*, vol. 15, p. 2112, September 1976.

[3] J. Wilson and J. Hawkes, *Optoelectronics an Introduction*, 3rd ed. Prentice Hall, 1998.

[4] H. P. Myers, *Introductory Solid State Physics*. Taylor and Francis Ltd., 1990.

[5] F. L. Galeener, J. C. Mikkelsen, Jr., R. H. Geils and W. J. Mosby, "The Relative Raman Cross Sections of Vitreous SiO_2, GeO_2, B_2O_3 and P_2O_5," *Applied Physics Letters*, vol. 32, no. 1, p. 34, January 1978.

[6] N. P. Bansal and R. H. Doremus, *Handbook of Glass Properties*. Academic Press, 1986.

[7] G. P. Agrawal, *Nonlinear Fiber Optics*, 2nd ed. Academic Press, 1995.

[8] T. Horiguchi, K. Shimizu, T. Kurashima, M. Tateda, and Y. Koyamda, "Development of a Distributed Sensing Technique using Brillouin Scattering," *IEEE Journal of Lightwave Technology*, vol. 13, no. 7, p. 1269, July 1995.

[9] N. Shibata, Y. Azuma, T. Horiguchi and M. Tateda, "Identification of Longitudinal Acoustic Modes Guided in the Core Region of a Singlemode Optical Fiber by Brillouin Gain Spectra Measurements," *Optics Letters*, vol. 13, no. 7, p. 595, July 1988.

[10] T. Kurashima, T. Horiguchi and M. Tateda, "Thermal Effects of Brillouin Gain Spectra in Single Mode Fibers," *IEEE Photonics Technology Letters*, vol. 2, no. 10, p. 718, October 1990.

[11] P. C. Wait, K. De. Souza, T. P. Newson, "A Theoretical Comparison of Spontaneous Raman and Brillouin Based Fibre Optic Distributed Temperature Sensors," *Optics Communications*, vol. 144, no. 1-3, p. 17, December 1997.

[12] P. C. Wait and T. P. Newson, "Landau Plazcek Ratio Applied to Distributed Fibre Sensing," *Optics Communications*, vol. 122, p. 141, Jun 1996.

[13] T. R. Parker, M. Farhadiroushan, V. A. Handerek and A. J. Rogers, "A Fully Distributed Simultaneous Strain and Temperature Sensor Using Spontaneous Brillouin Backscatter," *IEEE Photonics Technology Letters*, vol. 9, no. 7, p. 979, July 1997.

[14] K. D. Souza, P. C. Wait and T. P. Newson, "Characterisation of Strain Dependence of the Landau-Placzek Ratio for Distributed Sensing," *Electronics Letters*, vol. 33, no. 7, p. 615, March 1997.

[15] K. Shimizu, T. Horiguchi, Y. Koyamada and T. Kurashima, "Coherent Self-Heterodyne Detection of Spontaneously Brillouin-Scattered Light Waves in a Single-Mode Fiber," *Optics Letters*, vol. 18, no. 3, p. 185, February 1993.

[16] T. Kurashima, T. Horiguchi and M. Tateda, "Distributed-temperature Sensing using Stimulated Brillouin Scattering in Optical Silica Fibers," *Journal of Lightwave Technology*, vol. 7, no. 8, p. 1170, August 1989.

[17] T. Horiguchi, T. Kurahima and M. Tateda, "A Technique to Measure Distributed Strain in Optical Fibers," *IEEE Photonics Technology Letters*, vol. 2, no. 5, p. 352, May 1990.

[18] X. Bao, D. J. Webb and D. A. Jackson, "22 km Distributed Temperature Sensor Using Brillouin Gain in an Optical Fiber," *Optics Letters*, vol. 18, no. 7, p. 552, April 1993.

[19] J. Smith, A. Brown, M. DeMerchant and X. Bao, "Simultaneous Distributed Strain and Temperature Measurement," *Applied Optics*, vol. 38, no. 25, p. 5372, September 1999.

[20] A. Fellay, L. Thevenaz, M. Facchini, M. Nikles and P. Robert, "Distributed Sensing Using Stimulated Brillouin Scattering: Towards Ultimate Resolution," *12th International Conference on Optical Fiber Sensors Technical Digest (OFS)*, vol. 16, p. 324, October 1997.

[21] K. Hotate and S.S.L. Ong, "Distributed Dynamic Strain Measurement Using a Correlation-Based Brillouin Sensing System," *IEEE Photonics Technology Letters*, vol. 15, no. 2, p. 272, February 2003.

[22] J. Schroeder, R. Mohr, P.B. Macedo and C.J. Montrose, "Rayleigh and Brillouin Scattering in K_2O-SiO_2 Glasses," *Journal of the American Ceramic Society*, vol. 56, no. 10, p. 510, October 1973.

[23] J. D. C. Jones, "Review of Fibre Sensor Techniques for Temperature-Strain Discrimination," *12th International Conference on Optical Fiber Sensors Technical Digest (OFS)*, vol. 16, p. 36, October 1997.

[24] K. D. Souza, P. C. Wait and T. P. Newson, "Double-Pass Configured Mach-Zehnder Interferometer Optical Filter for Distributed Fibre Sensing," *Electronics Letters*, vol. 33, no. 25, p. 2148, December 1997.

[25] P. C. Wait and A. H. Hartog, "Spontaneous Brillouin-Based Distributed Temperature Sensor Utilizing a Fiber Bragg Grating Notch Filter for the Separation of the Brillouin Signal," *IEEE Photonics Technology Letters*, vol. 13, no. 5, p. 508, May 2001.

[26] H. H. Kee, G. P. Lees and T. P. Newson, "All Fiber System for Simultaneous Interrogation of Distributed Strain and Temperature Sensing by Spontaneous Brillouin Scattering," *Optics Letters*, vol. 25, no. 10, p. 695, May 2000.

[27] S. M. Maughan, H. H. Kee and T. P. Newson, "57 km Single-ended Spontaneous Brillouin-Based Distributed Fiber Temperature Sensor Using Microwave Coherent Detection," *Optics Letters*, vol. 26, no. 6, p. 331, March 2001.

[28] V. Lecoeuche, M.W. Hathaway, D. J. Webb, C. N. Pannell and D. A. Jackson, "25 km Brillouin-based Single-ended Distributed Fibre Sensor for Threshold Detection of Temperature or Strain," *Optics Communications*, vol. 168, no. 1-4, p. 95, Septemper 1999.

[29] H. Izumita, T. Sato, M. Tateda and Y. Koyamada, "Brillouin OTDR Employing Optical Frequency Shifter using Side-Band Generation Technique With High-Speed LN Phase Modulator," *IEEE Photonics Technology Letters*, vol. 8, no. 2, p. 1674, December 1996.

[30] K. Shimizu, T. Horiguchi and Y. Koyamada, "Characteristics and Reduction of Coherent Fading Noise in Rayleigh Backscattering Measurement for Optical Fibers and Components," *IEEE Journal of Lightwave Technology*, vol. 10, no. 7, p. 982, July 1992.

[31] J. P. King, D. F. Smith, K. Richards, P. Timson, R. E. Epworth and S. Wright, "Development of a Coherent OTDR Instrument," *Journal of Lightwave Technology*, vol. LT-5, no. 4, p. 616, April 1987.

[32] S. M. Maughan, "Distributed Fibre Sensing using Microwave Heterodyne Detection of Spontaneous Brillouin Backscatter," PhD Thesis, University of Southampton, 2001.

[33] Y. T. Cho, "An Investigation into Using Optical Amplifiers for Enhancing Brillouin Based Optical Time Domain Reflectometry," PhD Thesis, University of Southampton, 2004.

[34] S. M. Maughan, H. H. Kee and T. P. Newson, "Simultaneous Distributed Fibre Temperature and Strain Sensor using Microwave Coherent Detection of Spontaneous Brillouin Backscatter," *Measurement Science and Technology*, vol. 12, p. 834, February 2001.

[35] X. Bao, D. J. Webb and D. A. Jackson, "32 km Distributed Temperature Sensor Based on Brillouin Loss in an Optical Fiber," *Optics Letters*, vol. 18, no. 18, p. 1561, September 1993.

[36] K. Hotate and M. Tanaka, "Distributed Fiber Brillouin Strain Sensing With 1 cm Resolution by Correlation-Based Continuous Wave Technique," *IEEE Photonics Technology Letters*, vol. 14, no. 2, p. 179, February 2002.

[37] K. Hotate and M. Tanaka., "Enlargement of Measurement Range of Optical-Fiber Brillouin Distributed Strain Sensor Using Correlation-Based Continuous-Wave Technique," *Conference of Lasers and Electro-Optics Technical Digest (CLEO)*, p. 119, May 2001.

Chapter 3

Optimising the Coherent Brillouin Sensor

3.1 Introduction

For long range Brillouin based distributed optical sensors, maximising the weak Brillouin backscattered light is crucial, since it determines sensing range and accuracy. The coherent Brillouin sensor initially constructed at the University of Southampton was reconfigured and optimised for longer range and better sensing performance. This chapter describes the optimisation and improvements that have been made to the sensor. It also reports on the demonstration of a new Microwave Detection System (MDS) for high spatial resolution temperature measurement and its usage in characterising special fibres designed to suppress SBS in high power fibre laser systems.

3.2 Sensor Reconfiguration and Improvements

3.2.1 Previous System Set-up and Limitations

Prior to this research, the University employed a method of optically heterodyning the Brillouin backscattered signal using a commercially available Electrical Spectrum Analyzer (ESA). Figure 3.1 illustrates the previous Brillouin coherent sensor [1][2].

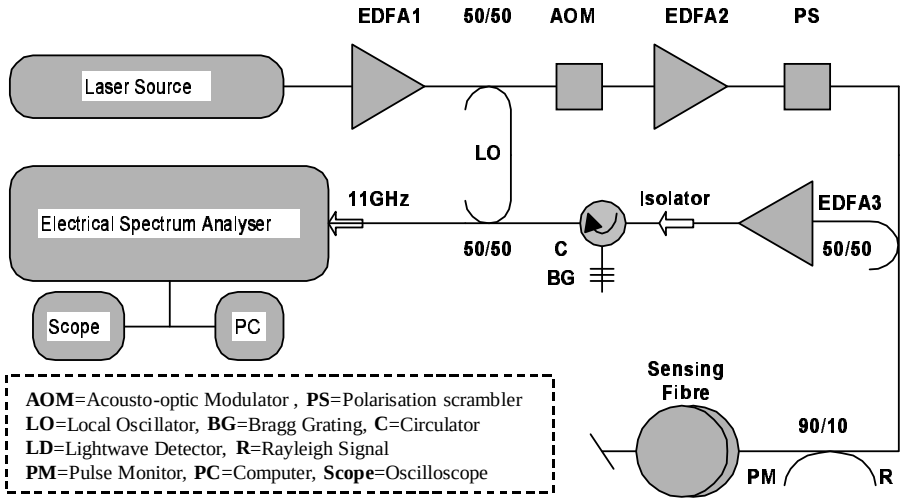

Figure 3.1: *Block diagram of the previous coherent Brillouin sensor.*

The sensor's experimental set-up and principle of operation can be summarised as follows: The light source was a tuneable laser at 1533.2nm, with ∼1MHz linewidth, and up to 100μW CW output power. Two EDFAs and an AOM were used to generate a probe pulse, which was launched into the sensing fibre. EDFA3 was used to amplify the weak backscattered signal, generated in the sensing fibre, prior to mixing it with the optical LO. The Bragg grating (*reflectivity = 99.4%,* $\triangle\lambda_g$ *= 0.12nm,* λ_g *= 1533.11nm*) filtered the Brillouin anti-Stokes signal from the Rayleigh signal. A 90/10 fibre coupler was used as a 10% tap of the probe pulse for pulse monitoring (PM), which was used as a diagnostic for the system output power and pulse width. The other arm of the coupler was used to enable direct detection of the Rayleigh backscattered signal (R) for Brillouin power trace normalisation. A 20GHz lightwave detector and an ESA allowed the collection of time-domain traces centred at the desired RF frequencies. The Brillouin spectrum along the sensing fibre was built from the measured traces and, by fitting a Lorentzian function to each spectrum, the Brillouin frequency shift and power

change were computed from the fitted curve. The temperature/strain change along the sensing fibre was determined by analyzing the frequency shift and power change of the anti-Stokes Brillouin backscatter signal. Analysis of the sensor set-up (Figure 3.1) revealed that the sensor could be further optimised by reducing the number of optical components and implementing more efficient data processing.

3.2.2 Optimised Sensor Set-up and Improvements

A schematic diagram of the reconfigured sensor is shown in Figure 3.2 and the key changes are summarised.

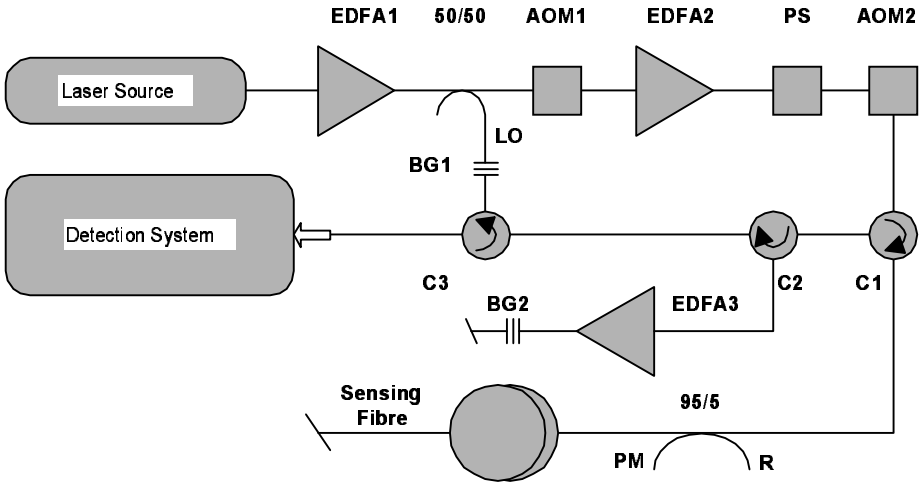

Figure 3.2: *Optimised coherent Brillouin sensor set-up.*

Important changes to the previous sensor include:

- A three port circulator C1 was employed instead of the 3dB coupler.
- An additional AOM2 was used to gate the ASE generated by EDFA2 (see figure 3.4).
- The backscattered signal was further amplified by employing a double pass amplification (EDFA3) where BG2 (*reflectivity = 99.4%,* $\triangle\lambda_g$ *= 1nm,* λ_g *= 1533nm*) filters much of ASE generated in the first pass. Up to ∼3dB improvement was obtained compared to the single pass, with no sign of signal distortion by ASE noise.

- The isolator used in the previous sensor was removed, as it was redundant as a result of the use of the circulator. The 90/10 coupler was replaced by a 95/5 coupler to increase the Brillouin backscattered light; hence more than 2dB improvement on the Brillouin backscattered power was obtained.

- A more efficient mixing technique was used, in which the optical LO is mixed with the anti-Stokes Brillouin signal by allowing it to pass through the Bragg grating (BG1) that filters the Rayleigh signal.

The following schematic diagram illustrates in detail the mixing principle using BG1.

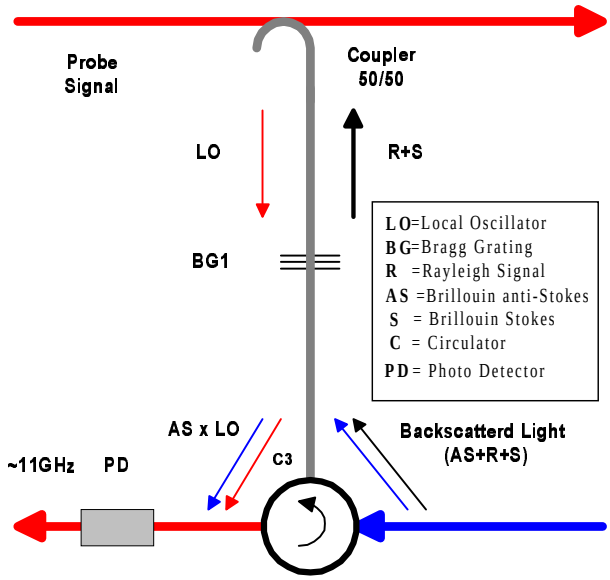

Figure 3.3: *Local oscillator signal and Brillouin anti-Stokes mixing principle via the Bragg grating (BG1).*

The principle of this mixing technique is that the optical LO at 1533.2nm is transmitted through the Bragg grating (BG1) (*reflectivity = 99.4%,* $\triangle\lambda_g$ *= 0.12nm,* λ_g *= 1533.11nm*) at the output arm of the (50/50) coupler. The backscattered light, which includes Rayleigh and both Brillouin Stokes and anti-Stokes signal, is routed by C3 towards the BG1. BG1 allows the Brillouin Stokes at 1533.28nm and the Rayleigh signal at 1533.2nm to be transmitted, whilst reflecting the Brillouin anti-Stokes at 1533.11nm back towards the circulator, which now shares a common path with the optical LO and is mixed on the face of the photodetector. This efficient mixing and filtering avoids the 3dB loss present in the previous sensor (Figure 3.1).

Figure 3.4 illustrates the effect of using AOM2 to gate the ASE generated by EDFA2.

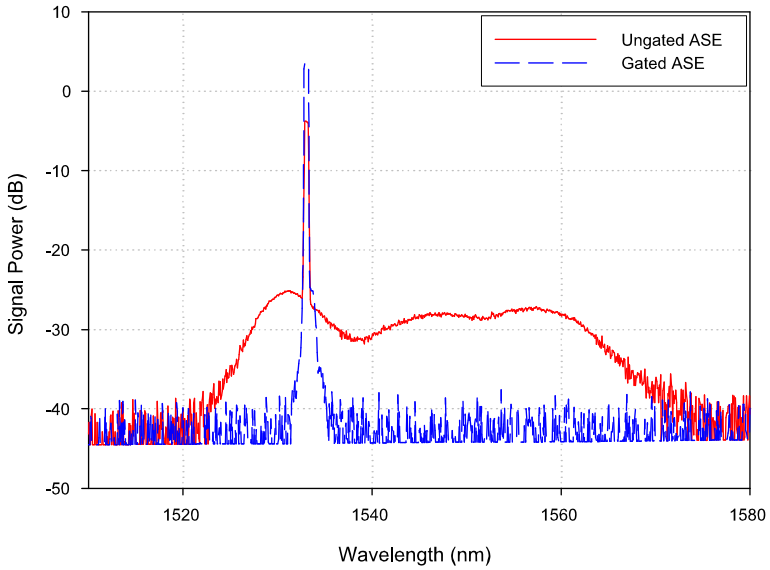

Figure 3.4: *ASE signal with/without AOM gating technique measured at the output of the CBS.*

In the previous sensor, the ASE signal generated by EDFA2 was launched alongside the probe signal into the sensing fibre, hence inducing noise on the Brillouin backscattered light. However, by employing the gating technique, the ASE signal was suppressed by around 20dB, as can be seen in Figure 3.4. A preliminary investigation of the optimised sensor noise revealed that the ASE signal produced by the preamplifier EDFA3 (Figure 3.2) made a significant contribution to such noise. In this case, the ASE beat with itself or with other signals, producing noise at ∼11GHz, hence overlapping with the Brillouin signal and reducing SNR. At present, the BG1 has a filtering bandwidth of ∼15GHz. However, ∼2GHz will be more than enough to measure Brillouin frequency shifts in practical sensing applications, hence more than 8dB improvement is possible if a stable BPF with ∼2GHz bandwidth is used. The second ASE noise signal was identified to be the ASE coming from the optical LO produced by EDFA1. This noise signal is relatively small compared to the preamplifier ASE noise, and can be reduced significantly by employing optical filtering as well.

Overall improvement on the Brillouin backscattered optical power was achieved as a result of this new reconfiguration compared to the previous sensor, as summarised in Table 3.1.

Table 3.1: *Overall improvement in Brillouin backscattered power as a result of optimising CBS.*

Changes made to the sensor	**Brillouin power improvements**
Using C1 instead of 3dB coupler	*2dB*
Single to double pass preamplification	*3dB*
New coupling ratio/isolator removal	*2dB*
Mixing using BG1 instead of 3dB coupler	*2dB*
Total improvement	**9dB**

The optical backscattered power was improved by around 9dB as a result of the CBS reconfigurations and optimisation, which is equivalent to round 23km improvement on sensing range. The ASE noise generated from EDFA2 was also significantly reduced through the gating process. To further improve CBS performance, its data processing techniques were investigated, as reported in the next section.

3.3 Data Processing Considerations for the Coherent Brillouin Sensor

In order to gain further insight into the performance of the coherent Brillouin sensor, a brief investigation of its data processing was carried out, as reported in this section. The aim was to identify the various factors that affect the sensor's performance. Factors considered were the curve fitting routines used, the choice of frequency range/spacing and the overall measurement time.

3.3.1 Spectral Curve Fitting and Brillouin Power Measurement

In the coherent detection technique, the distributed Brillouin spectrum is built from a number of time-domain traces measured over the frequency of interest (Figure 2.5). Since the spontaneous Brillouin spectrum is known to have Lorentzian shape, a Lorentzian curve is fitted to each spectrum. For this purpose, the Levenberg-Marquardt nonlinear least squares algorithm was used [3]. After the fitting process, the centre frequency, peak power, linewidth and area under the curve are determined from the Lorentzian spectral profile and used to extract measurand information. However, at certain points along the sensing fibre, where frequency shift changes over a distance smaller than the spatial resolution, a double or even triple Lorentzian peak is needed. The Brillouin power at each point along the sensing fibre may be extracted from the recorded spectra using several methods, for example, by multiplying the Lorentzian peak power by its linewidth, or alternatively by summing all spectral components over the frequency range, since the total power is proportional to the area under the curve for Lorentzian fit. However, the latter method may induce some error, if part of the Brillouin spectrum lies outside the scanned frequency range. Using the product of Brillouin linewidth and peak has the disadvantage that it cannot be implemented in situations where there is significant variation in temperature/strain within the pulse width. If, for example, there were a step change in temperature/strain, two peaks would emerge. The method of summation of all spectral components can be applied without Lorentzian fit, hence overcoming the problem of multiple peaks. This method may give more accurate measurement of the

Brillouin power if adequate frequency range and suitable frequency step are used. In fact, the choice of frequency range and spacing are crucial to the accuracy of the fitting process, and hence the measurands' resolution. The summation method will be used in subsequent measurements.

3.3.2 Choice of Frequency Range and Step

Brillouin frequency/power measurements require the Brillouin spectrum to be measured over a particular frequency span, which mainly depends on sensing applications. For example, a 100 °C change in temperature or 2000$\mu\varepsilon$ strain shifts the Brillouin frequency by around 100MHz. Therefore the intended range of frequencies needs to be estimated carefully in order to avoid collecting time-domain traces of unnecessary frequencies or underestimating the range which would lead to poor curve fitting. For the above example, a frequency range of ∼300MHz provides good accuracy of Lorentzian fit. Another factor that needs to be considered is the frequency step[1], where the bandwidth of the detection system and the required measurement resolution determine the appropriate interval frequency. It was verified experimentally that with larger frequency spacing, the measurement time is significantly reduced. However, a large amount of trace averaging is required to achieve the same measurand resolution as that obtained with smaller frequency steps. Based on such finding, a frequency step of 10MHz was chosen, a compromise between smaller quantity of data and measurement time. This step frequency is used in the subsequent measurements.

3.3.3 Measurement Time Considerations

The total measurement time depends on the frequency range, the frequency step, number of averages, sensing fibre length and the data acquisition system. For example, if the optimum frequency range and step are 300MHz and 10MHz respectively, then 30 time-domain traces need to be measured. Each time-domain trace is averaged 4096 times, as this is relatively easily achieved with the oscilloscope used, and takes around 50s. Transfer time to PC takes a further 2s. Total measurement time is therefore (52s x

[1]Frequency interval between consecutive measured frequencies.

30) or ∼26 minutes. Although an oscilloscope is a convenient means to achieve the averaging, faster data processing boards exist, and the time taken for collecting each trace approaches the theoretical limit governed by the transit time of the pulse. For example, for a 100km sensing range, the round trip time is 1ms, so 4096 averages can be achieved in less than 5s (ten times faster than with the oscilloscope).

3.4 Microwave Detection System for the Coherent Brillouin Sensor

This section describes a new microwave detection system designed to overcome the spatial resolution limit imposed by the ESA. The system reveals itself to be a high spatial resolution distributed temperature sensor. It is also used to characterise special fibres designed and fabricated at the ORC which exhibit much higher SBS thresholds for use in high power fibre laser systems.

3.4.1 Introduction

In the previous CBS, the highest spatial resolution obtained was about 20m and was limited by ESA [1][4]. The present application for monitoring temperature in power cables required a spatial resolution up to ∼1m. Other potential applications of the system are to monitor strain with similar spatial resolution or higher in large scale structures, i.e. dams, bridges, tunnels and buildings. To achieve such spatial resolution requires an ESA with a higher video bandwidth and a broader resolution bandwidth than was previously available, at an economic price. The majority of ESAs are designed to maximise the frequency resolution capability, i.e. have narrow resolution bandwidth, operate at relatively low-intermediate frequencies (IF) and have correspondingly low video bandwidths leading to poor spatial resolution. As a result, a new microwave detection system was designed [2] to overcome the spatial resolution limitations imposed by ESAs.

3.4.2 Principle of Operation

In the CBS in Figure 3.2, a single laser is used both as a source for generating the probe pulse and as an optical LO. The generated beat signal is around 11GHz, corresponding to the Brillouin frequency shift. This signal is further downshifted using the microwave detection system. Figure 3.5 illustrates schematically the microwave detection system's components and set-up.

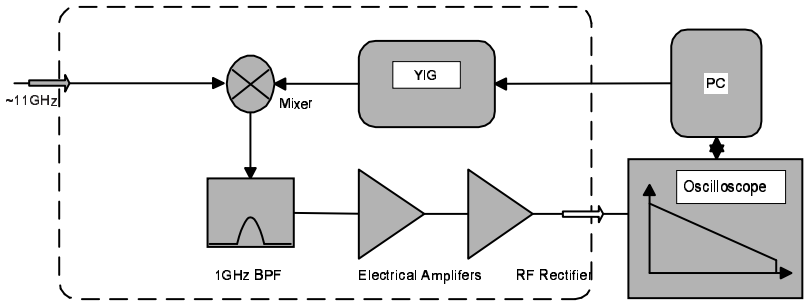

Figure 3.5: *Block diagram of the microwave detection system.*

The 11GHz signal was mixed with a PC controlled ∼10dBm Yttrium Iron Garnet (YIG) based Electrical Local Oscillator (ELO) and passed through a BPF centred at 1GHz, with a bandwidth of ∼50MHz to generate an IF of 1GHz. The ELO was scanned through a range of frequencies in user-defined frequency steps. The selected frequency of the ELO determined the portion of the Brillouin beat frequency spectrum that was measured: i.e. the measured component of the Brillouin beat frequency was equal to the ELO frequency plus the 1GHz IF, plus/minus the frequency induced by the AOMs. The IF was amplified and then rectified using a microwave diode rectifier and fed into a storage oscilloscope. The signal recorded was proportional to the Brillouin power at the chosen frequency over the bandwidth determined by BPF. Figure 3.6 illustrates the 1GHz BPF transmission window along with the downshifted Brillouin signal.

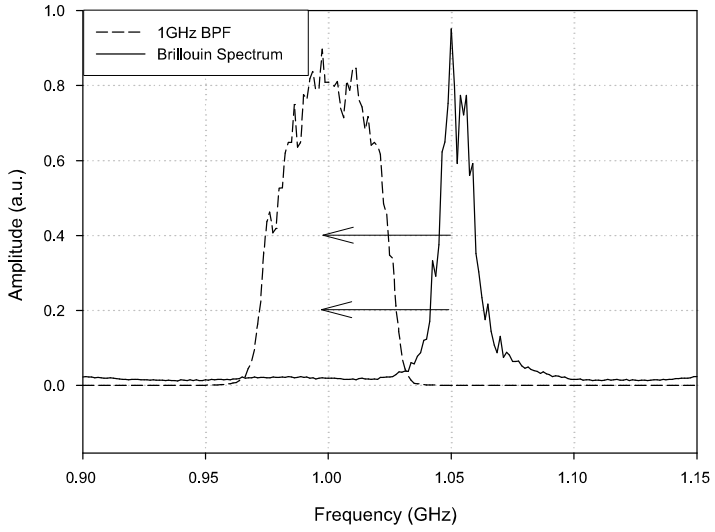

Figure 3.6: *Transmission window (∼50MHz) of the 1GHz BPF and the downshifted Brillouin spectrum.*

The downshifted Brillouin spectrum was generated from a SMF at room temperature. As the ELO frequency is increased, the filter transmission window scans the Brillouin signal, and a time-domain trace over the frequency of interest is measured. The oscilloscope was used to average a large number of time-domain traces that were then transferred to the PC. The Brillouin spectra were built by collecting such traces over a range of frequencies. The Brillouin frequency shifts and Brillouin power change were then extracted from the collected data and hence the temperature/strain change was spatially resolved.

A 3dB attenuator had previously been used at the input to the ESA to provide the required DC path. This was no longer required in this system. Optical beat noise generated around 9GHz was also mixed with the YIG signal, hence added to the electrical signal output at the 1GHz IF frequency. This was prevented by adding an RF notch filter at 9GHz with a 1GHz bandwidth prior to the mixer, as suggested by Dr. Peter Wait[2]. This improvement on the SNR is illustrated in Figure 3.7.

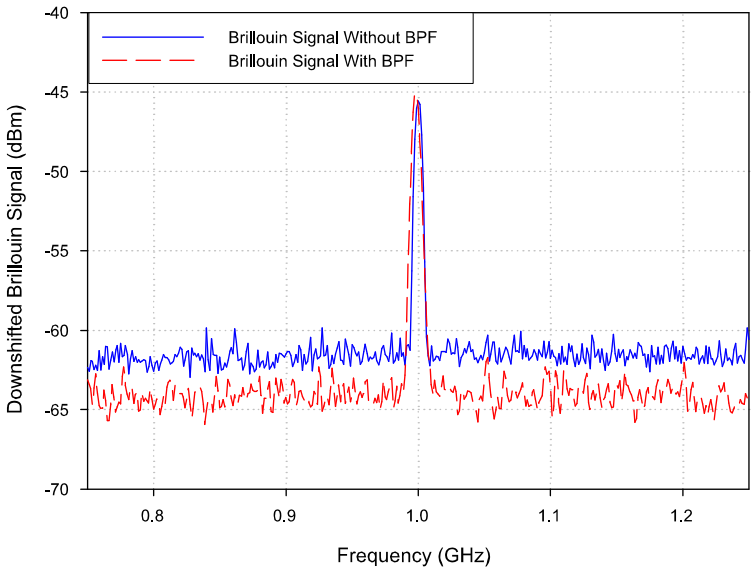

Figure 3.7: *Noise reduction due to the use of the notch filter at 9GHz in the microwave detection system.*

Figure 3.7 compares the 1GHz signal with/without the 9GHz notch filter. Around 3dB improvement on SNR was achieved with the use of the filter.

[2]SENSA, Chilworth Science Park,UK.[*Through personal communication*].

3.4.3 Spatial Resolution and System Applications

The spatial resolution of MDS is determined by the bandwidth of the 1GHz BPF and the rise time of the RF diode rectifier. Currently, the 1GHz BPF bandwidth is around 50MHz (∼60cm spatial resolution) and could be increased up to ∼80MHz (∼4cm spatial resolution). The rise time of the current RF diode is around 10ns (∼1m spatial resolution). With faster RF diodes, typically the conversion ratio from RF power to DC voltage is reduced[3]. However, for ultra high spatial resolution measurements, the sensing range is expected to be short, therefore such reduction in the conversion ratio maybe tolerated. The MDS was mainly designed for high spatial resolution measurements combined with long sensing range. However, another new application of MDS that has been realised recently is the characterisation of special fibres designed to suppress SBS. In the next two sections, the MDS was examined for distributed temperature measurement over a sensing range of 30km with 2m of spatial resolution, and also used to characterise special fibres designed to suppress SBS.

[3]Specification sheet of the current RF diode.

3.5 Temperature Measurement using the Microwave Detection System

3.5.1 Introduction

Distributed optical fibre sensors based on Brillouin scattering, with sub-metre spatial resolution capabilities, have been previously reported, but were confined to relatively short sensing lengths, and focused on either measuring the Brillouin frequency shift [5] or power [6]. Several applications, such as the continuous monitoring of temperature/strain in underground power cables, live optical links and large scale structures, require sensors with relatively high spatial resolution combined with long range [7][8]. In this section, the optimised CBS, along with the microwave detection system, was experimentally demonstrated as a long range high spatial resolution distributed temperature sensor.

3.5.2 Experimental Details and Measurements

The experimental arrangement for the coherent detection of anti-Stokes spontaneous Brillouin backscatter, using the microwave detection system, is illustrated in figures 3.1 and 3.5. The source was a tuneable laser at 1533.2nm, with ∼1MHz linewidth, and 100μW CW output. Two EDFAs and an acousto-optic modulator were used to generate a probe pulse of 25mW and 20ns with a repetition rate of ∼80Hz, which was launched into the 32km sensing fibre. A single pass EDFA preamplifier was used to amplify the weak backscattered signal generated in the sensing fibre prior to mixing with a 1.8mW optical LO. A 20GHz lightwave detector and the microwave detection system allowed the collection of time-domain traces centred at the desired RF frequencies. The sensing fibre was standard SMF in 3 sections. The first 30km remained on the original spools at room temperature. The next 400m were placed in an oven at 60 °C. The subsequent 1.6km was maintained at room temperature and zero strain as a reference. To determine the spatial resolution and accuracy of the system, Brillouin frequency measurements were taken between 30 and 30.8km, where the central 400m length of fibre was heated to 60 °C, and the remaining fibre was at room temperature (20 °C). The temperature

change along the sensing fibre was determined by analyzing the frequency shift of the Brillouin backscatter. Brillouin spectra were built from 15 separate backscatter traces, each averaged 2^{15} times, taken every 10MHz, starting at 10.99GHz. A Lorentzian curve was fitted to each spectrum and the peak frequency was evaluated at each point along the sensing fibre. First, the spatial resolution was evaluated by measuring the rise time at a heated section; then the temperature change at the heated section 30km down the sensing fibre was measured. The frequency resolution along the sensing fibre was evaluated every 5km, averaged over a length of 500m, and then converted to the corresponding temperature resolution.

3.5.3 Experimental Results

The spatial resolution was limited by the rise time of the available modulator AOM used to generate the probe pulse, which limits the pulse width to ∼20ns. For clarity, figure 3.8 shows a 10-90% rise-time measured at the front end of the sensing fibre. It agrees with the expected performance, which is governed by the duration of the pulse and not by the electronics of the detection system.

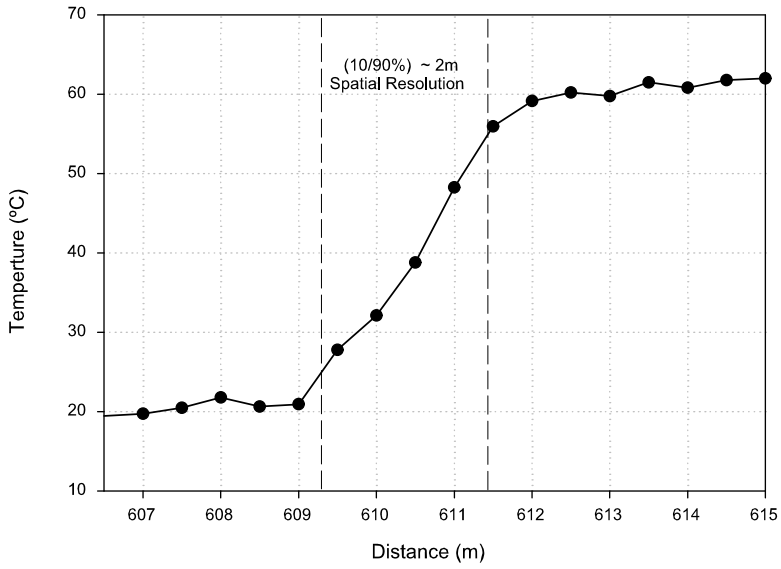

Figure 3.8: *A (10-90%) rise time of temperature change at 600m down the sensing fibre indicating spatial resolution of ∼2m.*

Figure 3.9 illustrates the temperature change at the heated section 30km down the sensing fibre.

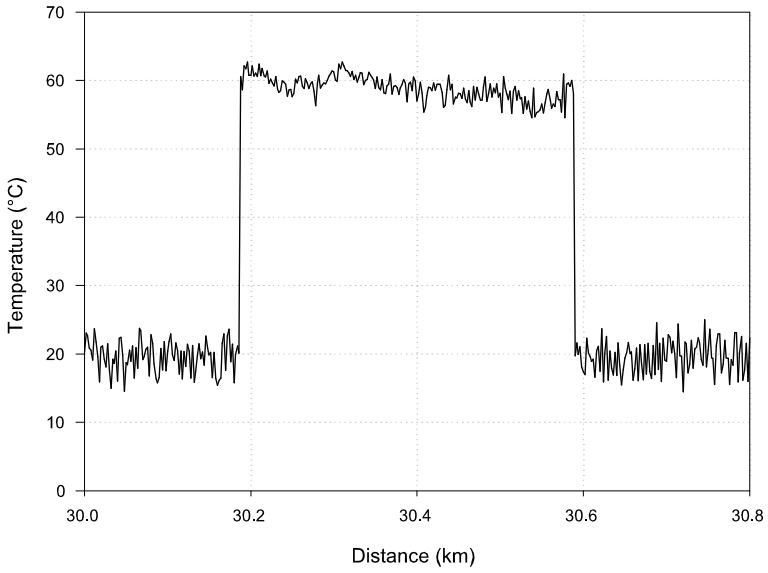

Figure 3.9: *Temperature change at the heated section 30km down the sensing fibre.*

The sensor was able to record temperature changes of less than 1.1 °C at up to 20km distance. The error increased with distance, but was less than 1.7 °C at the end of the sensing length. Figure 3.10 illustrates the temperature resolution along the sensing fibre.

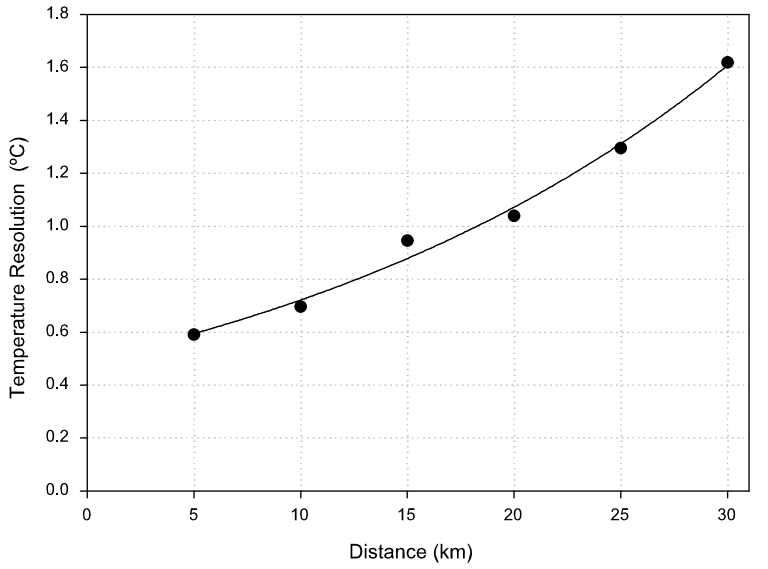

Figure 3.10: *The RMS temperature errors for the 20ns pulse width measurements along the sensing fibre at 5km intervals, averaged over a length of 500m.*

The system's accuracy may be improved by performing more time-domain trace averages, which will reduce noise but increase the measurement time. The rise time of the currently used RF diode rectifier (∼10ns) places an upper limit on the system's spatial resolution, but the detection system is now potentially capable of ∼60cm spatial resolution, provided its BPF bandwidth is tuned to its maximum (∼80MHz) and a faster microwave diode rectifier is used.

3.5.4 Discussion

A microwave detection system was demonstrated for coherent detection of backscattered spontaneous anti-Stokes Brillouin signals for distributed temperature/strain sensors. The aim was to improve the spatial resolution of the previously reported results by an order of magnitude, and this was achieved. The design represents an important and necessary advance for constructing a commercial sensor, as it dispenses with the previous need for an expensive ESA. It also promises practical high spatial resolution and accurate long range Brillouin based distributed optical sensing systems, with potential for further improvements in spatial resolution. As a future application of this new system, the set-up was used to characterise fibres designed to have a high SBS threshold for use in high power fibre lasers. This is reported in the next section.

3.6 Measurement of Suppressed Stimulated Brillouin Scattering in Special Fibres

In this section, the optimised coherent Brillouin sensor and its new microwave detection system were used to test and characterise different fibres with different properties/structures to suppress Stimulated Brillouin Scattering (SBS). These fibres were designed and fabricated to have a high SBS power threshold and to allow their use in high power fibre laser systems. The task was to spatially resolve the Brillouin spectrum along such fibres with ∼1m spatial resolution.

3.6.1 Introduction

A technological revolution is occurring in the field of solid-state lasers, and the power produced by fibre laser systems has rapidly increased [9]. The combination of high power and ease of use is expected to benefit applications in a wide variety of fields, including semiconductor device manufacturing, surgery, military technology, industrial material processing, remote sensing imaging and scientific instrumentation [10]. One important class of these fibre laser systems is the high power single-frequency fibre laser. However, the detrimental effects of nonlinear interactions in the fibre core such as SBS are expected to limit the power achievable from single-frequency sources [11]. Figure 3.11 illustrates schematically the typical additional loss that SBS introduces as soon as the launched power reaches a definite level.

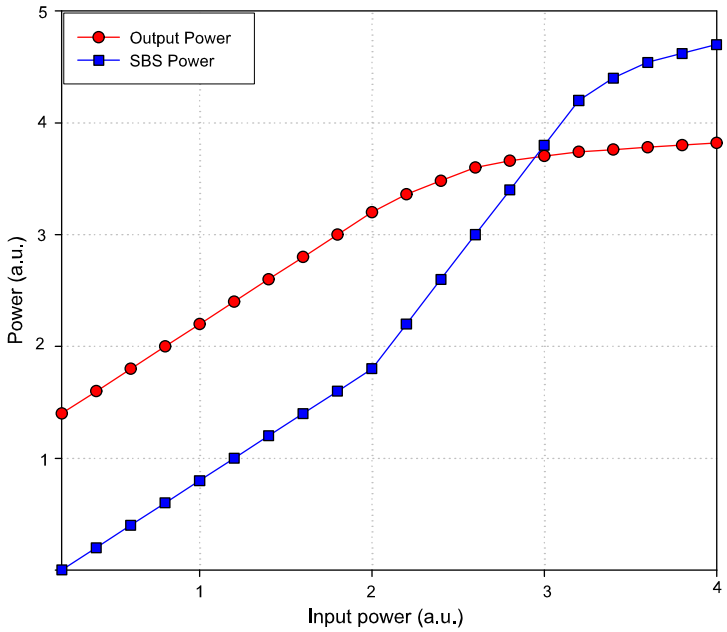

Figure 3.11: *General effect of SBS on the output power (After [12]).*

Stimulated Brillouin scattering is governed by the generation of acoustic waves through the process of electrostriction. This in turn causes a periodic modulation of the refractive index and light is scattered through Bragg diffraction. In general, the waveguide structure and refractive index profile can also affect acoustic wave behaviour in fibres and result in changes in Brillouin scattering properties. In fact, there have been attempts to reduce the effect of SBS by changing the Brillouin scattering properties within the fibre. This can be achieved through variation of the composition along the fibre length and/or varying the core radius and introducing non-uniformities by stressing the optical fibre. In general, these techniques lead to a non-uniform Brillouin frequency shift along the fibre and/or broadening of integrated Brillouin bandwidth, and, as a consequence, higher SBS threshold powers [13] [14].

Southampton University is a leading player in the field of high power fibre laser technology, and has a particular interest in investigating the design of fibres that suppress SBS [15]. The fibres characterised here were designed and fabricated at the ORC by the fibre fabrication group led by Dr. Jayanta Sahu.

Figure 3.12 illustrates schematically the main two structures of fibres that were characterised.

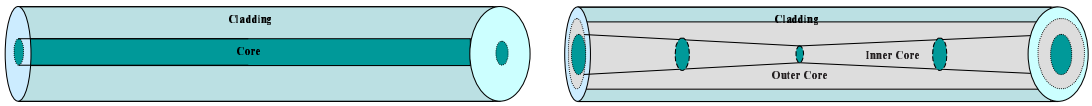

(a) *Non-tapered uniform core/cladding fibre structure.* (b) *Structure of tapered fibre with two cores.*

Figure 3.12: *Schematic diagrams of two fibre structures designed and fabricated to have high SBS threshold power.*

Figure 3.12(a) shows uniform core/cladding structures, and figure 3.12(b) shows a nonuniform fibre structure (*tapered*), which has a double core structure. In this type of structure, the inner core size varies with fibre length, which may have different dopants and/or concentration levels compared to the outer core. The uniform structure may have two cores as well. Four different fibres (A, B, C, and D) were selected for characterisation, and table 3.2 summarises their properties.

Table 3.2: *Characterised fibre properties.*

Fibre	**Fibre Structure**	**Dopants**	**Length (m)**	**Loss (dB/m)** *(At 1533nm)*	**Diameter (μm)**	**NA**
A	Non-tapered single core	Al	300	~ 0.01	100	0.13
B	Tapered double core	Al/Ge	100	~ 0.18	80	0.12
C	Non-tapered single core	Al	100	~ 0.138	80	0.12
D	Non-tapered double core	Ge/Yb	150	~ 0.036	100	0.13

Variations of fibre composition and structure are expected to change the property of the Brillouin gain spectrum in terms of the number of Brillouin peaks, frequency shifts and Brillouin linewidth. To verify the expected changes within a relatively short length of fibre, the MDS for the CBS was used to spatially resolve the Brillouin spectrum at each point of interest along the fibres, with ∼1m of spatial resolution. The system spatial resolution was limited by the response time of the available RF diode rectifier (∼10ns).

3.6.2 Experimental Details and Measurements

The experimental set-up for characterising the Brillouin scattering in the tested fibres is shown schematically in Figure 3.13.

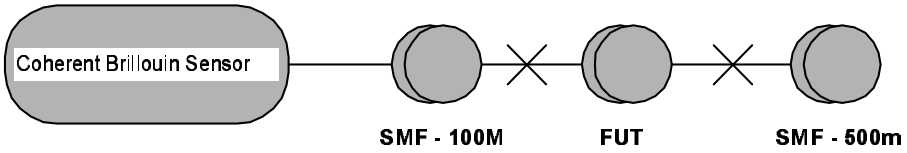

Figure 3.13: *Experimental set-up for characterising special fibres for suppressed SBS.*

The coherent Brillouin sensor and the microwave detection system, previously described in figures 3.2 and 3.5 respectively, were used. However, to achieve high spatial resolution measurements, the AOM[4] was replaced by an EOM to achieve a shorter pulse width (∼ns) for fast response time, and hence better spatial resolution. For clarity and comparison purposes, two sections of standard SMF (100m and 500m) were used as references before and after the fibre to be characterised (Figure 3.13). Such fibre has a loss of ∼0.20dB/km, an effective area of ∼80μm^2 and a diameter of ∼125μm. The integrated Brillouin signal, i.e. for the whole fibre, was first measured using an ESA. This allowed the Brillouin frequency shift and number of peaks to be identified. The microwave detection system was then used to spatially resolve the Brillouin spectrum along the fibre. The Brillouin peaks' shift and linewidth along these fibres were measured by fitting Lorentzian functions to each spectra of interest.

[4]Response time was limited to around 20ns.

3.6.3 Experimental Results

Figure 3.14 shows the spatially resolved Brillouin spectrum along the four characterised fibres A, B, C and D respectively.

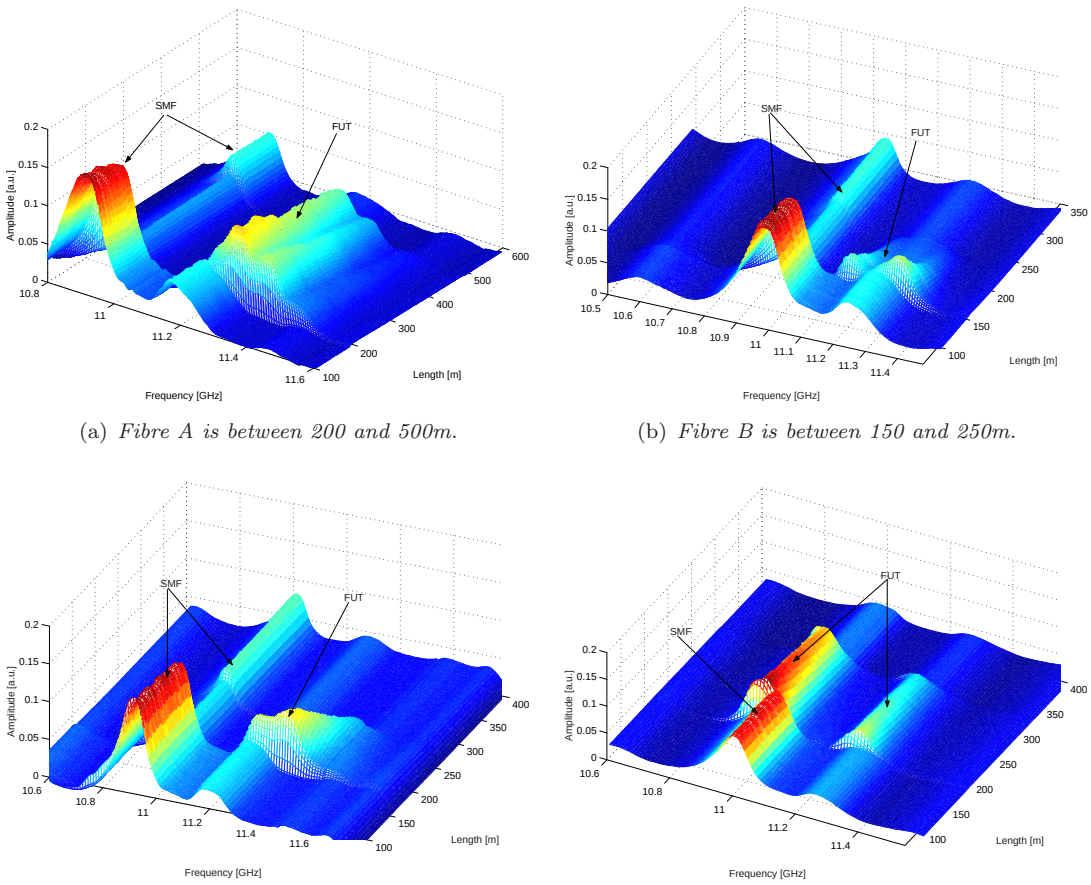

(a) *Fibre A is between 200 and 500m.*

(b) *Fibre B is between 150 and 250m.*

(c) *Fibre C is between 200 and 300m.*

(d) *Fibre D is between 200 and 350m.*

Figure 3.14: *Spatially resolved Brillouin spectrum along different tested fibres.*

The Brillouin spectrum along these characterised fibres are shown with the reference spectrum of standard SMF, which has only one Brillouin peak centred at ∼11.1GHz. The change in Brillouin scattering properties (Brillouin frequency shift, line width and number of peaks) of the characterised fibres (Figure 3.14) is due to the change in the waveguide structures and dopants (Table 3.2). Due to the high loss in some of the fibres under test (Table 3.2), the Brillouin signal is severely attenuated, but still measurable. Figure 3.14(a) shows fibre A; this non-tapered fibre exhibits two adjacent peaks. However, for simplicity they will be considered as being one main structural peak situated at ∼11.3GHz, with much larger linewidth compared to the reference SMF.

Figure 3.14(b) shows fibre B. This tapered fibre exhibits two distinct adjacent peaks, a smaller peak at ∼11.15GHz and a larger one at ∼ 11.33GHz. Fibre C is shown in Figure 3.14(c). This fibre exhibits two adjacent peaks, which can be again considered as one main peak situated at ∼11.35GHz. Fibre D has two distinct peaks. The first peak at the lower frequency is larger than the second one, as can be seen from Figure 3.14(d). In order to evaluate Brillouin properties at any point of interest along the characterised fibres, the data of figure 3.14 was analysed, Brillouin spectra corresponds to the 50^{th}m from the FUT front end was chosen for analysis. By fitting a single or double Lorentzian curve to the spectra, Brillouin peaks, frequency shift and linewidth at that particular point were determined. Figure 3.15 illustrates the Brillouin peaks, frequency shift and linewidth measured in the four characterised fibres.

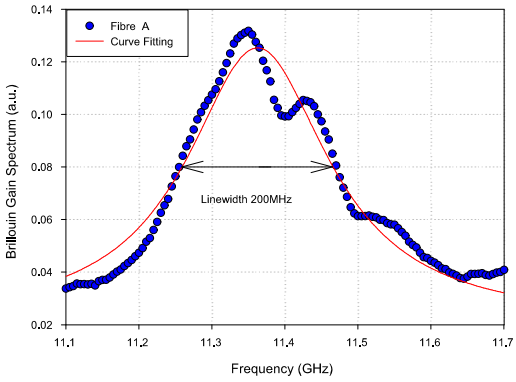

(a) *Brillouin spectrum at the 50^{th}m of fibre A.*

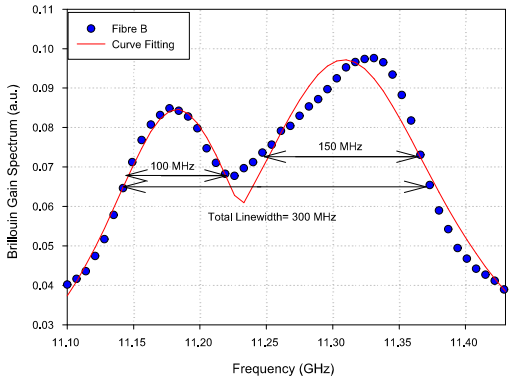

(b) *Brillouin spectrum at the 50^{th}m of fibre B.*

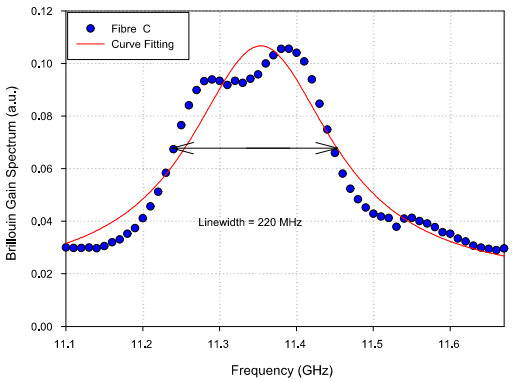

(c) *Brillouin spectrum at the 50^{th}m of fibre C.*

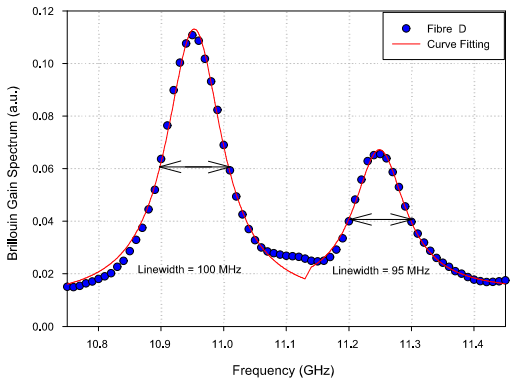

(d) *Brillouin spectrum at the 50^{th}m of fibre D.*

Figure 3.15: *Brillouin peaks, frequency shift and linewidth measured at the 50^{th}m of each of the four characterised fibres.*

Fibres A and C exhibit two adjacent peaks with an overall linewidth of around 200 and 220MHz (Figure 3.15(a) and Figure 3.15(c)), respectively. The similarities between these two fibres may resulted because both have a single core structure.

Fibre B and D on the other hand have double core structure and exhibit double peaks. The two distinct peaks in fibre B are shown in (Figure 3.15(b)). The smaller peak is centred at 11.175GHz with ∼100MHz linewdith and the second peak is at 11.33GHz with ∼150MHz linewidth. The overall linewidth of both peaks in fibre B is around 300MHz. Fibre D (Figure 3.15(d)) also has two distinct peaks situated at 10.95GHz and 11.25GHz. The second peak is relatively small (∼50% smaller) compared to the main one at 10.95GHz. These two peaks are separated by more than 300MHz and exhibit a comparable linewidth of ∼100MHz.

In order to account for any spectral broadening due to the relatively narrow pulse width, the Brillouin spectral linewidths of the characterised fibres were referenced to the Brillouin spectrum of the standard SMF, the relative broadening are illustrated in Table 3.3, which also summarises in more detail the Brillouin characteristics of the four test fibres.

Table 3.3: *Brillouin properties of the characterised fibres.*

Fibre	**Number of main peaks**	**Frequency shift** (GHz)	**Linewidth** (MHz	**Relative Linewidth to SMF**
A	1	∼11.35	∼200	2
B	2	(∼11.175)(∼11.33)	(∼100)(∼150)	1 & 1.5
C	1	∼11.35	∼220	2.2
D	2	(∼10.95)(∼11.25)	(∼100)(∼95)	1 & 0.95

3.6.4 Discussion

These results indicate clearly that Brillouin gain spectral properties such as number of peaks, frequency shifts and linewidth, are dependent on the structure and dopant variations along the optical fibre. It is evident from this preliminary result that it is possible to design and fabricate fibres with broadened Brillouin spectra. This is expected to increase the SBS threshold power and hence allow higher power fibre lasers to be built. The CBS demonstrated adequate sensitivity in measuring the Brillouin spectrum area in these lossy fibres. Spatial resolution could be further improved by using a faster RF diode combined with a wider BPF bandwidth.

3.7 Conclusions

The coherent Brillouin sensor and the microwave detection system were reconfigured and optimised for better sensing performance, exhibiting around 9 and 6dB improvement on the Brillouin optical and electrical power, respectively. The optimised sensor was demonstrated for a distributed temperature measurement over 30km with 2m spatial resolution and 1.6 °C of temperature resolution. The system was also used successfully for the first time to spatially resolve the Brillouin spectrum in special fibres with ∼1m spatial resolution for suppressed SBS verification. From both measurements, it was evident that the optimised sensor along with its MDS provides a commercially practical solution for high spatial resolution measurements. Due to the weak dependence of Brillouin power with temperature and strain, along with other factors such as fibre loss and nonlinear effects, the accuracy of Brillouin power measurement limits the accurate determination of temperature and strain simultaneously over long sensing range. The next chapter investigates alternative techniques that avoid the need to measure the Brillouin power.

Bibliography

[1] S. M. Maughan, H. H. Kee and T. P. Newson, "Simultaneous Distributed Fibre Temperature and Strain Sensor using Microwave Coherent Detection of Spontaneous Brillouin Backscatter," *Measurement Science and Technology*, vol. 12, p. 834, February 2001.

[2] N. P. Lawrance, "A Hybrid Microwave Heterodyne Receiver Design for use in Distributed Fibre Sensing of Spontaneous Brillouin Backscatter," Master's thesis, University of Southampton, September 2002.

[3] W. H. Press, S. A. Teukolsky, W.T. Vetterling and B. P. J. Flannery, *Numerical Recipes in C-the Art of Scientific Computing*, 2nd ed. Cambridge University Press, 1995.

[4] Hewlett Packard, "Spectrum Analyzers: Optimizing spectrum analyzer amplitude accuracy," *Hewlett Packard*, vol. E, p. 59.

[5] K. Hotate and T. Hasegawa, "Measurement of Brillouin Gain Spectrum Distribution Along an Optical Fiber with a High Spatial Resolution using a Novel Correlation-Based Technique," *13^{th} International Conference on Optical Fiber Sensors Technical Digest (OFS)*, p. 337, April 1999.

[6] H. H. Kee and T. P. Newson, "1.5 μm Brillouin-Based Fibre Optical Distributed Temperature Sensor with High Spatial Resolution of 20 cm," *14^{th} International Conference on Optical Fiber Sensors Technical Digest (OFS)*, p. 800, October 2000.

[7] P. C. Wait and A. H. Hartog, "Spontaneous Brillouin-Based Distributed Temperature Sensor Utilizing a Fiber Bragg Grating Notch Filter for the Separation of the

Brillouin Signal," *IEEE Photonics Technology Letters*, vol. 13, no. 5, p. 508, May 2001.

[8] F. H. Wild and P. Schmetz, "The Applications of Optical Sensors for Temperature, Mechanical Stress and Moisture in Energy Cables in the Netherlands," *14^{th} International Conference on Optical Fiber Sensors Technical Digest (OFS)*, p. 820, 2001.

[9] V. Gapontsev and W. Krupke, "Aided by Side Pumping with Multiple Modules, Fibre Lasers Now Reach Diffraction-limited Outputs of 100W and Low Order Multimode Outputs of up to 2KW," *Laser Focus World*, p. 83, August 2002.

[10] A. Galvanauskas, "High Power Fiber Lasers," *Optics and Photonics News*, July 2004.

[11] A. Liem, J. Limpert, H. Zellmer and A. Tunnermann, "100-W Single-frequency Master-oscillator Fibre Power Amplifier," *Optics Letters*, vol. 28, no. 17, p. 1537, September 2003.

[12] "Stimulated Brillouin Scattering - SBS," Fibre Optics Information, www.fibre-optics.info, Tech. Rep.

[13] G. P. Agrawal, "Suppression of Stimulated Brillouin Scattering in Optical Fibers Using Fiber Bragg Gratings," *Optics Express*, vol. 11, no. 25, p. 3467, December 2003.

[14] N. Yoshizawa, T. Horigushi and T. Kurashima, "Proposal for Stimulated Brillouin Scattering Suppression By Fibre Cabling," *Electronics Letters*, vol. 27, no. 12, p. 1100, June 1991.

[15] Y. Jeong, J. K. Sahu, D. N. Payne and J. Nilsson, "Ytterbium-doped Large-core Fibre Laser with 1kW of Continuous-wave Output Power," *Electronics Letters*, vol. 40, no. 8, p. 470, April 2004.

Chapter 4

Simultaneous Temperature and Strain Measurement Techniques

4.1 Introduction

Although it is possible to separately resolve temperature and strain along a single linear fibre using the dependencies of the spontaneous Brillouin power on temperature and strain combined with the frequency information, the power measurement limits performance in long range sensing. As a result, alternative measurement techniques that avoid the Brillouin power measurement were required. In this chapter, two different techniques, frequency shift of dual Brillouin peaks and combined spontaneous Raman and Brillouin scattering were investigated for simultaneous temperature and strain measurement over a 23km sensing range and compared to the conventional Brillouin frequency and power based technique. The relative advantages of these techniques were identified and reported.

4.2 Spontaneous Brillouin Frequency and Power Based Technique

4.2.1 Introduction

In this section, distributed temperature and strain were measured simultaneously over 23km of standard single mode fibre using a spontaneous Brillouin frequency shift and power change based technique. This conventional measurement was used as a reference for comparison with other techniques.

4.2.2 Principle of Operation

As described in Section 3.6, the number of Brillouin peaks and their frequency shifts correspond to the fibre refractive index, structure and dopant materials. In standard SMF fibre, Brillouin scattering exhibits one main spectral peak around 11GHz. Figure 4.1 illustrates both the standard SMF refractive index and its Brillouin gain spectrum measured at room temperature and 1550nm.

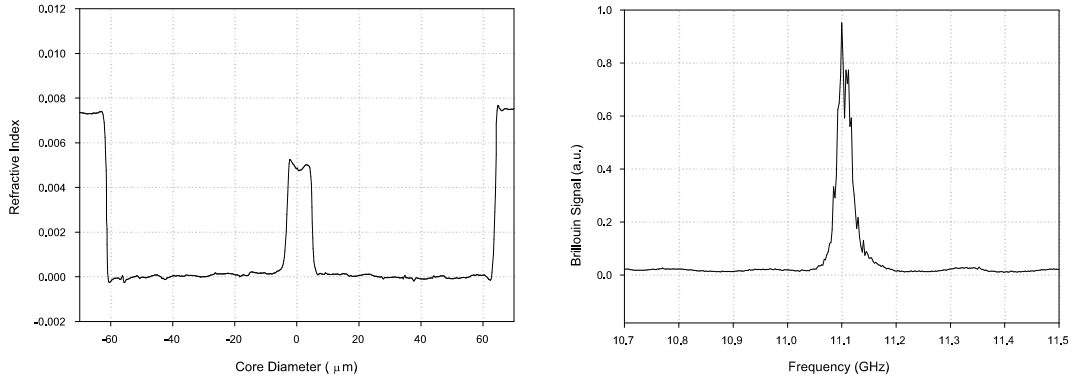

(a) *Refractive index profile of standard SMF.* (b) *Spontaneous Brillouin spectrum in SMF.*

Figure 4.1: *Single mode fibre refractive index profile and the corresponding Brillouin spectrum measured at room temperature and 1550nm.*

In standard SMF, the refractive profile is uniform across its cladding and core (Figure 4.1(a)). Hence, only one Brillouin peak at around 11GHz is observed (Figure 4.1(b)). By measuring both the absolute Brillouin peak frequency shift and power change simultaneously, the temperature and strain profile along the sensing fibre can be obtained

using equations 2.15 and 2.16 (described in Section 2.4.4). The corresponding errors in the derived temperature and strain measurements are given by equations 2.17 and 2.18, respectively [1] [2].

4.2.3 Experimental Details and Measurements

The experimental arrangement for measuring distributed temperature and strain simultaneously is shown schematically in the following figure. It should be noted that this measurement took place before the optimisation of the CBS described in Section 3.2.

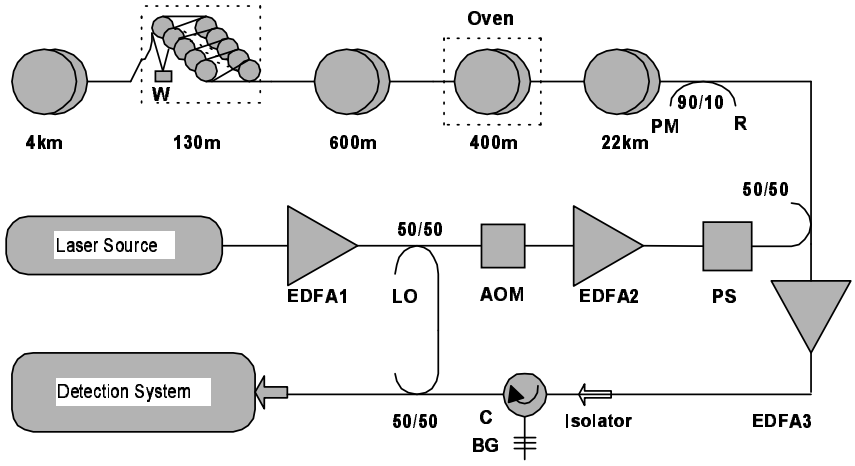

Figure 4.2: *Experimental set-up for measuring temperature and strain simultaneously.*

The source was a $\sim$100μW tuneable laser at 1533.17nm with EDFA amplification, generating a probe pulse of 120mW, and 100ns duration. This was launched into the sensing fibre. Coherent detection of the spontaneous Brillouin backscatter signal was achieved by direct measurement of the 11GHz beat frequency between the optical LO and the Brillouin signal, using a wide bandwidth lightwave detector along with the MDS. The SMF used in this experiment has a loss of $\sim$0.20dB/km and an effective area of $\sim$80μm^2. The sensing fibre was arranged as shown in Figure 4.2. The first 22km remained on the original spools at room temperature. The next 400m was loosely coiled and placed in an oven to allow heating, whilst ensuring zero strain. The subsequent 600m were used as a reference and maintained at room temperature with zero strain. The following 130m section was passed round 9 pairs of pulleys and loaded by placing weights suspended at the end of the rig to strain the fibre at room temperature. The last 4km was used as a second

reference length and maintained at room temperature with zero strain. The distributed temperature and strain variation around the heated and strained sections were determined by analysing the frequency shift and power change of the anti-Stokes Brillouin backscatter signal. Brillouin spectra were built from 18 separate backscatter traces, each averaged 2^{15} times, and taken every 10MHz, starting at 11.05GHz. A Lorentzian curve was fitted to each spectrum and the peak frequency and its power were evaluated at each point along the sensing fibre. All Brillouin frequency shift measurements were referenced to room temperature and zero strain. Brillouin power was measured by evaluating the sum of Brillouin spectrum components at each point along the sensing fibre and was normalised by a Brillouin trace taken at room temperature/zero strain to account for fibre splice/loss. Initial measurements were performed to reconfirm Brillouin frequency/power reported coefficients with respect to temperature/strain using standard SMF (Section 2.4.4). Results are shown in the following table.

Table 4.1: *Temperature and strain coefficients obtained in SMF.*

Coefficients	**Corresponding values**
K_T^ν	1.07 ± 0.070 MHz$(\,^\circ\mathrm{C})^{-1}$
K_ϵ^ν	0.048 ± 0.003 MHz$(\mu\varepsilon)^{-1}$
K_T^P	0.36 ± 0.030 $\%(\,^\circ\mathrm{C})^{-1}$
K_ϵ^P	$-9 \times 10^{-4} \ \pm 1^{-5}$ $\%(\mu\varepsilon)^{-1}$

The measured coefficients' values are in close agreement with previously reported values (Section 2.4.4). Such coefficients were used in the subsequent measurements. In order to validate the performance and accuracy, measurements were taken between ∼20 and 23km at oven temperatures of 60 °C and applied strain of 1500$\mu\varepsilon$ for the heated and strained sections, respectively.

4.2.4 Experimental Results

Figure 4.3 shows the normalised Brillouin frequency shift and power change around the heated and strained fibres.

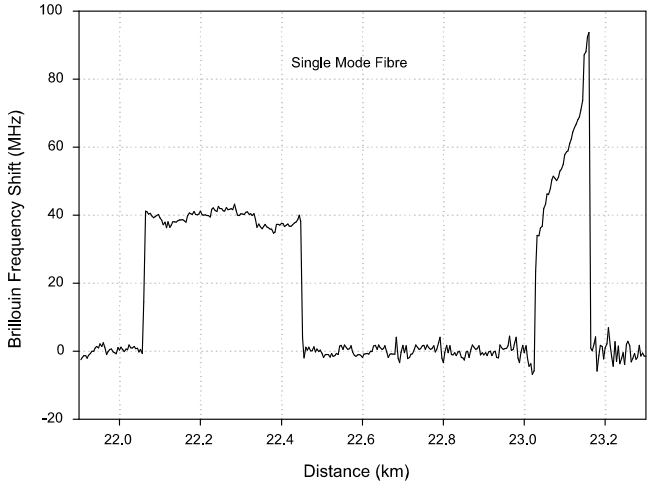

(a) *Brillouin frequency shift referenced to room temperature.*

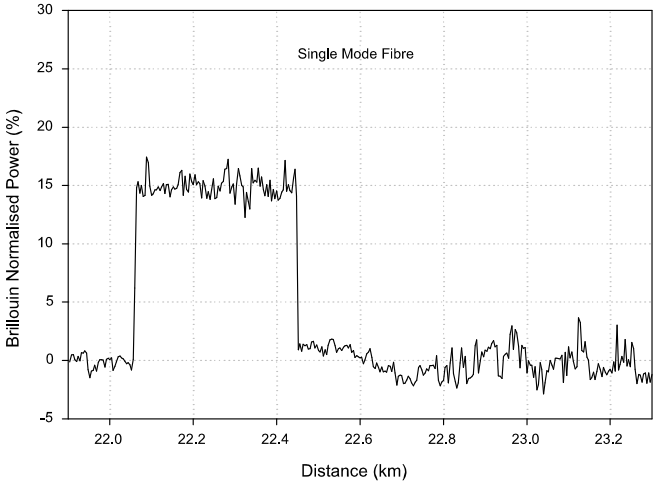

(b) *Normalised Brillouin power change.*

Figure 4.3: *Normalised Brillouin frequency shift and power change around the heated and strained sections.*

Using the measured Brillouin frequency shift $\Delta\nu$ and power change ΔP (Figure 4.3) along with the measured Brillouin frequency and power coefficients, temperature and strain profiles were derived using equations 2.15 and 2.16, respectively. Results are shown in Figure 4.4.

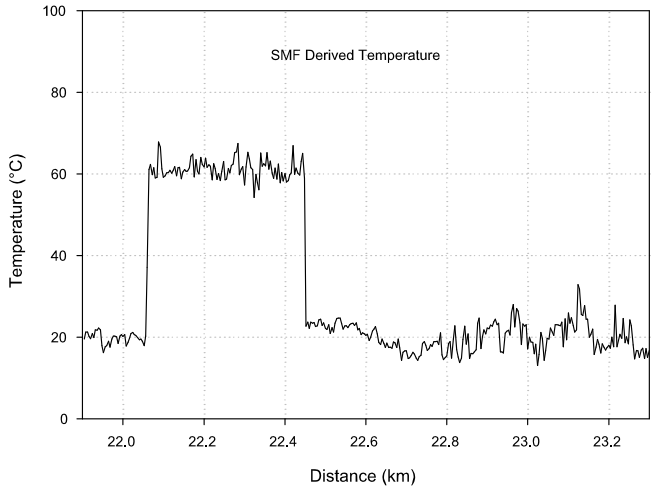

(a) *Derived temperature profile.*

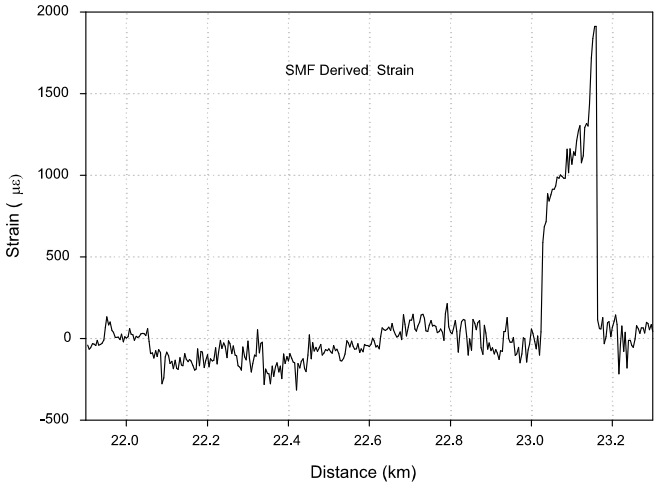

(b) *Derived strain profile.*

Figure 4.4: *Derived temperature and strain profiles around the heated and strained sections.*

As can be seen from Figure 4.4, there is a little cross talk between temperature and strain, and the nonuniform strain distribution is due to pulley friction on the strained fibre. The derived temperature and strain resolution can be obtained by using Brillouin frequency and power RMS errors $\delta\nu$ and δP, respectively. The RMS errors were measured at the reference section (Figure 4.3) and were found to be $\sim$1.31MHz and $\sim$1.64%, respectively. Using equations 2.17 and 2.18, the temperature and strain resolution were found to be $\sim$4 °C and $\sim$120$\mu\varepsilon$, respectively. These values will be compared to the other temperature and strain resolutions obtained using different measurement techniques.

4.2.5 Discussion

Initially, it was verified that Brillouin power was temperature dependent, but that the power was relatively weakly dependent on strain; i.e., 1 °C or 300$\mu\varepsilon$ produces the same change in power, whilst 1 °C or 20$\mu\varepsilon$ produces the same change in frequency. In fact, it was reported that power error is responsible for 99.7% of the temperature error and 94% of the strain error [1]. The effect of the power error on the measurand resolution can be seen clearly by using the obtained frequency and power errors, so that, for example, if the power error is halved, then the temperature and strain errors will be ∼2 °C and ∼70$\mu\varepsilon$, respectively, compared to 4 °C and 120$\mu\varepsilon$. On the other hand if the frequency error is halved, then the computed temperature and strain resolution will be ∼4 °C and ∼110$\mu\varepsilon$, respectively. In order to explore other techniques which provide an alternative to relying on the Brillouin power for separating temperature and strain, the use of sensing fibres with multiple Brillouin peaks that exhibit different frequency variations with temperature was investigated and is reported in the next section.

4.3 Multiple Peaks of Brillouin Frequency Based Technique

4.3.1 Introduction

It was demonstrated and concluded in the previous section that measurand errors arise mainly from the noise on the Brillouin power trace. Hence, to avoid the Brillouin power measurement, a solution recently proposed by Lee *et al.* [3] is to use Brillouin frequency shifts in Large Effective Area Fibre(LEAF)^{TM}, which is Non-zero Dispersion Shifted Fibre (NZ-DSF)[1]. This kind of fibre has a positive dispersion (4.3ps/nm.km) at 1550nm and a multiple composition fibre core, and hence multiple Brillouin peaks. The previously reported work [3] was restricted to a relatively short sensing fibre length of ∼3.7km; in this work the range was extended to over 23km and its accuracy determined for later comparison.

4.3.2 Principle of Operation

The Brillouin spectrum of a silica fibre depends on the structure and doping composition of the fibre core. In SMF, only one peak is observed (Figure 4.1(b)), whilst multiple peaks are observed in LEAF. These peaks can arise mainly from the refractive index profile of the core and other factors, as described in Section 3.6: two peaks were observed for core profiles, with a central dip in refractive index [4]. Figure 4.5 illustrates the refractive index profile and Brillouin spectrum in LEAF fibre measured at room temperature and 1550nm.

[1] A dispersion shifted single mode fibre that has the zero-dispersion wavelength near the 1550nm window.

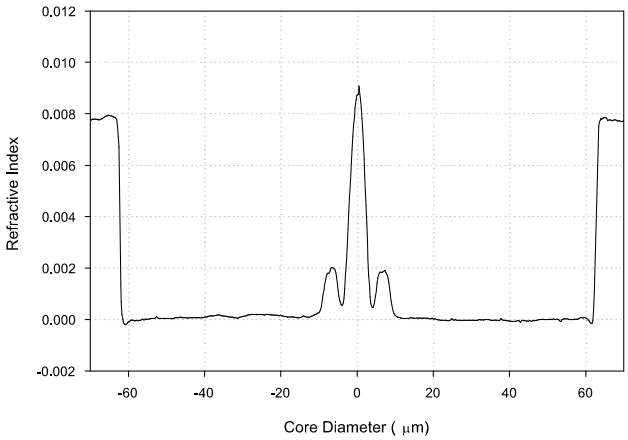

(a) Refractive index profile in LEAF.

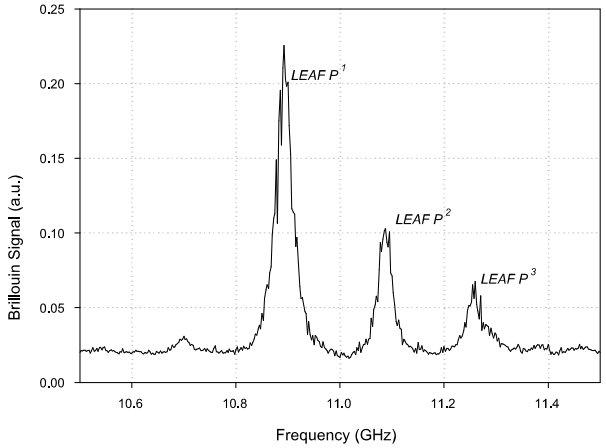

(b) Brillouin spectrum in LEAF.

Figure 4.5: *Refractive index profile and spontaneous Brillouin spectrum in LEAF measured at room temperature and 1550nm*

As shown in Figure 4.5(a), the LEAF refractive index profile across the core region is not uniform; hence multiple peaks appear in the Brillouin spectrum, as shown in Figure 4.5(b). The central frequencies of these peaks, (P^1 and P^2) at room temperature were found to be at ∼10.97 and ∼11.14GHz, respectively. The third peak at ∼11.24GHz is relatively small and is neglected in this work. Lee *et al.* [3] demonstrated that the frequency shift dependence of the Brillouin 1^{st} and 2^{nd} peaks are notably different for temperature, but similar for strain. Using the Brillouin frequency shift and power change matrix equation (described in Section 2.4.4), but substituting the power change by the frequency shift of the LEAF 2^{nd} peak, the Brillouin frequency shifts of peak one $\Delta\nu^{P1}$ and peak two $\Delta\nu^{P2}$ are related to temperature ΔT and strain $\Delta\varepsilon$ by the following

relation:

$$\Delta\nu^{Pi} = K_{\nu T}^{Pi}\Delta T + K_{\nu\varepsilon}^{Pi}\Delta\varepsilon \tag{4.1}$$

Where i= 1 and 2, $K_{\nu T}^{Pi}$ and $K_{\nu\varepsilon}^{Pi}$ are the changes in frequency of peak i with temperature and strain, respectively. Since the strain coefficients for LEAF peaks P^1 and P^2 are equal, the change in temperature and strain can be derived from equation 4.1 and are given by equations 4.2 and 4.3, respectively:

$$\Delta T = \frac{\Delta\nu^{P1} - \Delta\nu^{P2}}{K_{\nu T}^{P1} - K_{\nu T}^{P2}} \tag{4.2}$$

$$\Delta\epsilon = \frac{\Delta\nu^{P2}K_{\nu T}^{P1} - \Delta\nu^{P1}K_{\nu T}^{P2}}{K_{\nu T}^{P1}K_{\nu\varepsilon}^{P1} - K_{\nu T}^{P2}K_{\nu\varepsilon}^{P1}} \tag{4.3}$$

By measuring both Brillouin peaks' frequency RMS error, the error in derived temperature and strain can be calculated using the following equations:

$$\delta T = \frac{\left|K_{\nu\varepsilon}^{P2}\right|\delta\nu^{P1} + \left|K_{\nu\varepsilon}^{P1}\right|\delta\nu^{P2}}{\mid K_{\nu T}^{P2}K_{\nu\varepsilon}^{P1} - K_{\nu\varepsilon}^{P2}K_{\nu T}^{P1}\mid} \tag{4.4}$$

$$\delta\varepsilon = \frac{\left|K_{\nu T}^{P2}\right|\delta\nu^{P1} + \left|K_{\nu T}^{P1}\right|\delta\nu^{P2}}{\mid K_{\nu T}^{P2}K_{\nu\varepsilon}^{P1} - K_{\nu\varepsilon}^{P2}K_{\nu T}^{P1}\mid} \tag{4.5}$$

Where $\delta\nu^{P1}$ and $\delta\nu^{P2}$ are the measured RMS error on the Brillouin frequency shift of peak one and two respectively.

4.3.3 Experimental Details and Measurements

The experimental set-up for this measurement was similar to that for the previous measurement (Figure 4.2). The LEAF investigated was NZ-DSF single mode fibre with the following characteristics: loss of ∼0.199dB/km, effective area of $\sim 72\mu m^2$, and dispersion of 4.3ps/nm.km at 1550nm. Initial tests were performed to establish values for the coefficients governing the frequency shifts of peak one and two for their variations with temperature and strain. By applying different combinations of temperature and strain to the LEAF fibre and measuring the Brillouin frequency shifts of both peaks, the relative temperature and strain coefficients were obtained. The results are shown in Figure 4.6.

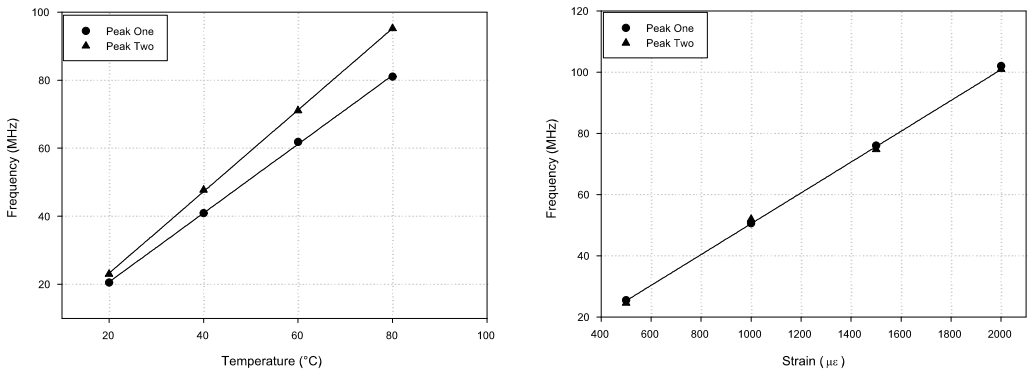

(a) *Peak one and two frequency shifts at different temperatures.*

(b) *Peak one and two frequency shifts at different applied strain.*

Figure 4.6: *LEAF peak one and two dependence on temperature and strain, respectively.*

Figure 4.6(a) shows that peak two has stronger dependence on temperature than peak one. However, for strain, the two peaks exhibited the same dependency, as shown in Figure 4.6(b) which agrees with previously reported work [3]. Using the data of figure 4.6, the measured coefficients' values were averaged, as summarised in Table 4.2.

Table 4.2: *Temperature and strain coefficients in LEAF*

Measurands	**Peak One** *i=1*	**Peak Two** *i=2*
$K_{\nu T}^{Pi} \quad MHz(^\circ C)^{-1}$	1.03±0.081	1.19±0.083
$K_{\nu \varepsilon}^{Pi} \quad MHz(\mu\epsilon)^{-1}$	0.051±0.001	0.050±0.002

The LEAF fibre was then heated to 60 °C and strained to 1500$\mu\varepsilon$, as in the previous measurement, at a distance of 23km, and measurements for the Brillouin frequency shifts of peak one and two were established. Brillouin anti-Stokes backscatter traces were collected at a number of frequencies for both peaks. The Brillouin spectrum at each point was obtained by fitting double Lorentzian curves to the data.

4.3.4 Experimental Results

Figure 4.7 shows a three dimensional plot of the Brillouin frequency shift of P^1 and P^2 from 22 to 80 °C at a distance of 9km, chosen for clarity, down the sensing LEAF.

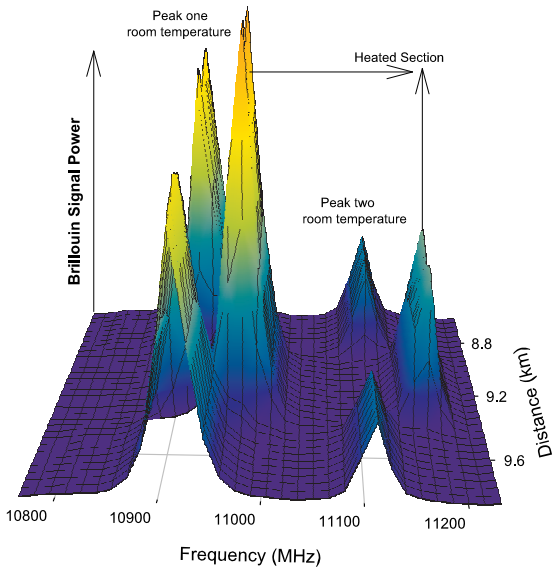

Figure 4.7: *Three dimensional representation of LEAF peak one and two frequency shifts at a heated section some distance down the sensing fibre.*

Figure 4.8 shows the Brillouin frequency shifts of both peaks measured from ∼21.8 to ∼23.3km. Both frequency shifts were referenced to room temperature and zero strain.

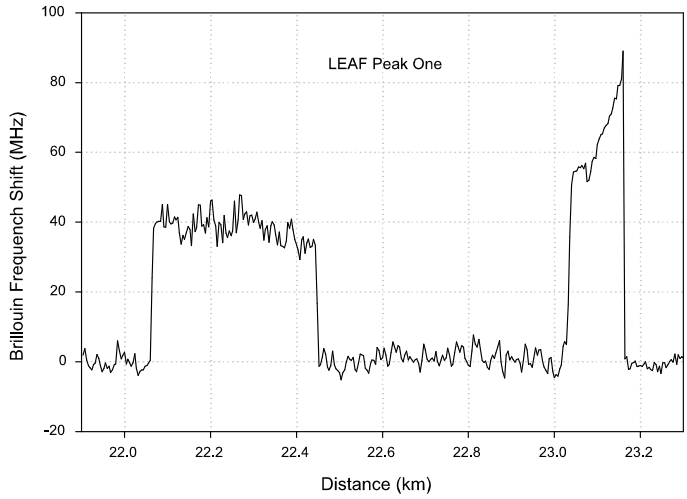

(a) *Brillouin frequency shift of peak one.*

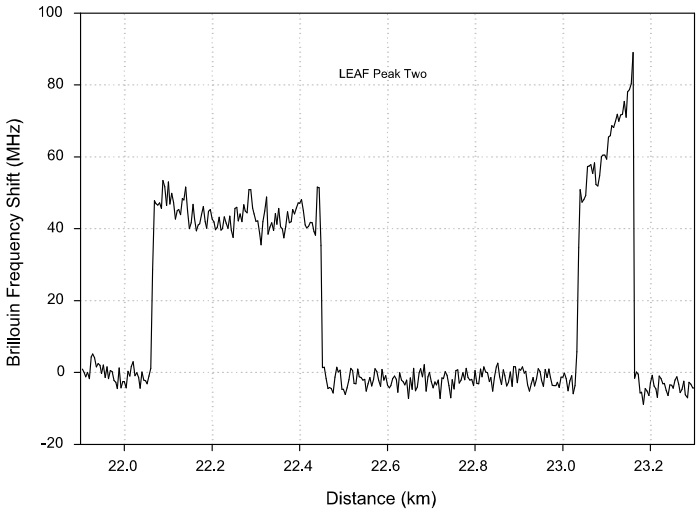

(b) *Brillouin frequency shift of peak two.*

Figure 4.8: *Brillouin frequency shift of peak one and two in LEAF, referenced to room temperature and zero strain.*

The variation in frequency over the strain region is attributed to the friction in the pulley system. Using the Brillouin frequency shifts of peak P^1 and P^2, temperature and strain were computed using equations 4.2 and 4.3. Figures 4.9(a) and 4.9(b) show the derived profile of temperature and strain, respectively.

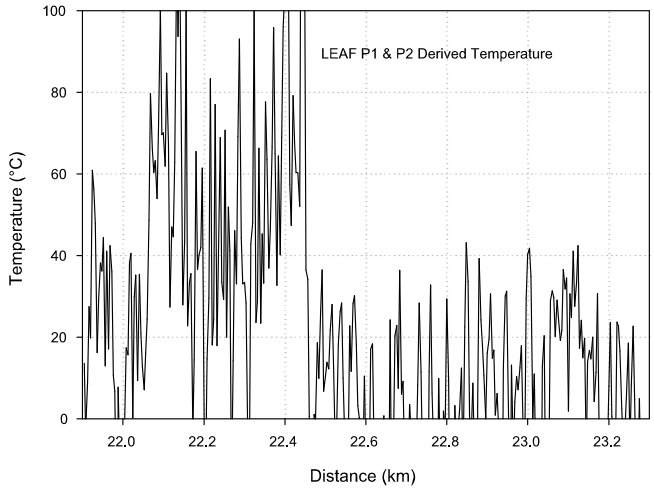

(a) *Derived temperature profile.*

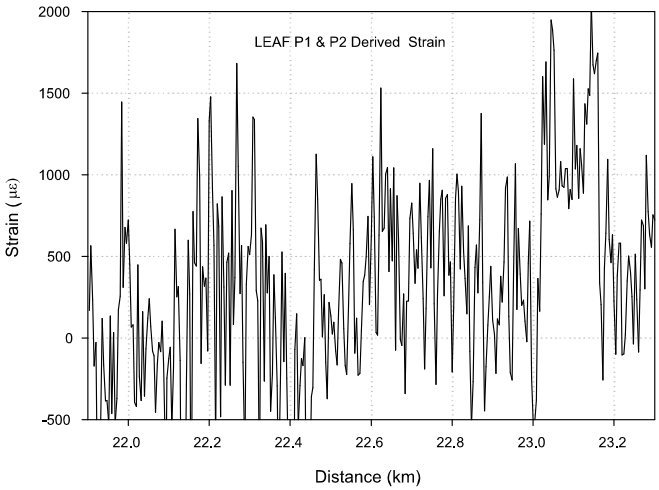

(b) *Derived strain profile.*

Figure 4.9: *Derived temperature and strain profiles around the heated and strained sections of LEAF.*

There is some induced crosstalk between temperature and strain, as shown in Figure 4.9. Using the data of figure 4.8, the frequency error of peak one $\delta\nu^{P1}$ and peak two $\delta\nu^{P2}$ were calculated and found to be ∼2.16MHz and ∼2.56MHz, respectively. The temperature and strain resolution were then calculated using equations 4.4 and 4.5, and found to be ∼29 °C and ∼630$\mu\varepsilon$ respectively.

4.3.5 Discussion

At present, the technique of using the two frequency peaks of the LEAF to measure temperature and strain yields increased errors when compared to the frequency and power analysis of the single frequency peak in SMF. Whilst the CBS method allows detection of the peak frequency to a resolution of less than a few MHz at this range, this new technique imposes more stringent requirements on the resolution of the frequency measurement; it is a differential frequency change that provides temperature information, i.e. ∼190kHz/ °C compared to ∼1MHz/ °C in SMF. A temperature resolution better than 1 °C requires individual frequencies to be resolved to approximately $190/\sqrt{2}$ or ∼135kHz. The spontaneous Brillouin linewidth is approximately 35MHz and, in the presence of noise will limit the frequency resolution measurement. Direct detection of the differential frequency may prove to be a means to achieving some improvement, as would fibres specifically designed to have a greater differential frequency change with temperature. It is believed that most of the measurand's error is associated with the second peak measurement, because it is smaller in magnitude compared to the first peak (40% smaller). Investigations indicated that it was just as troublesome to measure the differential frequency with the required precision and as yet it has been impossible to demonstrate any significant performance advantage over the frequency/power technique. As a result, another technique based on combining Raman power with Brillouin frequency shift was investigated, and is reported in the next section.

4.4 Combined Raman and Brillouin Scattering Based Technique

4.4.1 Introduction

In this section, an innovative technique to measure both temperature and strain simultaneously, which avoids Brillouin power measurement, is presented. This technique is based on measuring both the spontaneous Raman power and Brillouin frequency shift simultaneously. The two signals are generated from a single light source and access to only one end of the fibre is required.

4.4.2 Principle of Operation

The principle of this technique is based on optical time domain reflectometry, using a single pulsed light source operating at 1533nm and spatially resolving both the Brillouin anti-Stokes frequency shift and the power of the Raman anti-Stokes signal at 1450nm. The Raman signal is sensitive to temperature, but not to strain, and the temperature along the fibre can be determined. This is the basis of conventional Raman based Distributed Temperature Sensors (DTS)^{TM}. With knowledge of the temperature of the fibre, the strain can then be computed from the Brillouin frequency shift information. The power of the anti-Stokes Raman signal is more sensitive to temperature 0.80%/ °C [5], than the anti-Stokes Brillouin signal, ∼0.30%/ °C. This to some extent compensates for it being more than one order of magnitude smaller than that of the Brillouin signal. To accurately predict the temperature changes, the Raman signal has to be referenced to a temperature independent signal measured with the same spatial resolution. In commercial Raman based distributed temperature sensors, a second source is normally used to generate the Rayleigh signal at the Raman shifted wavelength. For experimental convenience we used the Raman signal, recorded prior to heating the fibre, as our reference for normalisation and hence compensation for splice and fibre losses.

The temperature profile due to Raman power measurement along the fibre can be obtained using the measured Raman power change as follows:

$$\Delta T_R(L) = \frac{\Delta P_R(L)}{K_{RT}^P} \tag{4.6}$$

Where L is the distance along the fibre, $\Delta P_R(L)$ is the normalised change of Raman power, and K_{RT}^P is the temperature coefficient of the Raman power. The Brillouin frequency shift is dependent on both temperature and strain, and, by measuring Brillouin frequency shift and using the now known temperature, the strain profile along the fibre is given by:

$$\Delta\varepsilon(L) = \frac{\Delta\nu_B(L) - K_T^\nu \Delta T_R(L)}{K_\varepsilon^\nu} \tag{4.7}$$

Where $\Delta\nu_B(L)$ is the Brillouin frequency shift along the sensing fibre referenced to room temperature and zero strain, K_T^ν and K_ε^ν are the temperature and strain coefficients for the Brillouin frequency shift, respectively. These coefficients are taken to be 1.07MHz/ °C for temperature and 0.048MHz/$\mu\varepsilon$ for strain in standard SMF as measured in Section 4.2.

4.4.3 Experimental Details and Measurements

The experimental set-up for measuring temperature and strain simultaneously, using both spontaneous Brillouin and Raman scattering, is shown in Figure 4.10. It is essentially as described previously in Figure 3.2, but with an additional WDM (1450/1550) and Bragg grating BG2 to allow measurement of the Raman signal.

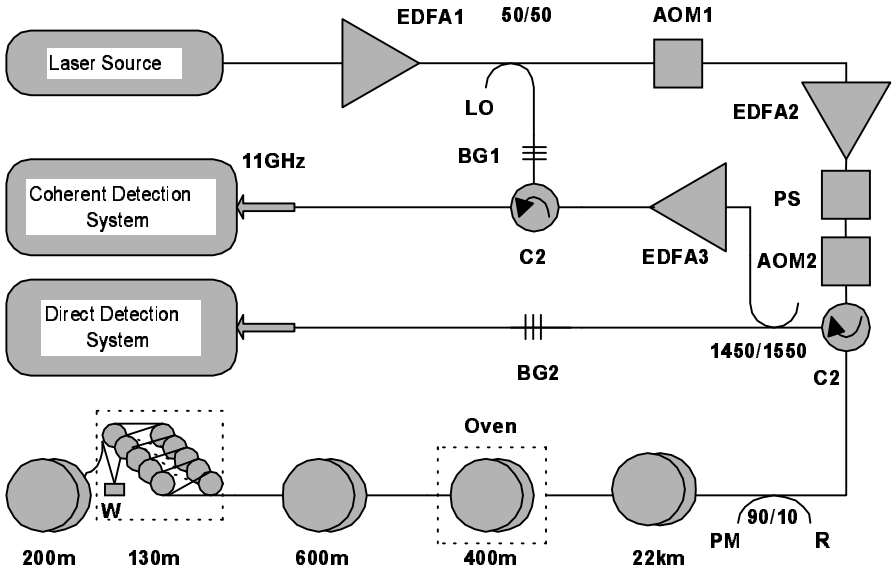

Figure 4.10: *Experimental set-up for measuring both spontaneous Raman power and Brillouin frequency shifts.*

Two detection systems were employed; a direct detection system was used to spatially resolve the Raman anti-Stokes power, and coherent detection was used to spatially resolve the Brillouin frequency shifts. In the direct detection measurement of the Raman signal, a 1550/1450 WDM was used to provide some initial filtering of the 1533.2nm Rayleigh signal from the anti-Stokes Raman signal. The Rayleigh signal was ∼30dB bigger than the Raman anti-Stokes, so a fibre Bragg grating (BG2) (*reflectivity = 99%,* $\Delta\lambda_g$ *= 1nm,* λ_g *= 1533nm*) was placed before the detector to provide further rejection of the backscattered Rayleigh light. The two fibre sections were heated to 60 °C and strained by 1500$\mu\varepsilon$ respectively as in the previous measurements. Initially, the Raman power was measured along the ∼23km with a probe power of ∼1W; then a detailed measurement around the heated and strained sections was performed. The Raman anti-Stokes signal was averaged 2^{15} times and normalised using a trace obtained prior to heating and straining the fibre. The Brillouin frequency shifts due to the combined effect

of both temperature and strain were subsequently measured using a reduced probe power of ∼80mW to avoid any nonlinear effects on the Brillouin signal, such as MI (Chapter 5).

4.4.4 Experimental Results

A plot of the Raman backscatter power measurement at 1450nm over the entire length of the sensing fibre is shown in Figure 4.11; the heated section is visible in the inset figure.

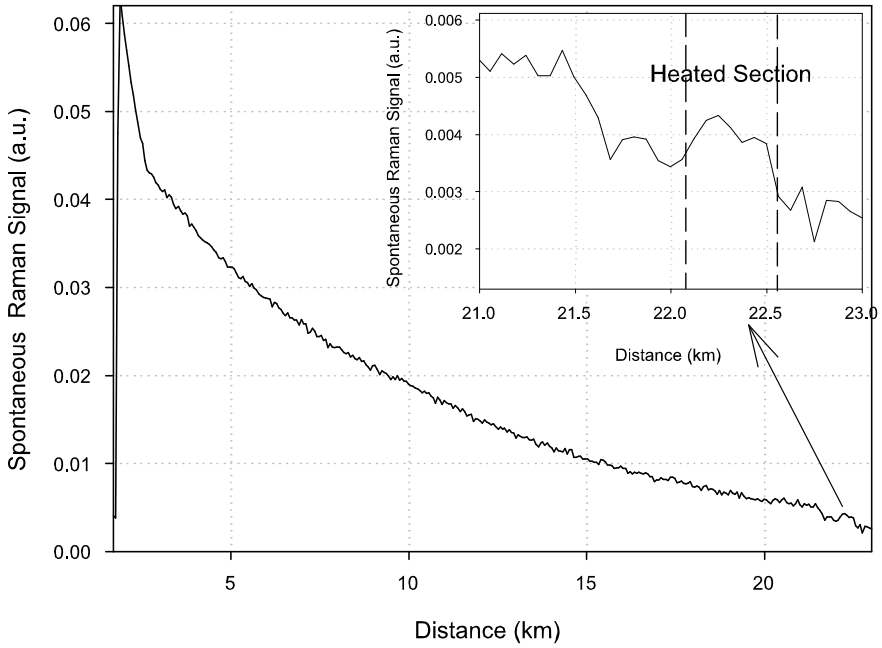

Figure 4.11: *Raman anti-Stokes power trace along the sensing fibre; the heated section is clearly visible at ∼22km.*

Figure 4.12(a) shows an enlarged scale of the normalised Raman power change around the heated and strained sections. The Raman power change at the heated section was measured to be ∼32%, and the RMS percentage resolution was measured to be ∼4.8%. Figure 4.12(b) shows the normalised Brillouin frequency shifts for both the heated and strained sections relative to the unheated and unstrained fibre.

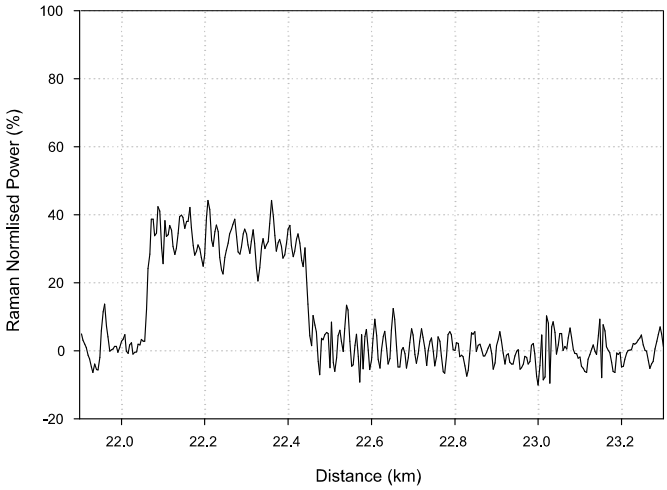

(a) *The Raman anti-Stokes normalised power change.*

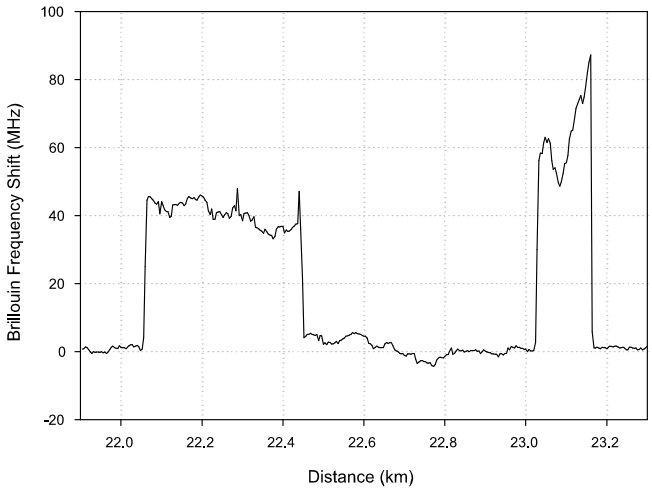

(b) *The Brillouin frequency shift around the heated and strained sections.*

Figure 4.12: *Normalised Raman anti-Stokes power change and the Brillouin frequency shift around the heated and strained sections, respectively.*

Using the Raman power change obtained from the normalised Raman trace and the known Raman anti-Stokes temperature coefficient of 0.80%/ °C, the temperature profile was obtained, as shown in Figure 4.13(a). The temperature change at the heated section was calculated using equation 4.6 and was found to be ∼39 °C.

Using this temperature information and the Brillouin frequency shift data from Figure 4.12(b), the strain profile was derived using equation 4.7, as shown in Figure 4.13(b).

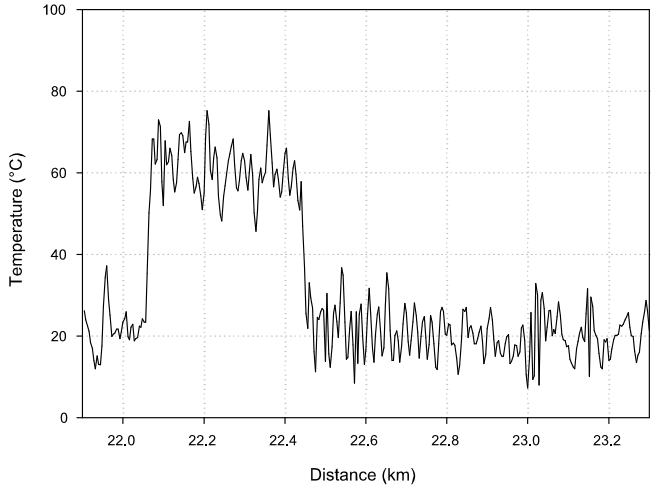

(a) *Derived temperature profile.*

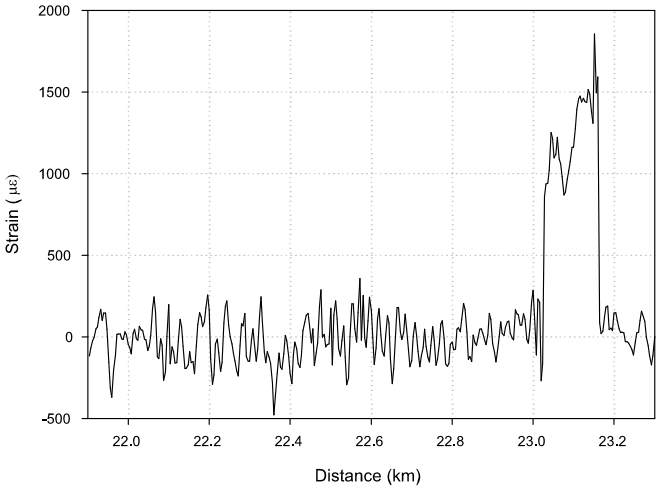

(b) *Derived strain profile.*

Figure 4.13: *Derived temperature and strain profile around the heated and strained sections using the combined spontaneous Raman and Brillouin scattering based technique.*

The strained fibre is not uniformly strained, due to friction in the pulley system, as mentioned earlier. The temperature resolution was determined from the Raman power RMS error (Figure 4.12(a)) and found to be $\sim$6 °C. The strain resolution was determined from the data of figure 4.13(b) and found to be $\sim 150\mu\varepsilon$.

4.4.5 Discussion

The feasibility of using this new technique to measure temperature and strain simultaneously was demonstrated. Despite not currently achieving better results when compared to the Brillouin frequency and power technique, there is scope for improvements. The noise on the temperature and strain measurements mainly arises from the noise associated with the Raman power measurement, and may be reduced by increasing the number of averages. Some of the noise is also thought to arise from contamination of the Raman signal with coherent Rayleigh noise. Improved filtering and further attenuation of the Rayleigh contamination would help to reduce this noise. The contribution to strain errors from errors in the determination of the Brillouin frequency shift is small in comparison to the noise in the Raman power measurements; the RMS frequency error was evaluated in the 150m reference fibre, and converted to the corresponding temperature and strain errors. It was calculated to be less than $\sim$0.74MHz, which is equivalent to a temperature error of less than 0.7 °C and a strain error of less than 15$\mu\varepsilon$. Commercial Raman DTS systems can now readily achieve 1 °C temperature resolution over this distance [6], so if combined with the Brillouin frequency measurement, this would allow a strain resolution of around 30$\mu\varepsilon$.

4.5 Comparison between Simultaneous Measurements Techniques

In this section, a comparison between the three techniques for measuring temperature and strain simultaneously is presented. Table 4.3 summarises temperature and strain resolutions at 23km for all three techniques.

Table 4.3: *Comparison of temperature and strain resolutions estimated in all three sensing techniques.*

Measurands	**Brillouin Frequency & Power**	**LEAF Peak 1 & 2**	**Spontaneous Raman & Brillouin**
$Temperature(^{\circ}C)$	4	29	6
$Strain(\mu\epsilon)$	120	630	150

Analysis of the temperature and strain resolutions in all three techniques reveals that the Brillouin frequency and power based technique gives the best resolution for both measurands, whilst measurands resolution obtained using the spontaneous Raman and Brillouin based technique is better than those obtained with the multiple Brillouin peaks based technique. The temperature and strain resolutions using the LEAF fibre and the two frequency measurements were $\sim$7 and $\sim$5 times worse than that achieved using the Brillouin frequency and power measurements. The temperature and strain resolution using the spontaneous Raman and Brillouin signal were $\sim$1.5 and $\sim$1.2 times worse than those achieved using Brillouin frequency and power measurements. It is concluded that distributed fibre sensors based on LEAF or other fibres with multiple Brillouin peaks provide an exciting new possibility for extending range and accuracy. However, this preliminary investigation to compare the performance of the dual frequency analysis of the Brillouin spectrum to the peak frequency and power analysis of Brillouin spectra in SMF proved that there was no advantage of using such a technique at present. The feasibility of the spontaneous Raman and Brillouin based technique was demonstrated, and it may prove suitable, especially if combined with commercial Raman DTS. In fact, the large input power and high temperature sensitivity make the Raman technique

worth consideration for combined sensor applications at medium ranges. However, for a combined long range sensor >30km, the Brillouin frequency and power technique is considered to be the best candidate so far.

4.6 Conclusions

Three different techniques for measuring distributed temperature and strain simultaneously were investigated and compared. Analysis of the two frequency components of the LEAF fibre to determine temperature and strain produced almost seven fold deterioration in the temperature resolution from 4 °C to ∼29 °C, and more than a five fold deterioration in the strain resolution compared to the Brillouin frequency and power based technique in SMF. Raman anti-Stokes power was used to measure the temperature and is independent of the strain, and this, combined with the Brillouin frequency shift measurement, allows the strain information to be determined. The results of this technique are encouraging and demonstrate its feasibility, with Raman sensitivity and higher input power making this technique worth considering, for example, combined with commercially available DTS. The best measurand resolutions obtained were with the Brillouin frequency and power based technique measured in SMF. This technique may be used in longer sensing range, provided that the accuracy of the power measurement can be improved. One obvious way is to launch a higher pulse power, as the signal strength is directly proportional to the pulse power. The next chapter investigates in detail the nonlinear effects that limit the launched pulse power and investigates a possible solution.

Bibliography

[1] S. M. Maughan, H. H. Kee and T. P. Newson, "Simultaneous Distributed Fibre Temperature and Strain Sensor using Microwave Coherent Detection of Spontaneous Brillouin Backscatter," *Measurement Science and Technology*, vol. 12, p. 834, February 2001.

[2] J. D. C. Jones, "Review of Fibre Sensor Techniques for Temperature-Strain Discrimination," *12th International Conference on Optical Fiber Sensors Technical Digest (OFS)*, vol. 16, p. 36, October 1997.

[3] C. C. Lee, P. W. Chiang, and S. Shi, "Utilization of a Dispersion-shifted Fiber for Simultaneous Measurement of Distributed Strain and Temperature Through Brillouin Frequency Shift," *IEEE Photonics Technology Letters,*, vol. 13, no. 10, pp. 1094–1096, October 2001.

[4] N. Shibata, R. G. Waarts and R. P. Braun, "Brillouin-gain Spectra for Single-mode Fibers Having Pure-silica GeO_2-doped and P_2O_2-doped Cores," *Optics Letters*, vol. 12, no. 4, p. 269, April 1987.

[5] A. H. Hartog, A. P. Leach, and M.P. Gold, "Distributed temperature sensing in solid-core fibres," *Electronics Letters*, vol. 21, no. 23, p. 1061, November 1985.

[6] *Distributed Temperature Sensor-DTS800*, SENSA, www.sensa.org.

Chapter 5

The Influence of Modulation Instability on Spontaneous Brillouin Based Sensors

5.1 Introduction

In the previous chapter, it was concluded that the Brillouin frequency and power based technique provides the best sensing results when compared to other techniques using standard SMF and its performance is expected to improve further provided that accurate measurement of the Brillouin power can be achieved. The Brillouin power accuracy is greatly dependent on the strength of Brillouin backscattered signal which in turns is proportional to the pulse energy within the sensing fibre. The pulse energy depends on the pulse peak power and width. However, the pulse width is limited by the spatial resolution requirement and the pulse power is limited by the need to avoid nonlinear effects. Typical nonlinear effects that affect spontaneous Brillouin based sensors in SMF are stimulated Raman scattering, stimulated Brillouin scattering, self-phase modulation, four wave mixing and modulation instability. This chapter initially reviews the nonlinear effects, and, since modulation instability was found to have the lowest threshold, this is then investigated in greater detail.

5.2 Nonlinear Effects on BOTDR Based Sensors

Nonlinear effects in Brillouin Optical Time Domain Refractometry (BOTDR) based sensors distort the backscattered trace either directly or via probe spectral broadening and/or depletion of its power. Probe spectral broadening occurs when part of the Rayleigh signal is spread to the Brillouin signal due to the small separation (∼11GHz) between Brillouin and Rayleigh signals. As a result, Brillouin sensitivity to temperature and strain is degraded. Probe power depletion occurs when some of the probe energy is transferred to generate other signals at different wavelengths. As the probe signal becomes weaker, so does its backscattered light, hence limiting its sensing range and accuracy. This section reviews the major nonlinear effects in BOTDR based sensors and theoretically approximates their power thresholds.

5.2.1 Stimulated Raman and Brillouin Scattering

In Brillouin based OTDR systems, when the pulse power approaches a certain threshold, SRS/SBS amplification will occur, and the pulse power is significantly transferred to the Stokes signals. Therefore it is important to keep the pulse power below this nonlinear threshold. The threshold pump power for SRS/SBS is defined as the input pump power required, such that the Stokes power becomes equal to the pump power at the fibre output. The SRS/SBS threshold powers in SMF can be approximated using [1] [2]:

$$P_{R,B}^{th} \cong \frac{C_{r,b} K A_{eff}}{g_{r,b} L_{eff}} \tag{5.1}$$

Where $C_{r,b}$ is a constant, 16 and 21 for Raman and Brillouin respectively, A_{eff} is the effective area which is calculated to be approximately $80\mu\text{m}^2$ for conventional silica fibres [3], the term K is a polarisation factor and its value, between 1 and 2, depends on the polarisation of the pump and Stokes waves, its value will be assumed to be 1 in the subsequent calculations. L_{eff} is the effective length of the fibre and g_b is the Brillouin gain coefficient ($\sim 5\times10^{-11}$ m/W) at 1550nm [2]. g_r is the Raman gain coefficient which was reported to have a value of ($\sim 1\times10^{-13}$ m/W) at 1064nm and can be approximated

at other wavelengths, related by [2]:

$$g_r(\lambda_p) = \left(\frac{1064nm}{\lambda_p}\right)(1.0 \times 10^{-13}) \tag{5.2}$$

Using equation 5.2 for $\lambda_p = 1550$nm gives $g_r \sim 7 \times 10^{-14}$m/W. The effective interaction length for the Brillouin scheme is half the pulse width, as both the pump wave and Brillouin backscattered wave are counter-propagating. However, in the case of Raman, the effective interaction length results from the forward propagation of the pump and Raman signals, and is given by equation 5.3:

$$L_{eff} = \frac{1}{\alpha_p}(1 - e^{-\alpha_p L}) \tag{5.3}$$

Where α_p is the absorption coefficient of the pump pulse in the sensing fibre ($\alpha_p \cong 4.5 \times 10^{-5}\text{m}^{-1}$ at 1550nm) and L is the length of the sensing fibre. As the pump and Raman Stokes wavelengths are separated by a large frequency difference (∼13THz), another effect becomes dominant when calculating the effective length for SRS threshold power. This effect is due to the significant wavelength difference between the pump and Stokes signal; the difference in group velocities at the two wavelengths leads to a pulse walk-off, i.e. the pump and probe pulses move apart as they travel down the fibre. This walk-off length is calculated by [4], using the equation:

$$L_w = \frac{W}{D\triangle\lambda} \tag{5.4}$$

Where W is the pump pulse width, D is the fibre dispersion parameter (∼17 ps/nm.km in SMF at 1550nm), and $\triangle\lambda$ is the wavelength separation between the pump and signal (∼100nm). Figure 5.2 illustrates both the effective length due to fibre loss and the walk-off length as a function of pulse width.

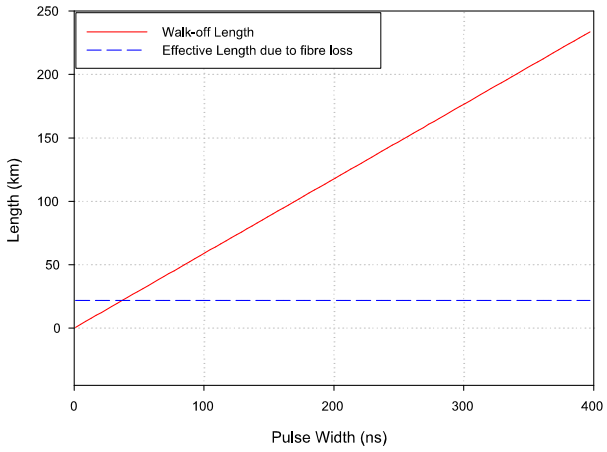

Figure 5.1: *Variation of the effective length due to fibre loss and the walk-off length with a sensor pulse width modelled for 100km fibre length. Both lengths have the same value, around ∼35ns, and for shorter pulse widths the walk-off length dominates the SRS threshold power.*

For a pulse width of ∼35ns, the effective and the walk-off lengths are equal. The significance of this is that, for pulse widths less than ∼35ns, the SRS power threshold is dictated by L_w but above that value it is dictated by L_{eff}. Both SRS and SBS place a constraint on the maximum power that can be launched into the sensing fibre and, by using equation 5.1, their power thresholds can be approximated at any pulse width, provided the fibre length is known. Figure 5.2 illustrates SRS and SBS threshold powers as a function of pulse width, modelled for 100km fibre length.

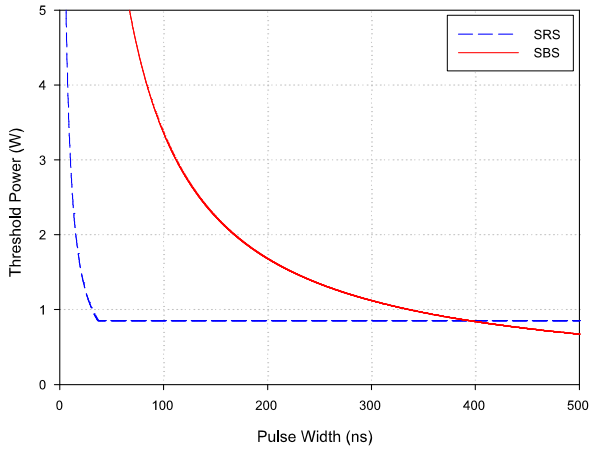

Figure 5.2: *Raman and Brillouin threshold powers as a function of pulse width modelled for 100km fibre length.*

Figure 5.2 shows that, as the pulse width is reduced, the threshold value is governed by the stimulated Raman threshold, which increases to about 3W for 10ns pulses, corresponding to a spatial resolution of 1m. Both scattering processes, SRS and SBS, had a similar threshold power of about 860mW for input pulse widths of ∼390ns, corresponding to a spatial resolution of ∼39m. Beyond this pulse width, the threshold power is determined by the SBS effect. The effective length for Raman scattering (Equation 5.3) initially increases with fibre sensor length, gradually tending to a constant value of $(\frac{1}{\alpha_p})$ for very long lengths, i.e. $\alpha_p L \gg 1$; hence the Raman threshold power becomes almost independent of the long sensing length. The Brillouin threshold power is likewise unaffected by sensing length, because it is a function of pulse width only, assuming the pulse width is very much less than the fibre length.

5.2.2 Self-Phase Modulation and Four Wave Mixing

Self-phase modulation is a phenomenon that leads to spectral broadening of optical pulses [2]. It occurs because the refractive index is power dependent and hence varies in a single pulse of light. As a result, the phase of the light waves that make up the pulse changes, leading to change in frequency; thus the pulse is spread out and distorted. This effect produces a broadened Rayleigh signal that eventually overlaps with the Brillouin signal, which hence becomes less sensitive to measurand variations. The threshold power of SPM along the fibre can be approximated as follows [2]:

$$P_{spm}^{th} = \frac{\phi_{\max}}{\gamma L_{eff}} \tag{5.5}$$

Where γ is the nonlinear parameter given by:

$$\gamma = \frac{2\pi\nu_o n_2}{cA_{eff}} \tag{5.6}$$

Where n_2 is the nonlinear index, typically $\sim 2.2\times10^{-20}$ $\mathrm{m^2W^{-1}}$ [5], ν_o is pump frequency, A_{eff} is fibre effective area and c speed of light. For standard SMF at λ=1550nm, with an effective area of $80\mu\mathrm{m}^2$, the nonlinear parameter $\gamma \simeq 1.1\mathrm{W^{-1}km^{-1}}$.

The $\phi_{\max}$ in equation 5.5 is the maximum phase shift given by [2]:

$$\phi_{\max} = \frac{1.16\kappa}{W} \tag{5.7}$$

Where κ is the broadening factor and W is the pump pulse width. In order to estimate the SPM threshold power for this application, it is defined as the power that broadens the probe spectrum to >1GHz. Using equation 5.5, the SPM threshold power can be calculated as a function of fibre length for certain pulse widths or vice versa. Figure 5.3 illustrates the SPM threshold for both cases.

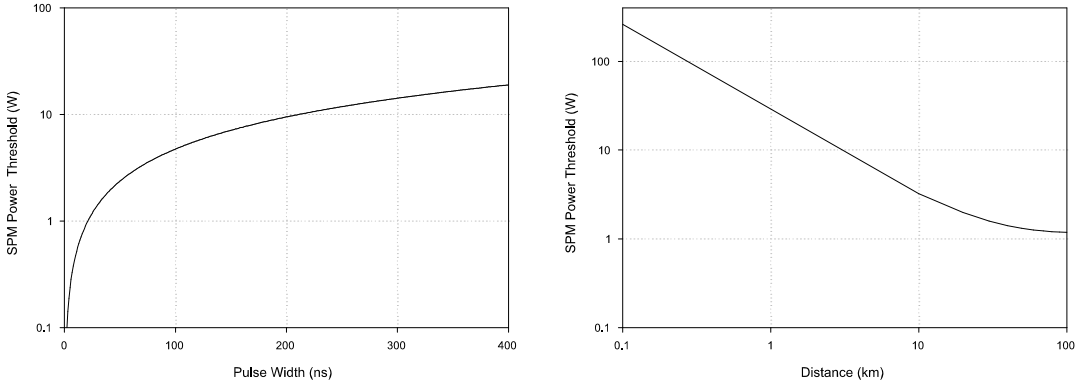

(a) *Threshold power of SPM versus pulse width modelled for 100km fibre length.*

(b) *Threshold power of SPM versus fibre length modelled for 35ns pulse width.*

Figure 5.3: *Theoretical analysis of SPM threshold power versus fibre length and pulse width modelled for 35ns pulse width and 100km fibre length, respectively.*

For a short pulse width, less than ∼25ns, SPM occurs at a relatively low power compared to SRS and SBS (Figure 5.2). For a pulse width of ∼1ns, the SPM power threshold is calculated to be ∼50mW. This value increased to ∼1.2W at a pulse width of ∼25ns (Figure 5.3(a)). For the same pulse width and at 100km sensing length, SPM threshold is approximated to be ∼1.2W, as can be seen in Figure 5.3(b).

Another nonlinear phenomenon that may degrade Brillouin based sensors employing EDFAs and narrow pulse width signals is four wave mixing. The process of FWM is where beams of frequency w_1 and w_2 are mixed through action of third order susceptibility to produce output at frequency $2w_1 - w_2$. FWM gives rise to new frequencies located either side of the Rayleigh frequency. It was reported [6] that for a high power, narrow-band sensing pulse with residual ASE, FWM is believed to cause pump depletion, which leads to weak backscattered light, hence limited sensing range and accuracy. A preliminary investigation of the nonlinear effects in BOTDR based sensors [7] has led to include this.

5.2.3 Modulation Instability

Modulation instability is a nonlinear process that operates in the anomalous dispersion regime where small amplitude and phase perturbations grow rapidly under the combined effects of nonlinearity and dispersion [8][9]. In such processes, during propagation the optical beam induces spectral sidebands situated symmetrically around the initial frequency of the pulse which grow with power and distance along the fibre. Due to the small frequency difference between Brillouin and Rayleigh, these sidebands contaminate the Brillouin signal leading to poor measurand resolution. Our investigation identified MI to have the lowest threshold in our applications and this is analysed in some detail in the following sections.

5.3 Theoretical Investigation of Modulation Instability in BOTDR Based Sensors

In this section, the influence of MI on spontaneous BOTDR based sensors is investigated theoretically. Firstly, a theoretical analysis of the origin of MI and its behaviour in lossless fibre is undertaken, and then its gain and critical frequency in lossy fibres are evaluated and introduced.

5.3.1 Introduction

In distributed temperature and strain sensors, based on spatially resolving the frequency and power of the spontaneous backscattered anti-Stokes Brillouin signal along the sensing length, MI effect is detrimental to the measurement. Operating at 1550nm, the Brillouin backscattered signal is typically about ∼11GHz from the pulse frequency. The MI induced sidebands in the pulse's spectrum lead to a broadening of both the backscattered Rayleigh and Brillouin signals. Any overlap of these spectra prevents accurate determination of, in particular, Brillouin power. Initially it was considered that stimulated Raman, stimulated Brillouin scattering and Self-phase modulation were the nonlinear effects that limit the permissible input powers. It is now identified that in long range sensors, using standard SMF, operating at 1550nm, MI has a much lower threshold. However, MI is only present in anomalous dispersion fibre and so by using fibre with negative dispersion at 1550nm such as NZ-DSF, this limitation is overcome, and a much higher pulse power can be launched safely. In fact, this opens the door for exploring opportunities arising from advances made in fibres, originally designed to handle higher power for the telecommunications industry, being used in sensing applications.

5.3.2 Analysis of Modulation Instability

For further insight and to gain understanding, the modulation instability phenomenon may be explored mathematically by considering the nonlinear Schrodinger equation, with the assumption that the fibre is lossless [2]:

$$i\frac{\partial A}{\partial L} = \frac{\beta_2}{2}\frac{\partial^2 A}{\partial^2 L} - \gamma |A|^2 A \tag{5.8}$$

Where $A(L,t)$ is the amplitude of the pulse envelope, β_2 and γ are broadening and nonlinear parameters respectively. In the case of CW radiation, the amplitude A is independent of time (t) at the fibre front end ($L = 0$). A steady state solution from equation 5.8 can be obtained if $A(L,t)$ is assumed to be independent of t during propagation along the fibre:

$$\widetilde{A} = \sqrt{P_o}\exp^{i\phi_{LN}} \tag{5.9}$$

Where P_o is the incident power at $L = 0$, and the nonlinear phase shift is given by:

$$\phi_{NL} = \gamma P_o L \tag{5.10}$$

The steady state solution suggests that CW light should propagate through the fibre unchanged rather than having a power phase shift and power reduction if fibre loss is present. However, the steady state solution is not stable against small perturbations. If the steady state solution is perturbed slightly, such that the amplitude A becomes:

$$A = (\sqrt{P_o} + a)\exp^{i\phi_{LN}} \tag{5.11}$$

And if the weak perturbation $a(L,t)$ evolution replaces $A(L,t)$ in equation 5.8, assuming a general solution of such an equation, the weak perturbation wave number k_p and critical frequency ω_c ($\omega_c = 2\pi f_c$) can be obtained as follows:

$$k_p = \pm\frac{1}{2}|\beta_2|\,\omega\sqrt{(\omega^2 + sgn(\beta_2)\omega_c^2)} \tag{5.12}$$

$$\omega_c^2 = \frac{4}{|\beta_2|\,L_{LN}} = \frac{4\gamma P_o}{|\beta_2|} \tag{5.13}$$

Equation 5.12 shows that the stability of the steady state depends on whether the pulse experiences normal or anomalous group velocity dispersion. In the case of normal dispersion ($\beta_2 > 0$, $\lambda < \lambda_d$) where ($\lambda_d \cong$1300nm represents zero dispersion), the steady state is stable against small perturbations. However, in the case of anomalous group velocity dispersion ($\beta_2 < 0$, $\lambda > \lambda_d$), the perturbation grows exponentially with L. Analysis of the nonlinear Schrodinger equation 5.8, for anomalous lossless fibre, yields the following key results [2]: The gain at a frequency ω from the critical frequency ω_c of the launched pulse is given by:

$$G(\omega) = |\beta_2 \omega| \sqrt{(\omega_c^2 - \omega^2)} \tag{5.14}$$

Equation 5.14 represents the gain at the frequency $\omega_o \pm \omega$ for a perturbation shifted by ω from the incident frequency ω_o, and it only exists for $|\omega| \leq \omega_c$. Figure 5.4 illustrates MI gain when the input power was varied from 100mW to 400mW.

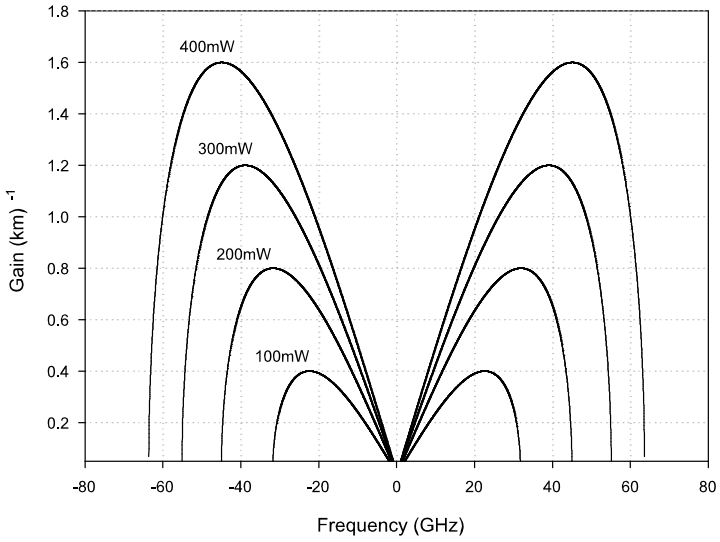

Figure 5.4: *Modulation instability gain in lossless fibre computed using equation 5.14 with various input powers from 100 to 400mW, in steps of 100mW.*

The maximum gain will occur at two frequencies, which are given by:

$$\omega_{\max} = \pm \frac{\omega_c}{\sqrt{2}} = \pm \left(\frac{2\gamma P_o}{|\beta_2|} \right)^{\frac{1}{2}} \tag{5.15}$$

By substituting the maximum frequency in the gain expression (Equation 5.14), the maximum MI gain becomes $G_{max} = 2\gamma P_o$ and increases linearly with the incident power [2]. In Brillouin based sensors, when the f_c exceeds ~11GHz as a result of higher input power/fibre length, MI gain leads to contamination of the Brillouin signal by the broadened Rayleigh backscattered light.

5.3.3 Modulation Instability Gain and Critical Frequency

The MI gain spectrum changes along the fibre as a result of fibre loss and CW or quasi-CW beam power depletion. The power depletion can generally be neglected unless the sidebands are strongly seeded and the gain profile along the fibre is determined by the local pulse power that decreases with distance. When fibre loss is taken into account, the previously calculated critical frequency ω_c, is replaced by $(\omega_c \exp^{-\alpha L/2})$ where α is the attenuation factor ~0.045km^{-1}and L is the fibre length. As a result, ω_c varies along the fibre length eventually decreasing to 0 as the fibre length goes to infinity [8]. Using the expressions provided by Hasegawa *et al.* [9], the spatially integrated gain and the critical frequency along standard SMF were computed. Figures 5.5 and 5.6 illustrate respectively the evolved MI gain and critical frequency along standard SMF fibre modelled for a 30km fibre length.

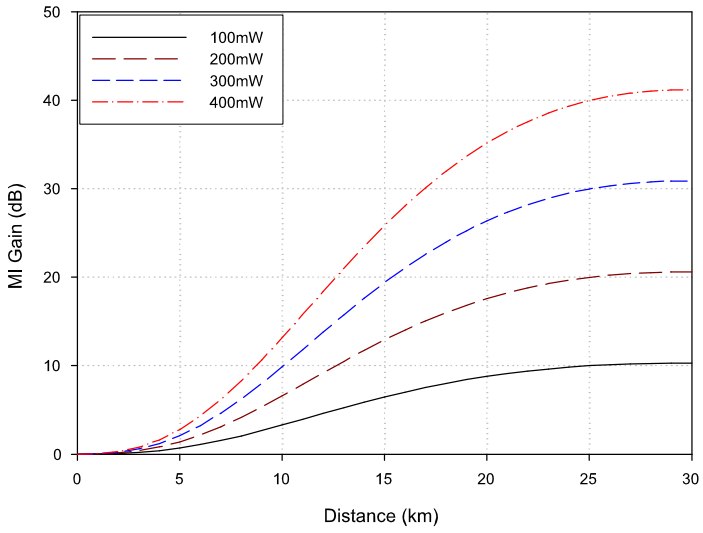

Figure 5.5: *Spatially integrated gain versus distance along standard SMF, modelled for launched pulse powers from 100 to 400mW, in steps of 100mW.*

It can be seen from Figure 5.5 that MI gain becomes larger as the input power and/or fibre length increases, and at around 25km asymptotically reaches a constant value due to pump depletion and/or fibre attenuation. The MI integrated gain can be approximated from Figure 5.5 to be ∼35dB at fibre length of 20km for a launched power of ∼400mW.

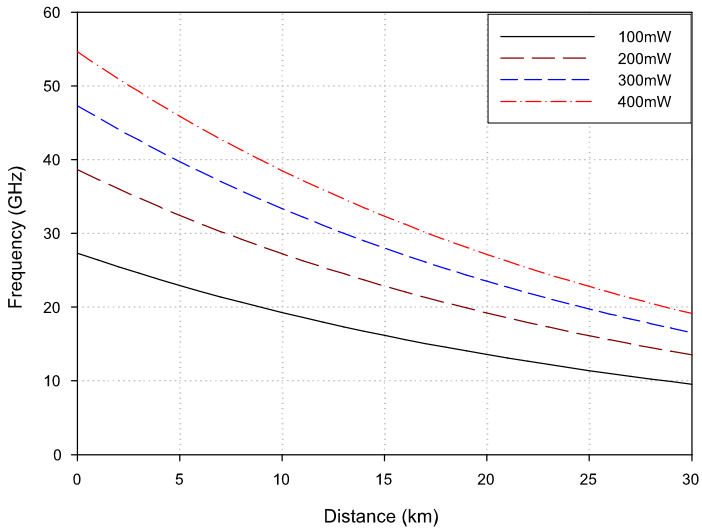

Figure 5.6: *Spatially integrated MI critical frequency versus distance along standard SMF, modelled for launched pulse powers from 100 to 400mW, in steps of 100mW.*

It is shown in Figure 5.6 that the critical frequency decreases as the fibre length is increased or the launch power is decreased. For a fibre length of ∼20km, the critical frequency is approximately ∼28GHz for a launched power of 400mW.

5.3.4 Discussion

Clearly, modulation instability can lead to contamination of the detected Brillouin signal when operating in the anomalous dispersion regime using standard SMF at 1550nm. This contamination is seen as an upward drift in the "Brillouin" signal along the fibre and translates to an upward drift in temperature along the fibre. In order to validate the MI effect, it was experimentally investigated in two different sensing fibres. Results were compared and are reported in the next section.

5.4 Experimental Investigation of Modulation Instability in Different Sensing Fibres

5.4.1 Introduction

In this section, the MI effect was investigated and compared in sensing fibres that have different dispersion regimes at 1550nm. Around 20km of both standard SMF and NZ-DSF MetroCor^{TM} Fibre[1] (MCF) were used as a sensing medium for distributed temperature measurements. The MI effect on temperature resolution in both fibres was investigated, compared and reported. The characteristics of these sensing fibres are summarised in Table 5.1, according to the specifications provided by the manufacturers.

Table 5.1: *Comparison of the characteristics of SMF and MCF fibres at 1550nm.*

Fibre Type	**Fibre Loss** (dB/km)	**Effective Area** (μm^2)	**Dispersion** (ps/km.nm)
SMF	≤ 0.20	~ 80	$+17$
MCF	≤ 0.25	~ 50	-1.384

It can be seen from Table 5.1 that MCF has higher fibre loss and smaller effective area compared to SMF. However, the MCF dispersion is negative; hence, the MI effect is expected to be overcome using such a fibre

[1] Available from Corning^{TM}.

5.4.2 Experimental Details and Measurements

The experimental set-up for measuring the MI effect in a spontaneous Brillouin based sensor using different sensing fibres is shown in Figure 5.7.

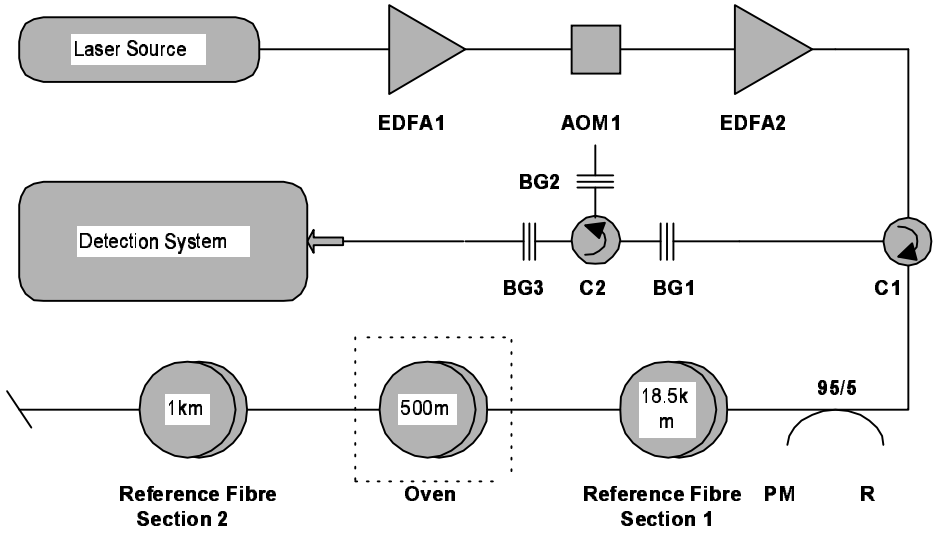

Figure 5.7: *Experimental configuration for measuring MI effects in different sensing fibres.*

Modulation instability was first demonstrated using a source consisting of a distributed feedback laser operating at 1533nm, linewidth <10MHz, amplified by EDFA1, gated using AOM1 and then further amplified using EDFA2. A pulse width of 100ns was used and the output power was varied from 100-400mW. A series of power spectra were measured using an optical spectrum analyser[2] at the output end of 20km for each fibre as a function of the input pulse power. The influence of MI on the detected Brillouin backscattered trace was then measured in the SMF and finally distributed temperature measurements using both fibres were performed, using the principle of BOTDR and direct detection of the power of the Brillouin signal [10] over a distance of 20km. The Brillouin signal was optically filtered from the Rayleigh signal by thermal tuning of two identical fibre Bragg gratings, BG1 and BG3 with reflectivity >99% and an optical bandwidth of 0.1nm, to the wavelength of the pulse. BG2 was used to gate any residual amplified spontaneous emission generated by the EDFAs. The optical bandwidth of BG2 was 1nm with a centre wavelength of 1533nm and reflectivity >96%. In both cases, the majority of the selected fibre was maintained at room temperature and around 500m of

[2]Hewlett Packard, model: 86142A.

the fibre was placed in an oven and heated to 60 °C. MI was evaluated by measuring the probe optical spectrum in each fibre at different input powers. Then both the power of the Brillouin and Rayleigh signals along both sensing fibres were measured with 2^{15} averages and 10m spatial resolution. The Rayleigh signal was measured using a second broadband (∼3nm) pulsed source to avoid significant coherent Rayleigh noise. The Brillouin signal was then divided by the Rayleigh signal to account for any splice and fibre loss. Using the relative Brillouin power temperature coefficients for both fibres, the apparent temperature profiles along the sensing fibre at different input powers were derived and plotted. The MI effect as a function of fibre length and the lowest nonlinear threshold in MCF were also evaluated.

5.4.3 Experimental Results

Figure 5.8 shows the output spectra recorded at the far end of both sensing fibres as the input launch power of the pulse increased.

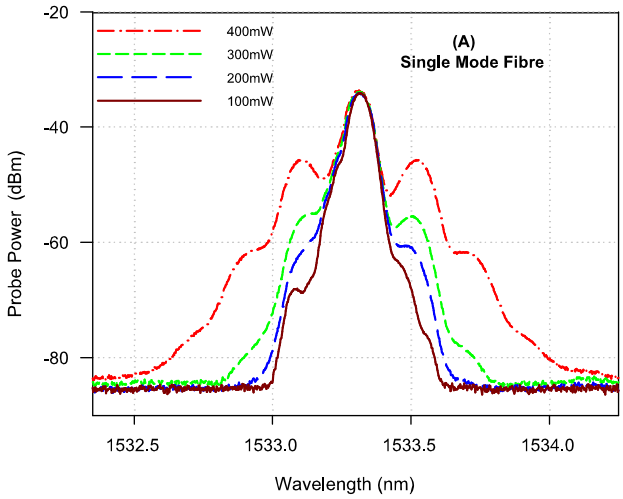

(a) *Pulse spectrum measured in SMF.*

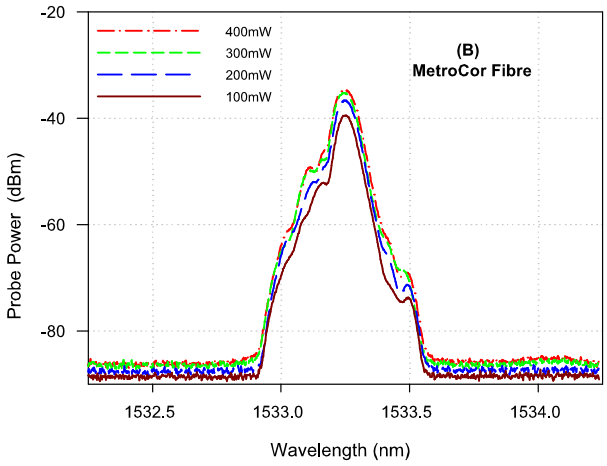

(b) *Pulse spectrum measured in MCF.*

Figure 5.8: *Power spectra for different pulse powers at the output end of the SMF and MCF. The power was increased from 100mW to 400mW, in steps of 100mW.*

In figure 5.8(a), the MI effect becomes more pronounced in SMF as the power increases. Figure 5.8(b) demonstrates the expected absence of the MI effect in the MCF due to its negative dispersion at 1530nm (Table 5.1) and suggests that larger input powers can be safely used. It is worth noting that the pulse spectrum peak in MCF was increased by around 5dB as the input power increased from 100mW to 400mW, without any significant broadening. However, in SMF, as the power increases, the pulse spectrum

peaks do not increase as expected but power is instead transferred to MI sidebands. Using the data from Figure 5.8, the spectrally broadened linewidth was approximated at ∼30dB from the peak in both fibres, and referenced to the unbroadened spectrum measured at 100mW input pulse power. The results are shown in Figure 5.9.

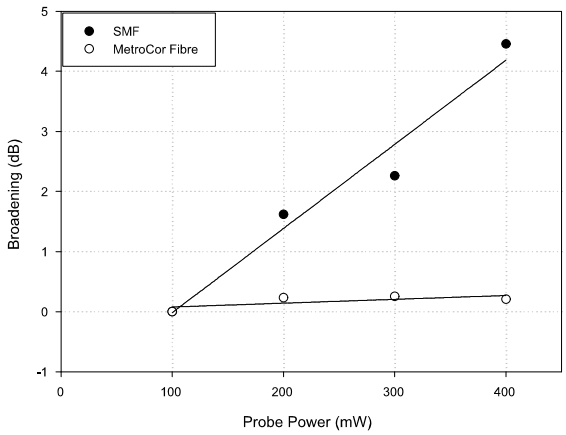

Figure 5.9: *Probe spectral broadening ratio in both fibres approximated using the data of figure 5.8 as referenced to 100mW input pulse power.*

In SMF, the probe spectra were broadened by more than 4dB for input powers from 100 to 400mW. On the other hand, MCF exhibits negligible spectral broadening as input power is increased (Figure 5.9). To calculate the MI gain in the SMF, the measured power spectra in Figure 5.8(a) were normalised by the source spectrum, which was also measured at the far end of the fibre, but at a low input power. The result is shown in Figure 5.10.

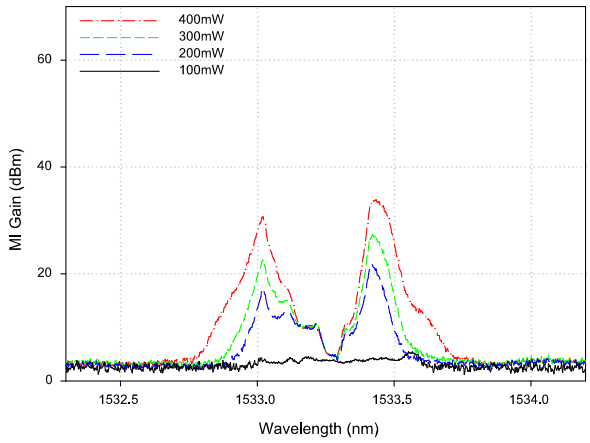

Figure 5.10: *Normalised MI gain spectrum measured at the output end of 20km of SMF for pulse powers from 100 to 400mW.*

Figure 5.10 demonstrates the expected characteristic and distinct MI sidebands. However, there was some asymmetry in the two sidebands, possibly attributed to the source characteristic. The estimate of the peak of MI gain was therefore obtained by taking the peak of the lower sideband. The critical frequency was taken to be one half of the spectral width defined by the distance between the outer limits of the lower and upper sidebands, i.e. where the gain was estimated to have fallen to zero dB. The measured values are summarised in Table 5.2 and compared to the theoretical values computed for figures 5.5 and 5.6 for a fibre length of 20km.

Table 5.2: *The theoretical and measured MI gain and critical frequency in standard SMF.*

$\mathbf{P}_0$ (mW)	$\mathbf{G}_{(\max)\,(\mathbf{Theoretical})}$ (dB)	$\mathbf{f}_{c\,(\mathbf{Theoretical})}$ (GHz)	$\mathbf{G}_{(\max)\ (\mathbf{Measured})}$ (dB)	$\mathbf{f}_{c\,(\mathbf{Measured})}$ (GHz)
400	35	28	30 ± 3	35 ± 7
300	25	24	21 ± 3	30 ± 7
200	16	20	17 ± 3	25 ± 7

It is believed that the different values of the theoretical and measured frequency are within the experimental errors of the measurements, i.e. the resolution of the OSA used in such measurements was limited to ∼60pm or (∼7GHz). The theoretical analysis of MI gain did not take into account power depletion, which may explain the slightly higher theoretical gain values.

The backscattered Brillouin Stokes and anti-Stokes spectra were detected at the front end of the SMF and MCF for different input pulse powers and the results are shown in Figure 5.11.

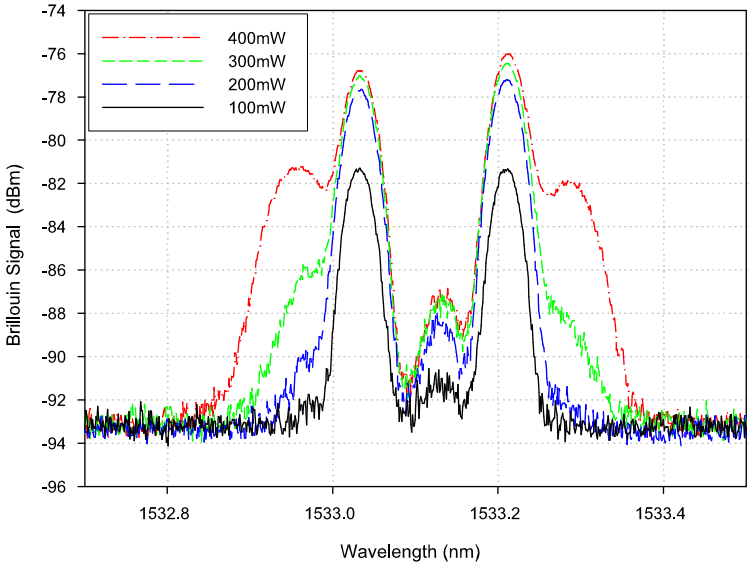

(a) *Brillouin Stokes and anti-Stokes measured in SMF.*

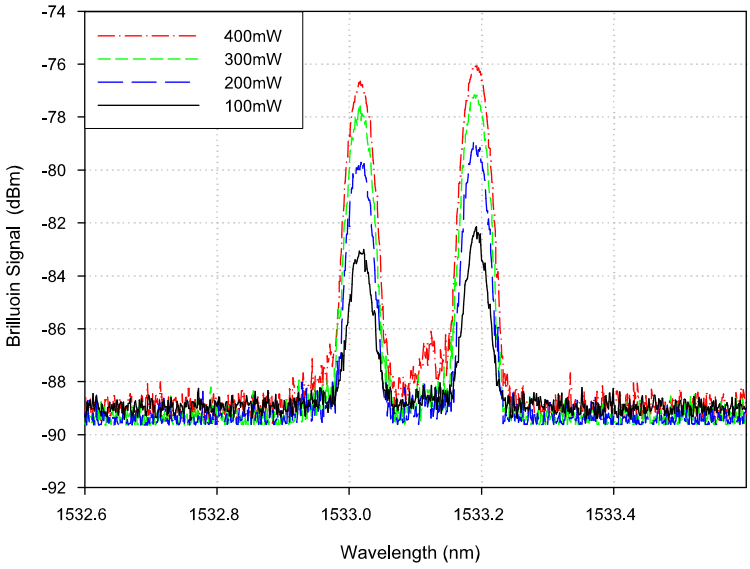

(b) *Brillouin Stokes and anti-Stokes measured in MCF.*

Figure 5.11: *The Brillouin Stokes and anti-Stokes spectra measured at the front end of both fibres for various input pulse powers. The power was increased from 100mW to 400mW, in steps of 100mW.*

In figure 5.11(a), the two largest peaks correspond to the Brillouin Stokes and anti-Stokes signals generated from SMF. The outer peaks are the Rayleigh backscattered signals

from the spectrally broadened pulse. Figure 5.11(b) illustrates the Brillouin Stokes and anti-Stokes signals in MCF. As expected, the Brillouin backscattered light spectrum is free from any broadening. In the SMF, the MI broadened pulse will also generate a broadened Brillouin spectrum (shifted by ∼11GHz) but this will be more than ∼15dB below the peaks due to Rayleigh scattering and hence below the noise floor. Although the peaks of the MI gain do not coincide with the Brillouin peaks, there is sufficient overlap for the measured Brillouin Stokes and anti-Stokes to be contaminated by the Rayleigh scattering from the spectrally broadened pulse. In separate measurements, the MI effect was evaluated at different sensing lengths of the SMF by measuring the probe optical spectrum at certain fibre lengths with fixed input power of 400mW and 100ns pulse width, as illustrated in Figure 5.12.

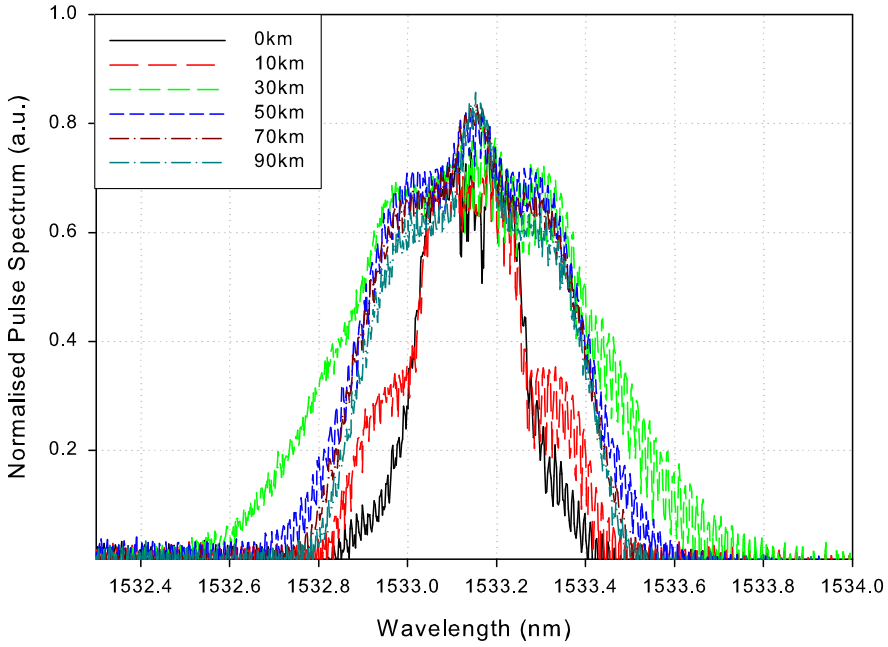

Figure 5.12: *MI effects measured at different sensing lengths in SMF with fixed input power.*

As can be seen from Figure 5.12, at zero length[3], the MI effect has not yet developed. However, as the beam propagates along the fibre, the MI effect grows rapidly. MI gain broadening (*critical frequency*) tends to be reduced with fibre length and this is in close agreement with the theoretical analysis described in 5.3.3.

[3]The front end of the sensing fibre.

Using the data of figure 5.12, the linewidth of probe spectral broadening due to MI was approximated at ∼30dB from the spectrum peak (reference to probe spectrum at 0km) and plotted against fibre length in Figure 5.13.

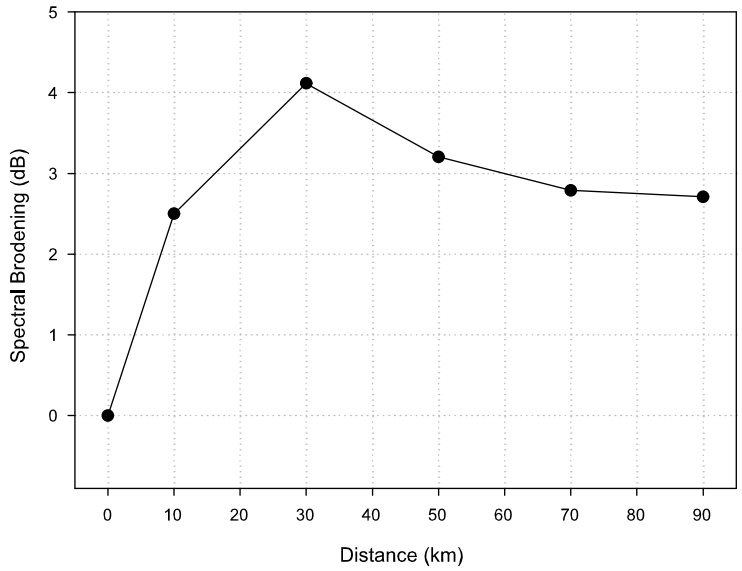

Figure 5.13: *Spectral linewidth broadening at different SMF lengths approximated at ∼30dB from the spectrum peak.*

By considering MI gain at the fibre front end (0km) as a reference, MI seems to have the largest broadening of its gain at ∼30km, and beyond that broadening is reduced.

In order to evaluate and compare the MI effect on temperature resolution in both fibres, distributed temperature measurements were performed. Initially, a characterisation of MCF was performed to evaluate the coefficient of Brillouin power with respect to temperature. Around 500m of MCF at a sensing length of ∼10km was placed in an oven and the Brillouin power was measured at different temperatures, i.e. from 20 to 80 °C, in steps of 20 °C with input power of 100mW and 100ns pulse width. The result is shown in Figure 5.14.

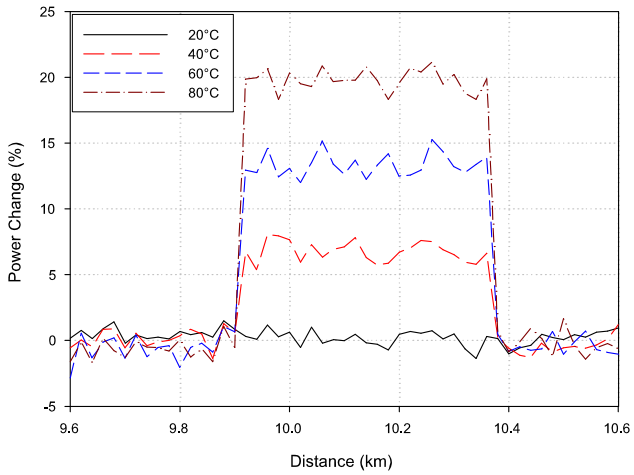

(a) *Brillouin power change at different temperatures.*

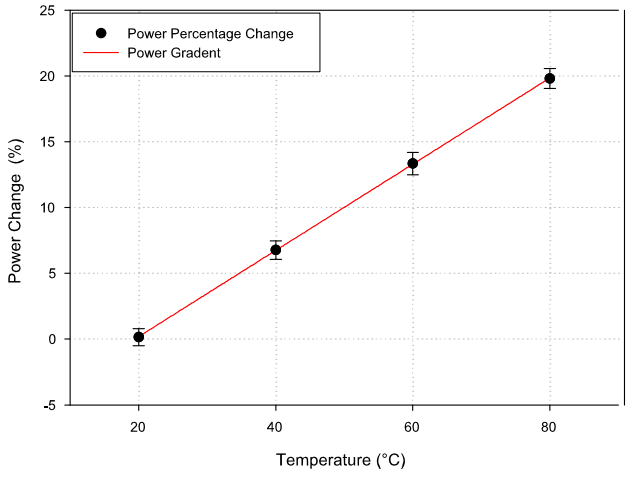

(b) *Gradient of Brillouin power change with temperature.*

Figure 5.14: *Brillouin power change with temperature in MCF. Power was measured at four different temperatures.*

Based on the data in Figure 5.14, the Brillouin power percentage change in MCF with respect to temperature was approximated to ∼0.33%/ °C. This value was used in the

subsequent measurements. After measuring the distributed temperature change along both fibres, the MI effect was clearly visible in SMF. Figure 5.15 shows the effect in both fibres at different launched pulse powers.

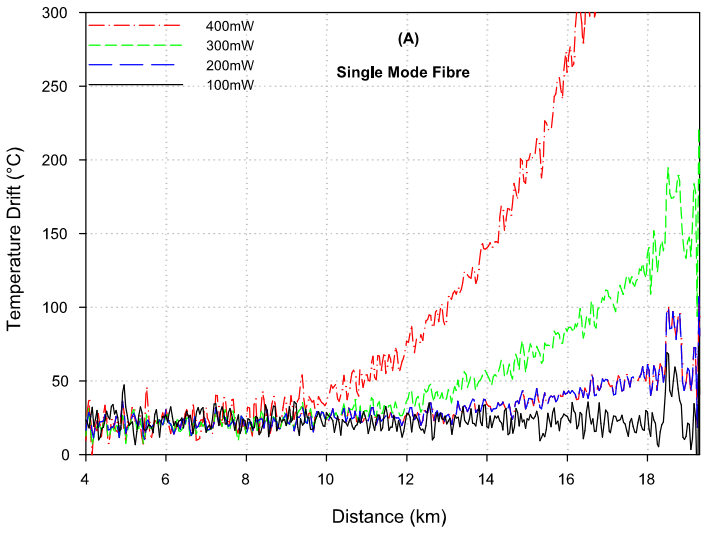

(a) *Temperature drift along SMF.*

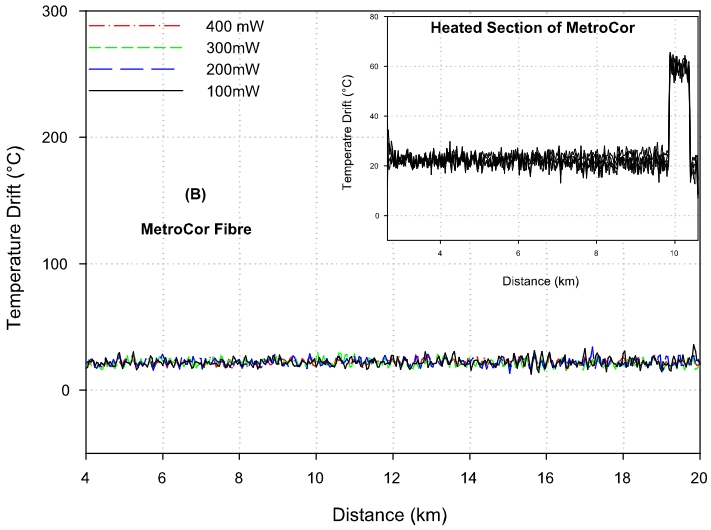

(b) *Temperature drift along MCF.*

Figure 5.15: *Temperature drift along (a) 20km of SMF, (b) 20km of MCF fibre for various launched powers. The inner plot in (b) represents a heated section 10km along the MCF fibre at different input powers.*

Figure 5.15(a) shows how this contamination translates to a drift in the measured temperature along the SMF. The effect is more marked as the launched power is increased

and is only circumvented by limiting the power to around 100mW for a 20km sensing length of SMF. At 400mW pulse power, a temperature error of only a few degrees is observed up to about 8km of SMF, but then increases rapidly to more than 250 °C at 16km. MCF (Figure 5.15(b)) shows a lower temperature error at the front end of the fibre and no evidence of MI induced drift in the temperature measurement along the entire 20km sensing fibre, even when the power was increased up to 400mW. The inset indicates a heated section at 10km along the fibre and confirms that the MCF showed a similar Brillouin power change with respect to temperature (0.33%/ °C) as for SMF. As well as the spatial drift in temperature measurement, the contamination of the Brillouin signal with Rayleigh scattering also produces an increase in the RMS noise in temperature resolution, primarily due to the presence of coherent Rayleigh noise. Figure 5.16 compares the RMS temperature resolution as a function of distance for the two fibres.

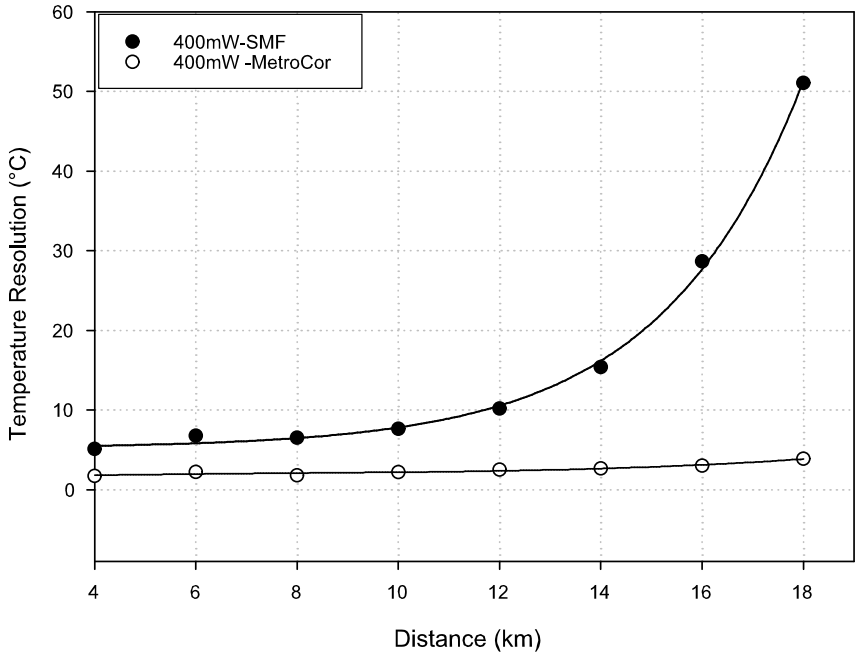

Figure 5.16: *RMS temperature errors measured every 2km and averaged over 500m along the characterised sensing fibres at 400mW launched power.*

The Brillouin power RMS value was calculated over 500m every 2km along the entire sensing length and translated to the corresponding temperature resolution. Figure 5.16 shows that the RMS temperature error in SMF is higher, and increased rapidly with distance (i.e. at 18km the temperature resolution was 52 °C), whereas there is just a

small deterioration in performance with distance using the MCF (i.e., temperature resolution at 18km was ∼4 °C), following the expected loss (∼0.40dB/km) of backscattered signal due to fibre attenuation.

To further explore MCF's ability to handle higher powers, a length of 25km of the MCF and a new light source were used. The pulse optical spectrum was measured at the output end of the MCF at different input powers using an OSA. It was found that the input power could be increased up to almost 1000mW before any significant stimulated Raman scattering was observed. Figure 5.17 illustrates the effect of SRS in MCF as a function of input power.

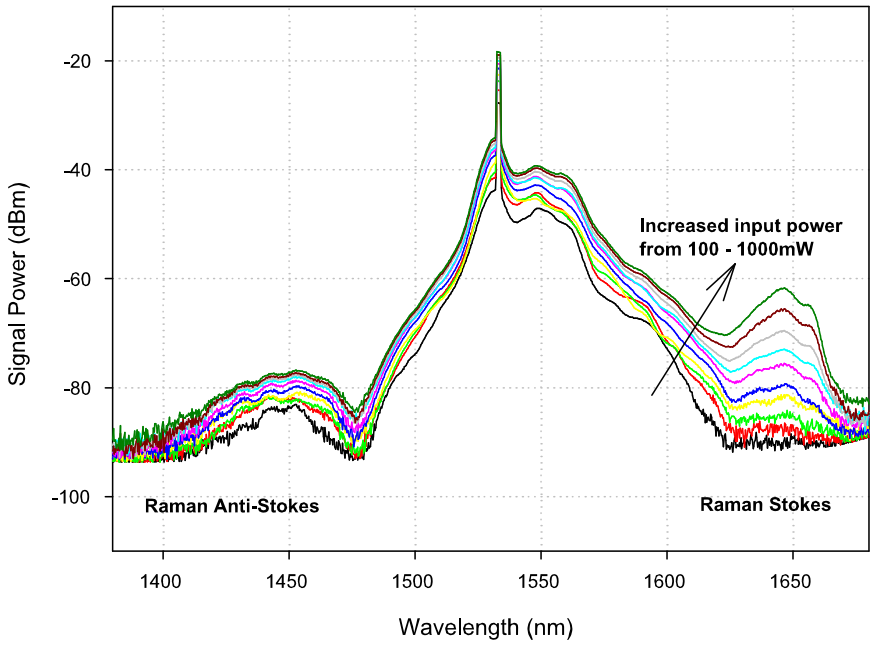

Figure 5.17: *Evidence of stimulated Raman scattering measured at the output end of 25km of MCF at different pulse powers. The input pulse power was increased from 100mW to 1000mW in steps of 100mW*

Figure 5.17 indicates, that as the input power is increased, the Raman Stokes signal at ∼1550nm is increased, which indicates that the pump power starts to be transferred to the Stokes. At a certain input power, defined by the SRS threshold, the pump power is significantly transferred. Using equation 5.1, the theoretical SRS threshold power in MCF was calculated to be ∼880mW for a fibre length of 25km.

The measured SRS threshold power can be found by taking the ratio of the Raman Stokes to anti-Stokes signals versus input pulse power. Figure 5.18 illustrates such a ratio.

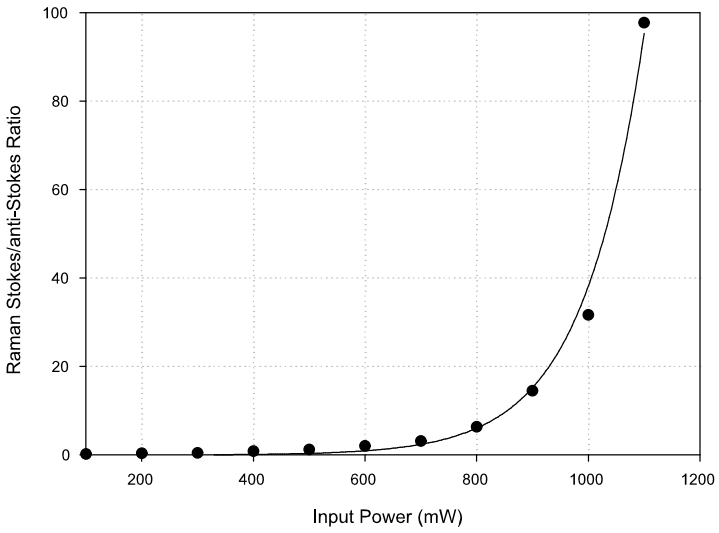

Figure 5.18: *Ratio of Raman Stokes and anti-Stokes versus input power in MCF.*

When the Raman Stokes signal rises rapidly with increasing input powers this indicates the onset of stimulated Raman scattering. The ratio of Raman Stokes and anti-Stokes versus input power indicates that the onset of stimulated Raman scattering occurs at around 900mW, which is in close agreement with the calculated value.

5.4.4 Discussion

It was evident from the experimental investigation that MI is a major limiting factor for sensing range and performance in systems that use standard SMF at 1550nm. However, the MI effect may be avoided by simply using sensing fibres that have negative dispersion at 1550nm, e.g. MCF. In this fibre, the input power can be significantly higher, which means longer range and better sensing performance. This obtained results have proven the benefit of exploring fibres originally designed to handle nonlinear/dispersion effects for the telecommunications industry; hence the DOFS may benefit.

5.5 Conclusions

An investigation was conducted to evaluate nonlinear effects on spontaneous Brillouin-based distributed sensors. Prior to this study, the nonlinear effects present in this type of sensors, namely spatial drift in temperature along the fibre, were initially attributed to exceeding the stimulated Raman scattering threshold. However, due to the absence of any observed Raman signal at the end of the sensing fibre, it was subsequently thought that SPM might be responsible. These new results now show that MI is responsible for the drift. Using MCF avoids MI and allows pulse powers to increase from around 100mW up to ∼900mW for sensing lengths of 25km. It is concluded that using NZ-DSF with negative dispersion at 1550nm as a sensing medium may provide a longer sensing range and better performance. On the other hand, in standard SMF, where the launched probe power needs to be limited to avoid nonlinear effects, a substantial improvement in sensing range and performance can still be achieved, provided that the double pass fibre loss, weakness of Brillouin scattering and limited input power can be compensated. One proposed solution is to use distributed optical amplification. The next chapter is devoted to techniques for improving the Brillouin coherent sensor range and sensing performance, utilising optical Raman amplification.

Bibliography

[1] R. G. Smith, "Optical Power Handling Capacity of Low Loss Optical Fibers as Determined by Stimulated Raman and Brillouin Scattering," *Applied Optics*, vol. 11, no. 11, p. 2489, November 1972.

[2] G. P. Agrawal, *Nonlinear Fiber Optics*, 2nd ed. Academic Press, 1995.

[3] Y. Namihira, "Wavelength Dependence of Correction Factor on Effective Area and Mode Field Diameter for Various Singlemode Optical Fibres," *Electronics Letters*, vol. 33, no. 17, p. 1483, August 1997.

[4] R. G. Stolen and A. M. Johnson, "The Effect of Pulse Walk-off on Stimulated Raman-Scattering in Fibers," *IEEE Journal of Quantum Electronics*, vol. 22, no. 11, p. 2154, November 1986.

[5] A. Boskovic, S. V. Chernikov, J. R. Taylor, L. Gruner-Nielsen and O. A. Levring, "Direct Continuous-Wave Measurement of n_2 in Various Types of Telecommunication Fiber at $1.55\,\mu$m," *Optics Letters*, vol. 21, no. 24, p. 1966, December 1996.

[6] H. Izumita, Y. Koyamada, S. Furukawa and I. Sankawa, "The Performace Limit of Coherent OTDR Enhanced with Optical Fiber Amplifiers due to Optical Nonlinear Phenomena," *Journal of Lightwave Technology*, vol. 12, no. 7, p. 1230, July 1994.

[7] S. M. Maughan, "Distributed Fibre Sensing using Microwave Heterodyne Detection of Spontaneous Brillouin Backscatter," PhD Thesis, University of Southampton, 2001.

[8] M. Karlsson, "Modulational Instability in Lossy Optical Fibers," *J. Opt. Soc. Am. B*, vol. 12, no. 11, p. 2071, November 1995.

[9] A. Hasegawa and K. Tai, "Effects of Modulational Instability on Coherent Transmission Systems," *Optics Letters*, vol. 14, no. 10, p. 512, May 1989.

[10] P. C. Wait, K. De. Souza, T. P. Newson, "A Theoretical Comparison of Spontaneous Raman and Brillouin Based Fibre Optic Distributed Temperature Sensors," *Optics Communications*, vol. 144, no. 1-3, p. 17, December 1997.

Chapter 6

Long Range Distributed Temperature/Strain Sensors Utilising Raman Amplification

6.1 Introduction

As demonstrated in the previous chapters, the fibre double pass loss, weakness of Brillouin scattering and nonlinear effects limit the performance of long range BOTDR based sensors. Recently, much attention has focused on the use of Raman amplifiers for optical fibre communication systems. The most attractive feature of these amplifiers is their large gain over a very wide bandwidth (multi-THz), combined with a small noise figure (∼3dB). This chapter investigates the combination of Raman amplification with CBS to enhance sensing range and performance. A review of the optical Raman amplification principle followed by the results of distributed temperature/strain measurements using different Raman pump configurations are reported. The various configurations are compared and their relative advantages are highlighted and discussed.

6.2 Optical Amplifiers

EDFAs have been tremendously successful in the low-loss window (∼1550nm) with broad gain bandwidth over 80nm, high gain, low insertion loss and polarisation independent gain [1]. However, these amplifiers are mainly used as discrete amplifiers[1], i.e. as in-line amplifiers and/or preamplifiers in communication systems. Whilst fibre Brillouin amplifiers can be used for distributed amplification using standard SMF, they have a narrow gain bandwidth (∼35MHz) and a high noise figure (∼20dB) [2], and this effectively removes such amplifiers from further consideration. Raman amplifiers have been developed and, along with the recent progress in high-power fibre lasers, now offer an efficient means of distributed optical amplification. The advantage of these amplifiers for distributed optical sensors is that any optical fibre can serve as the amplifying medium; in essence, the sensing fibre itself becomes the amplifier medium and hence the gain is distributed over the length of the fibre. In general, launching high-power pump light into the sensing fibre and allowing it to co-propagate or counter-propagate relative to the probe signal triggers distributed Raman amplification. Raman amplifiers were first demonstrated to extend OTDR sensing range by Spirit [3] and recently for BOTDR, based on direct detection, by [4]. Both have demonstrated potential improvements in sensing range and accuracy.

6.2.1 The Raman Amplification Principle

Raman scattering may by used to amplify an optical signal if the signal propagates simultaneously with a high-power pump beam and the signal falls within the Raman gain spectrum for that pump frequency. In fact, by sending an intense pulse of light down the fibre from a laser source, Raman Stokes wavelengths are generated, co-propagating with the forward travelling pulse, with the maximum intensity occurring at a wavelength shift of ∼100nm [5]. These Raman wavelengths build up by a process of stimulated Raman generation until the pump pulse is depleted. The generated first order Raman wavelength can also go on to generate further multiple orders of Raman wavelengths, each separated by ∼100nm.

[1] The gain occurs over a short length of fibre.

Raman gain can be derived analytically from the coupled power equations 6.1 and 6.2, on the assumption that pump depletion due to Raman interaction and higher order Stokes generation may be neglected. The coupled power equations below are provided by [6]:

$$\frac{dP_s}{dz} = \frac{g_r}{A_{eff}} P_s P_p - \alpha_s P_s \tag{6.1}$$

$$\frac{dP_p}{dz} = \frac{-\lambda_s g_r}{\lambda_p A_{eff}} P_s P_p - \alpha_p P_p \tag{6.2}$$

Where, P, α and λ are the optical power, fibre loss, and optical wavelength, respectively. Subscripts p and s refer to the pump and Stokes, respectively. A_{eff} is the effective core area and g_r is the Raman gain coefficient. The second terms on the right hand side of equations 6.1 and 6.2 are due to linear absorption in the fibre medium; the other terms describe Raman-type nonlinear coupling, e.g. the growth of the signal and pump depletion. The distribution of all possible Stokes frequencies that may be produced via Raman scattering is known as the Raman gain spectrum. The Raman gain spectrum depends on both the frequency of the incident light and the nature of the host material. Raman small signal gain can be approximated analytically from the coupled power equations 6.1 and 6.2 on the assumption that the $P_p \gg P_s$ and the pump depletion due to Raman interaction and higher order Stokes generation may be neglected; Raman gain in the forward pumping may be given by:

$$G_r(L) = \exp(\frac{g_r P_p L_{eff}}{K A_{eff}}) \tag{6.3}$$

Where K is a polarisation factor, L_{eff} is the effective length given by equation 5.3, $A_{eff} \cong 80\mu\mathrm{m}^2$, $g_r \cong 7.34 \times 10^{-14}$ m/W given by equation 5.2 for λ_p=1450nm, and $\alpha_p \cong 0.27$dB/km. Using equation 6.3 with such parameter values, the integrated Raman gain along a length of fibre L is plotted (Figure 6.1) at different pump powers.

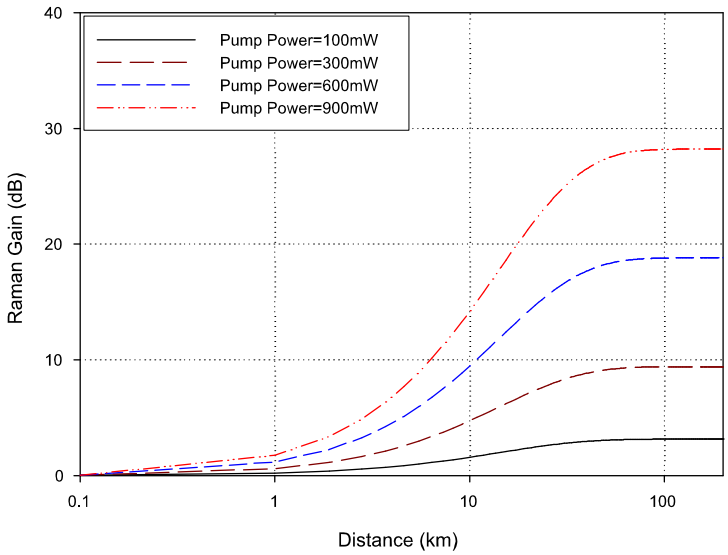

Figure 6.1: *Theoretical integrated Raman gain profile along the fibre. The gain was modelled for various pump powers from 100mW to 900mW.*

It can be seen from Figure 6.1 that Raman gain becomes larger as the fibre length increases and, at around 50km, it asymptotically reaches a constant value due to the attenuation of the pump power. From figure 6.1, the Raman gain can be approximated to ∼28dB at ∼100km for a pump power of ∼900mW, where a linear dependance on the pump power is exhibited (∼3.1dB/100mW). It is evident from equation 6.3 that Raman gain is influenced by a number of parameters, such as pump power, fibre loss, fibre effective area and gain coefficient. However, pump power and Raman gain coefficient are considered to be the most important parameters. The latter governs the coupling between the pump and signal and its value depends greatly on the pump wavelength (Equation 5.2). For optimum Raman gain, the pump and signal wavelengths need to be selected carefully, since the gain coefficient and effective length are governed by pump wavelengths. In fact, operating with pump and signal at ∼1450nm and ∼1550nm wavelength respectively, may provide the best performance [7].

Distributed Raman amplification may be achieved for BOTDR based sensors by using different Raman pump configurations, i.e. CW co-propagation, counter-propagation and delayed pulse Raman pump configurations. These Raman pump configurations were investigated experimentally for long range distributed temperature/strain measurements using the previously described CBS. The results are presented in the following sections.

6.3 Temperature Sensor with CW Co-propagating Raman Amplification

The single-ended distributed optical sensor is attractive because of the need only to access one end of the sensing fibre. In this section, the single-ended CW co-propagation Raman amplification technique is investigated. Initially, the optimum combination of the probe and pump power was determined and subsequently this was used for a temperature measurement along 100km of standard SMF, assuming zero strain.

6.3.1 Introduction

Raman amplification was initially demonstrated in Rayleigh based OTDR measurements by Spirit [3], where a Raman gain of 8dB, translated to a similar increase in measurement range, was obtained. For BOTDR based measurement, Raman amplification was recently investigated by direct detection of spontaneous Brillouin scattering [4]. It was found that the probe input power had to be significantly reduced, to avoid spectral broadening of the probe pulse caused by nonlinear effects such as MI (Chapter 5), another limiting factor was the Raman ASE Stokes noise generated from the CW Raman pump, which saturates the detection system at higher pump powers, these factors limited the potential increase in sensing range. An alternative solution was to combine the optimised CBS, which has a good filtering system with the advantages of the co-propagating Raman pump technique, which led to a significant improvement in sensing range and performance.

6.3.2 Experimental Details and Initial Measurements

The experimental arrangement for coherent detection of anti-Stokes spontaneous Brillouin backscatter with Raman amplification is illustrated in Figure 6.2.

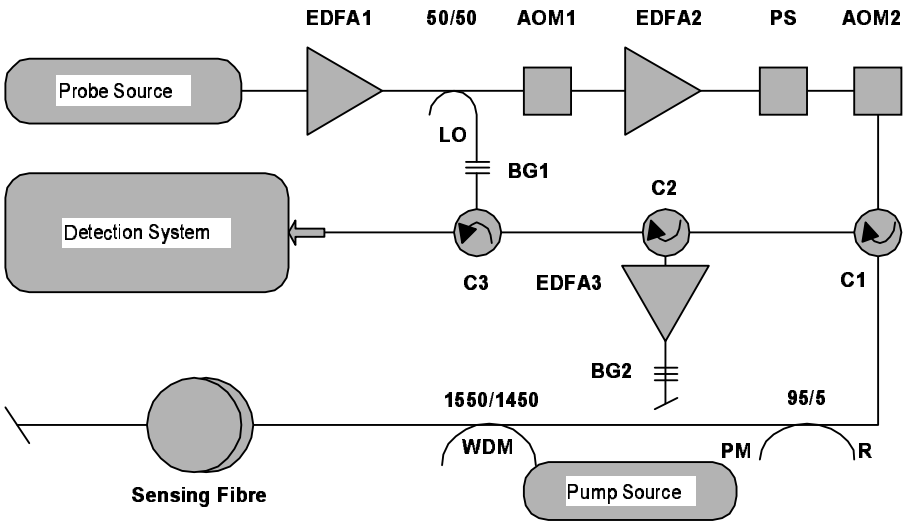

Figure 6.2: *Experimental set-up of the coherent Brillouin sensor utilising Raman amplification.*

The source was a tuneable laser at 1533.2nm, with ∼1MHz linewidth. Two cascaded EDFAs generated a peak probe power of ∼80mW, with a pulse width of 200ns and a repetition rate of 80Hz, which was launched into the 106km sensing fibre. A third EDFA was used to amplify the weak backscattered signal prior to mixing it with optical LO. The fibre Bragg grating BG1 was used to filter the anti-Stokes from the Rayleigh and spontaneous Raman scattering and allow the optical LO to mix with the anti-Stokes signal. A 20GHz optical detector and the MDS (described in Section 3.4) allow the collection of time domain traces centred at the desired RF frequencies. The Raman pump signal at 1450nm with ∼1.5nm linewidth was coupled to the pulsed probe signal using (1450/1550nm) WDM where up to ∼1000mW of CW output pump power was obtained. The total length of the sensing fibre was made up of 9 sections of standard SMF, fusion spliced together. The first seven sections: 11km, 19km, 17.2km, 19km, 22.3km, 11km and 4.7km remained on their original spools at room temperature and zero strain. Two additional fibre sections of 0.5km and 1.3km at 47.2km and 100km respectively, were placed in an oven at 80 °C with zero strain. The temperature change along the sensing fibre was determined by analysing the frequency shift of the anti-Stokes

Brillouin backscatter signal. Brillouin spectra were built from 18 separate backscatter traces, each averaged 2^{15} times, and taken every 10MHz, starting at 10.95GHz. A Lorentzian curve was fitted to each spectrum and the peak frequency and corresponding power were evaluated at each point along the sensing fibre. Using the current set-up, the probe and Raman gain spectrum were measured at the end of 106km, at different pump powers, using an OSA. The probe power was ∼80mW and it had a 500ns pulse width. The results are shown in Figure 6.3.

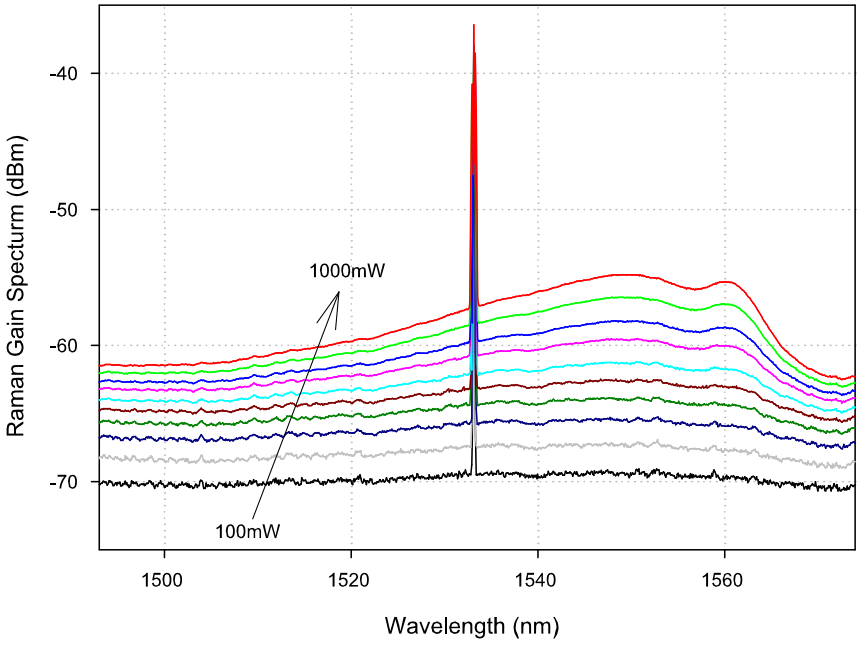

Figure 6.3: *Measured Raman gain profile at different pump powers. The pump power was varied from 100mW to 1000mW, in steps of 100mW*

The above figure shows the Raman gain spectra from ∼1500nm to ∼1580nm, which increases with pump power. The gain peaks around 1550nm and is significantly reduced for wavelengths greater than ∼1560nm. It would be useful to have the probe signal in the optimum Raman gain region (∼1550nm). However, the optical set-up had been constructed for a pulse wavelength of 1533.2nm corresponding to the peak of the EDFA gain.

In order to estimate nonlinear effects, such as MI on the probe signal, with the presence of Raman gain, the probe optical spectrum was measured at the end of 106km and at different Raman pump powers using an OSA whilst maintaining the input probe pulse power of ∼80mW and pulse width of 500ns. The result is shown in Figure 6.4.

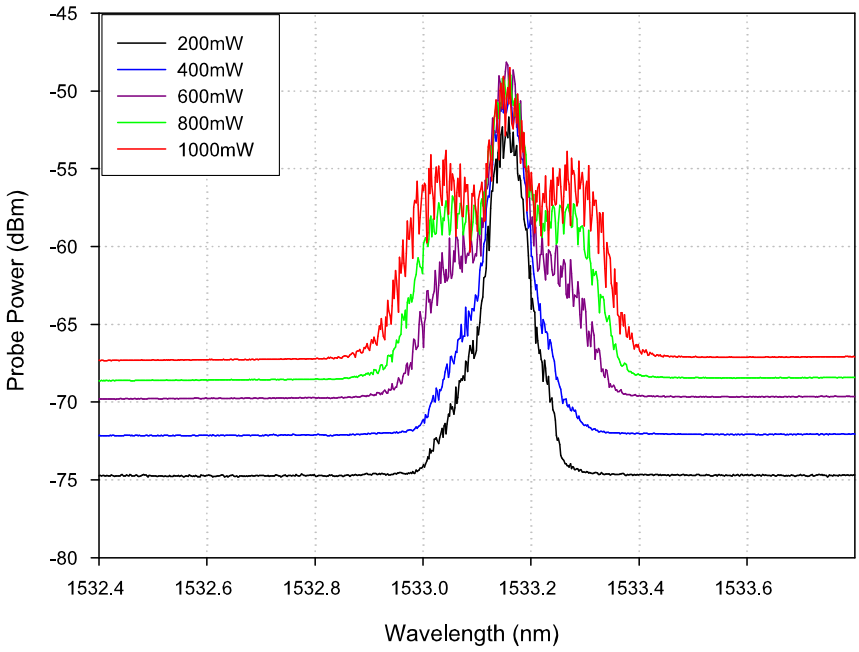

Figure 6.4: *Probe spectrum versus pump power at the end of 106km with input pulse power of ∼80mW and pulse width of 500ns. The pump power was varied from 200mW to 1000mW, in steps of 200mW.*

As the Raman pump power increases the probe spectrum is broadened, due to the MI. In order to avoid such broadening, but still make use of the Raman gain, it was necessary to find the optimum combination of probe and pump powers to give the best sensing performance. In order to achieve this, the temperature resolution was measured using both Brillouin frequency and power at a range of 100km, with different combinations of probe and pump powers. The range of probe powers was from 5 to 160mW and that of the Raman pump was from 0 to 1000mW, in steps of 200mW. The probe pulse width was 500ns.

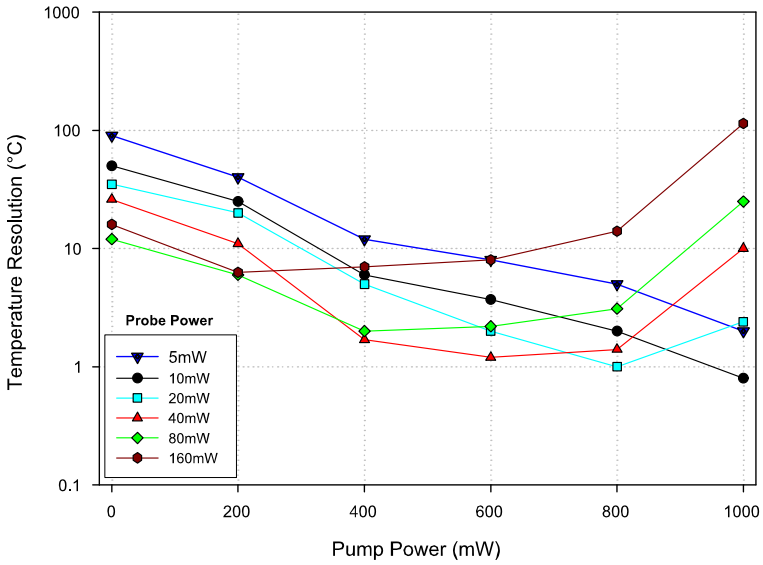

(a) *Performance analysis based on Brillouin frequency measurement.*

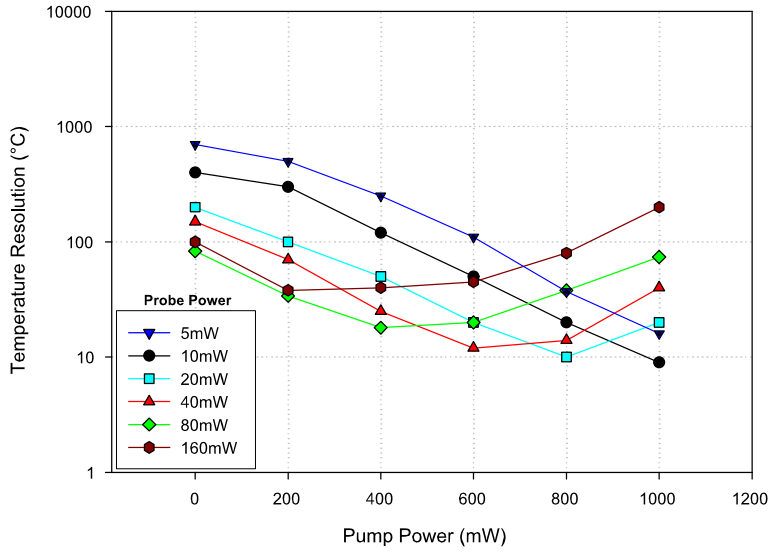

(b) *Performance analysis based on Brillouin power measurement.*

Figure 6.5: *Performance analysis of the optimum combination of probe and pump power using a CW co-propagation Raman pump configuration for both Brillouin frequency and power based measurements.*

Figure 6.5(a) shows the variation in the temperature resolution as the pump power is increased for various input probe powers. At zero pump power, it can be seen that the resolution initially improves as the probe power is increased to ∼80mW, but then falls when it is increased beyond this to 160mW. This is again due to the onset of MI. At the two lowest probe powers, 5 and 10mW, the resolution continues to improve as the

pump power is increased to 1000mW. For a 10mW probe power and 1000mW pump, the temperature resolution was below 1 °C. For probe powers greater than 10mW, a minimum is observed at a certain pump power. As the pump power increases, the minimum occurs at a lower probe power and the resolution improves. At 1000mW pump power the best resolution was found using a 10mW probe pulse. The traces suggest that the probe power could be increased a little, for a slightly improved resolution, but should be kept below 20mW, as, above this, the resolution would worsen. Without a Raman pump, it was found that ∼80mW probe power gives the best result, and this is considered as the MI threshold for such a sensing range. Using the Brillouin power based measurements (Figure 6.5(b)), a similar conclusion can be derived. In order to simplify the analysis of figure 6.5, the best result obtained with each combination is plotted in Figure 6.6 for both measurements.

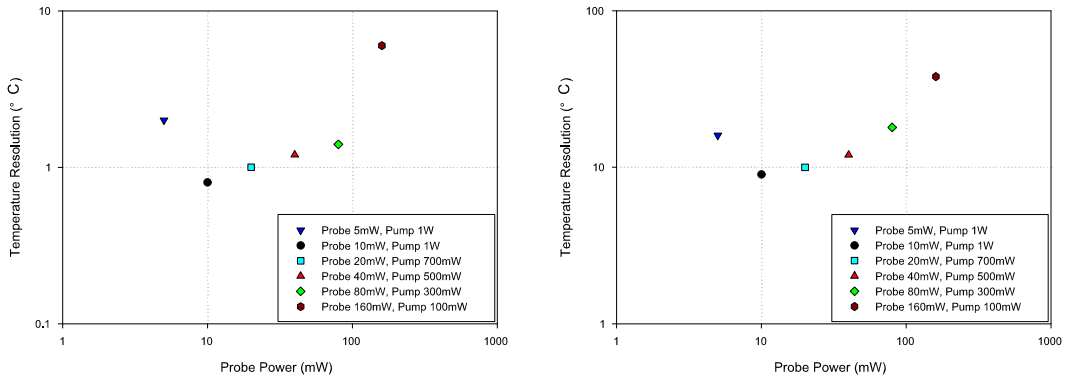

(a) *Frequency based measurement.* (b) *Power based measurement.*

Figure 6.6: *Optimum combination of probe and pump power based on both Brillouin frequency and power measurements. The 10mW and 1000mW probe and pump power combination is clearly shown to have the lowest temperature error in both measurements.*

Figure 6.6 illustrates the optimum probe and pump power combination for the available maximum pump power of ∼1000mW. However, it is expected that the temperature resolution could improve further provided that a higher pump power is available, combined with an even lower level of probe power.

The forward Raman gain was approximated by measuring the probe optical spectrum at the end of the sensing fibre using an input probe pulse of 10mW and comparing the output amplified pulse to that of the unamplified pulse at the far end of the sensing fibre, as the Raman pump was increased from 0 to 1000mW, in steps of 100mW. Results are shown in Figure 6.7.

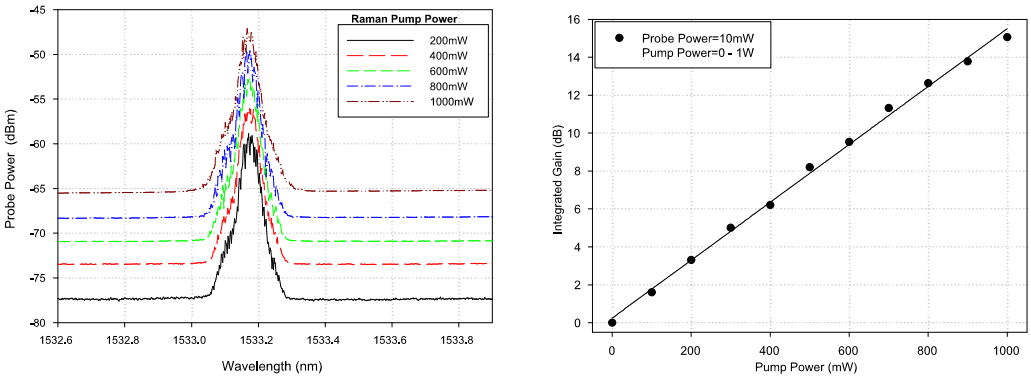

(a) *Amplified probe spectrum at different pump powers.*

(b) *Single Raman gain in CW co-propagating Raman pump.*

Figure 6.7: *Single Raman gain for CW co-propagating Raman pump measured at the end of the sensing fibre.*

Figure 6.7(a) shows the Raman gain as a function of Raman pump power and indicates a linear increase in gain as the pump power is increased. The overall single pass gain is shown in Figure 6.7(b) and was found to be ∼15dB (∼30dB for double pass).

In order to evaluate the advantages of using Raman amplification in a co-propagation Raman pump configuration, the temperature change along the sensing fibre was measured using Brillouin frequency shift with/without Raman amplification at the optimum probe and pump power combination with a pulse width of 200ns. The RMS frequency errors were evaluated along the entire sensing length and converted to the corresponding temperature resolution.

6.3.3 Experimental Results

A plot of the peak frequency as a function of distance is shown in Figure 6.8(a) at a probe power of 80mW over the 103km sensing fibre without Raman amplification. The sharp spikes at 47 and 100km correspond to the 0.5 and 1.3km heated sections, at 80 °C.

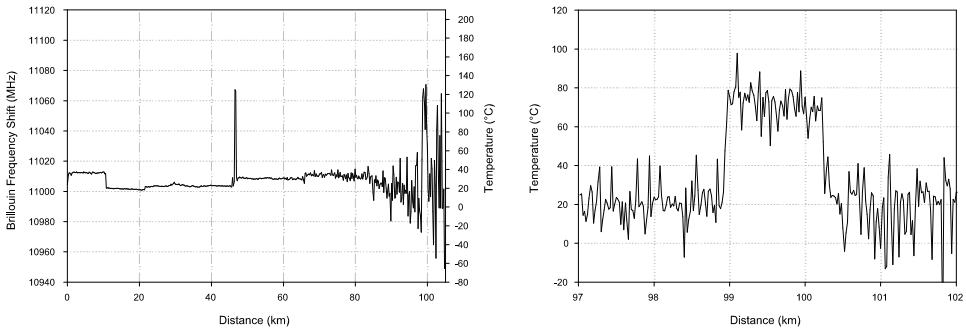

(a) *Brillouin frequency shift (left) and temperature (right) along the sensing fibre.*

(b) *An enlargement of the 1.3km heated section at 100km.*

Figure 6.8: *Temperature measurements obtained without Raman amplification for comparison purposes.*

The different fibre sections exhibit different Brillouin frequency shifts at room temperature, either due to differences in fibre properties or fibre winding tensions. Figure 6.8(b) is an enlargement of the heated section (1.3km at 100km in length). The frequency shift was referenced to room temperature and zero strain and then converted to the corresponding temperature. The temperature resolution of the 1.3km heated section at 100km, based on the frequency measurement, was found to be ∼12 °C. The temperature resolution based on the Brillouin power measurement was found to be ∼100 °C. Using the optimum probe and pump power, the previous measurement was repeated with a CW co-propagating Raman pump configuration. For clarity, figure 6.9 shows three dimensional representation of the Brillouin frequency spectrum around the 1.3km heated section, 100km down the sensing fibre.

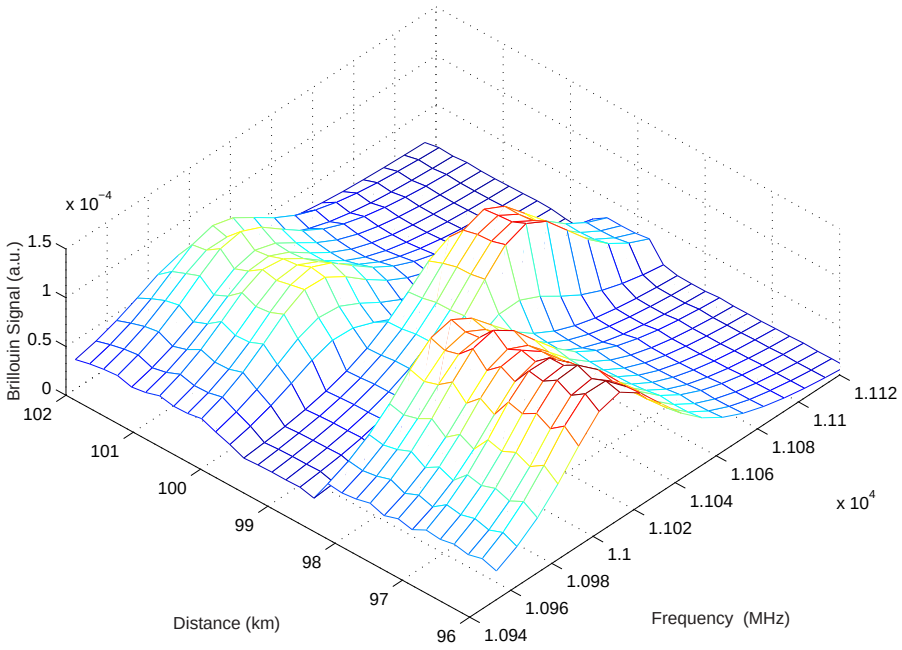

Figure 6.9: *Three dimensional representation of the Brillouin spectrum around the 1.3km heated section, 100km down the sensing fibre, with the presence of Raman amplification.*

Figure 6.10(a) shows the Brillouin frequency shift along the sensing fibre. Figure 6.10(b) is an enlargement of the 1.3km heated section, at 100km, for an oven temperature of 80 °C. A temperature sensitivity of ∼1.1 MHz/ °C was measured, and this is in close agreement with previous measurements.

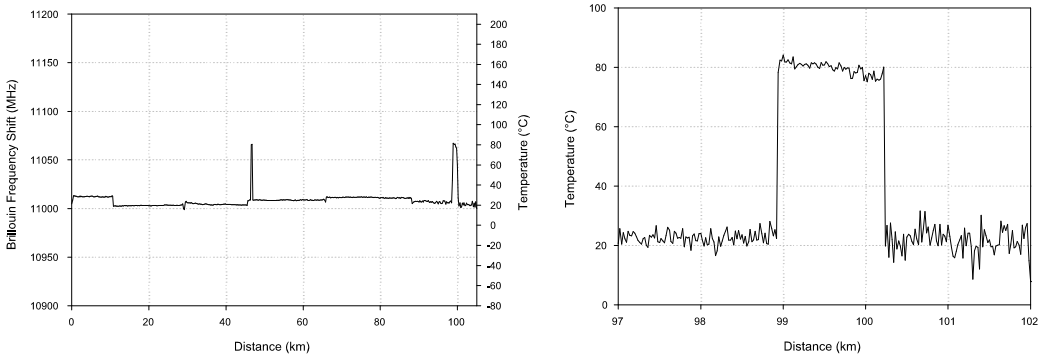

(a) *Brillouin frequency shift (left) and temperature (right) along the entire sensing length.*

(b) *An enlargement of the 1.3km heated section, at 100km.*

Figure 6.10: *Temperature measurements with co-propagating Raman pump configuration at the optimum probe and pump power combination.*

The RMS Brillouin frequency and power errors along the sensing fibre were evaluated with/without Raman amplification every 20km, averaged over a range of 5km, and were

converted to the corresponding temperature errors. The results are shown in Figure 6.11.

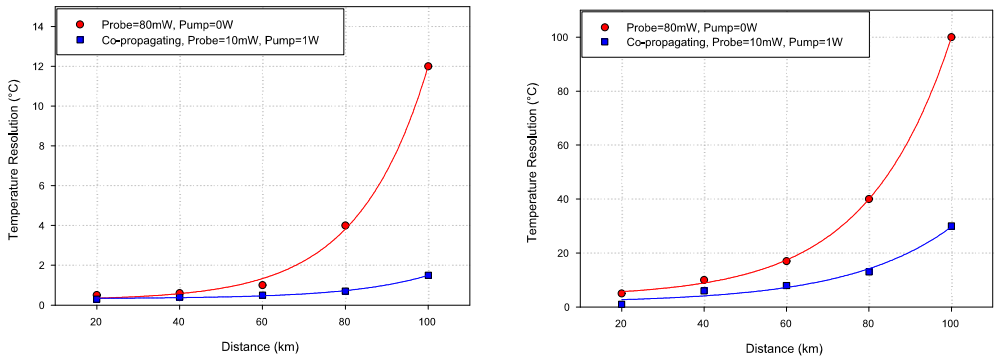

(a) *RMS temperature resolution based on Brillouin frequency measurement.* (b) *RMS temperature resolution based on Brillouin power measurement.*

Figure 6.11: *Temperature resolution along the sensing fibre with/without co-propagating Raman pump configuration.*

Figure 6.11(a) shows the RMS temperature resolution along the fibre based on Brillouin frequency measurements. The sensor was able to record a temperature resolution of less than 0.5 °C, up to ∼80km, with Raman gain amplification. The error was less than 2 °C at 100km compared to 12 °C obtained without Raman amplification. For the power based measurements (Figure 6.11(b)), temperature resolution was improved with the presence of Raman gain from ∼100 to ∼30 °C. The spatial resolution of the measurement was 20m corresponding, to a pulse width of 200ns used in the experiment.

6.3.4 Discussion

The overall improvement of the temperature resolution at a 100km sensing range, due to the use of a co-propagating Raman pump configuration, was found to be around 8.5dB and 5dB using Brillouin frequency and power based measurements, respectively. Sensor performance is expected to improve further using a higher pump power with further reduced probe power. The Raman ASE, observed with the direct detection of Brillouin signal, was not observed with the CBS, due to its good optical filtering system. To further investigate the advantages of using Raman amplification with the coherent detection of Brillouin signal, a counter-propagating Raman pump configuration was investigated and is reported next.

6.4 Temperature Sensor with CW Counter-propagating Raman Amplification

6.4.1 Introduction

Although Raman amplification with a co-propagating pump, described in the previous section, can be used to improve the performance of the sensor, the improvement does not match the Raman gain as the pulse power has to be reduced to avoid MI. In the counter-propagation configuration, this is not the case for long sensors, as the probe pulse is significantly attenuated before experiencing Raman amplification. In this section, experiments were conducted to investigate this configuration for distributed temperature measurement up to 150km, based on the Brillouin frequency shift.

6.4.2 Experimental Details and Measurements

The Raman pump signal was launched at the end of the sensing fibre, in counter propagation mode relative to the probe signal, using the same experimental set-up previously described and shown in Figure 6.2. A preliminary investigation of the MI effect, with the presence of counter-propagating Raman pump, reveals that the pump power could be increased to its maximum available power of 1000mW before any spectral broadening of the probe pulse was observed. Even when using a probe pulse power of ∼80mW, the Raman pump does not lower the nonlinear threshold of the incident probe power. Measurements were therefore taken at these powers. Using a probe power of 80mW, Raman gain along the sensing fibre was measured at pump powers of 300mW, 600mW and 1000mW. The previous measurement of distributed temperature along 100km was repeated with the optimum probe and pump power combination and a pulse width of 200ns. The RMS frequency errors along the same 100km were evaluated with and without Raman amplification for a spatial resolution of 20m. The sensing fibre length was extended in two steps by adding additional fibres to the front end, first of 25km then 50km: i.e. the original 0.5km and 1.3km heated sections at 47.2km and 100km sensing length were shifted forward by 25 and 50km from the front end of the sensing fibre,

respectively. The temperature measurement was then repeated for each length using an increased pulse width of 500ns.

6.4.3 Experimental Results

The optimum probe and pump power combination was found to be ∼80mW and ∼1000mW, respectively. Using such powers, integrated Raman gain was re-evaluated with this pump configuration. Figure 6.12(a) shows the amplified Brillouin signals along the 100km at different pump powers, and figure 6.12(b) shows the corresponding Raman gain profile along the sensing fibre for a probe power of ∼80mW.

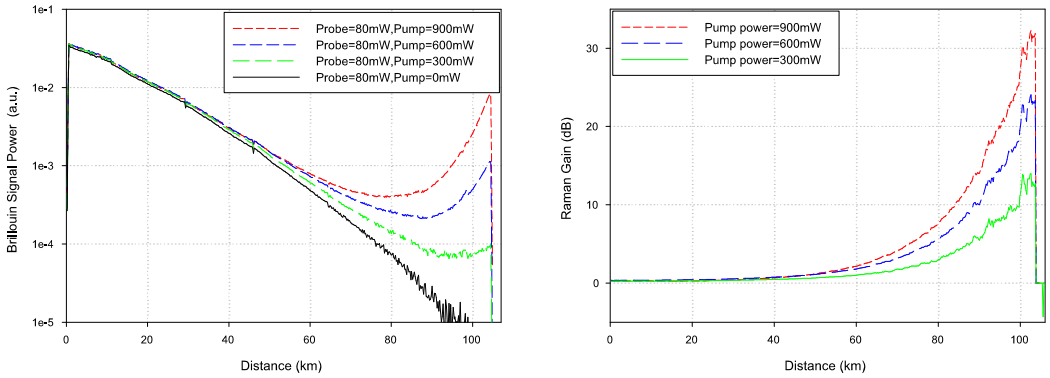

(a) *Amplified Brillouin signal at different counter-propagating pump powers.*

(b) *Raman gain profile along the sensing fibre at different pump powers.*

Figure 6.12: *Raman gain profile using CW counter-propagating Raman pump configuration. The gain was obtained by taking the ratio of an amplified signal to a reference signal measured without the pump.*

According to the measured gain, in Figure 6.12(b), the double path integrated gain for a pump power of 1000mW at the end of the sensing fibre was approximated to around 30dB (i.e. ∼3.0dB for every 100mW pump power). This measured gain is in good agreement with the single pass gain obtained using the co-propagation pump configuration (Figure 6.7). Figure 6.13 illustrates a three dimensional representation of the Brillouin spectrum along the sensing fibre measured at the optimum probe and pump power of ∼80mW and 1000mW, respectively.

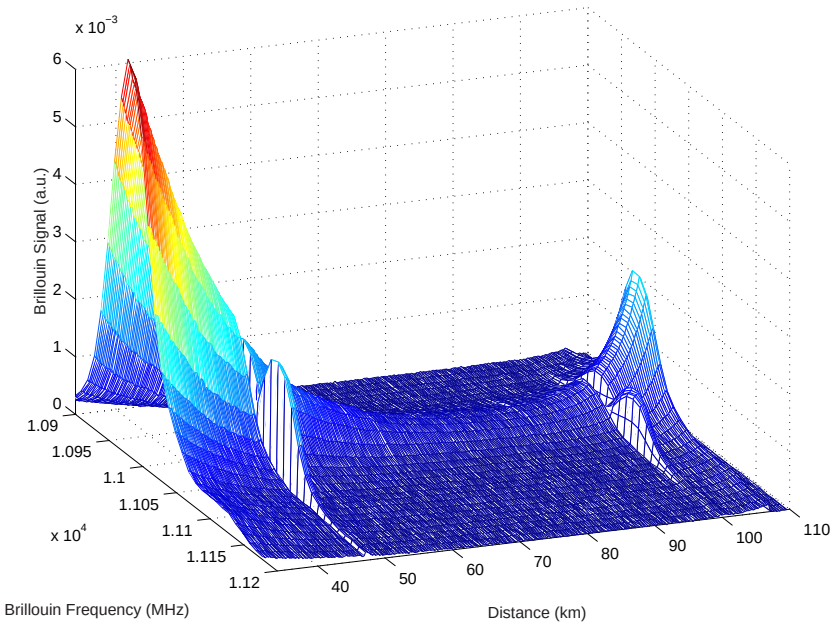

Figure 6.13: *Three dimensional representation of the Brillouin spectrum along the sensing fibre with counter-propagating Raman pump configuration. The Raman gain effect is clearly visible at the end of the fibre*

The counter-propagation Raman gain effect is clearly visible at the end of the sensing fibre along with the two heated sections at 47.2 and 100km, respectively. The Brillouin frequency shift and the corresponding temperature profile along the sensing fibre are illustrated in Figure 6.14. Both heated sections are clearly visible.

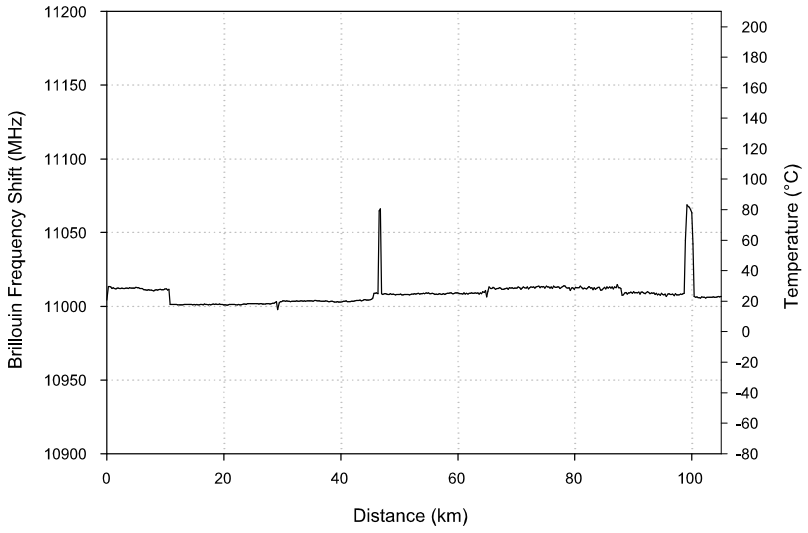

Figure 6.14: *Brillouin frequency shift (left) and the corresponding temperature (right) along the sensing fibre measured using a counter-propagating Raman pump configuration.*

Based on the Brillouin frequency shift measurement, the temperature resolution was found to be better than 1 °C at the heated section, 100km down the sensing fibre, using this pump configuration. Taking advantage of the accuracy of Brillouin frequency based measurements and to explore a longer sensing range, the sensing fibre was extended to 125km and the temperature was measured using the Brillouin frequency. After the addition of the first 25km at the front end of the sensing fibre, the heated sections were at 72km and 125km, respectively. The Brillouin frequency shift was measured using a probe power of ∼80mW , an increased pulse width of 500ns and a pump power of 1000mW. Figure 6.15 illustrates the temperature profile and the temperature resolution along 125km of sensing fibre.

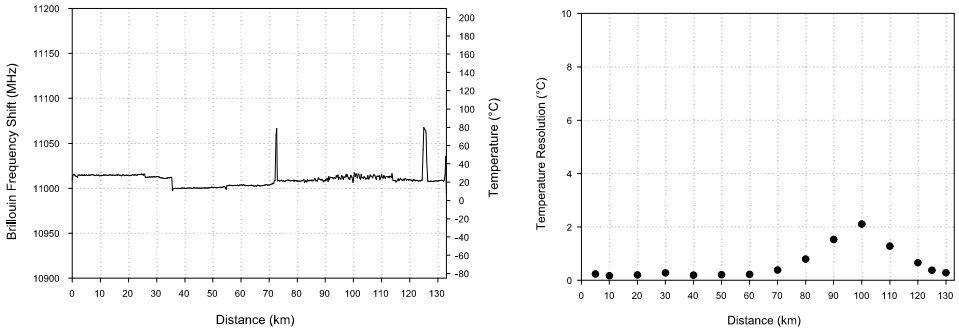

(a) *Brillouin frequency shift (left) and the corresponding temperature change (right) along 125km sensing fibre.*

(b) *Temperature resolution along 125km of sensing fibre measured every 10km over a range of 2km.*

Figure 6.15: *Temperature measurements along 125km using a counter-propagating Raman pump configuration.*

Figure 6.15(b) shows the temperature resolution along the 125km sensing fibre measured every 10km over a range of 2km. The temperature resolution was better than 1 °C up to ∼85km, then it increased to around 2 °C at 100km; at 125km the temperature resolution was better than 1 °C. Encouraged by such a result, the sensing fibre was extended by another 25km. The heated sections were then at 97.2 and 150km down the sensing fibre respectively, and the previous measurement was repeated. Figure 6.16 shows Brillouin frequency shift/temperature profile and the associated temperature error along 150km of the sensing fibre.

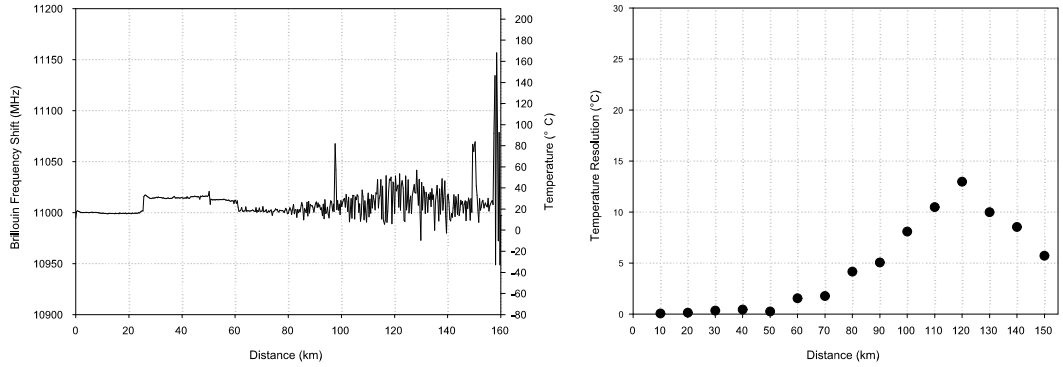

(a) *Brillouin frequency shift (left) and the corresponding temperature change (right) along 150km sensing fibre.*

(b) *Temperature resolution along a 150km sensing fibre measured every 10km over a range of 2km.*

Figure 6.16: *Temperature measurements along 150km using counter-propagation Raman pump configuration.*

The error in temperature increases with distance, when the probe signal becomes weaker due to fibre loss. The worst temperature resolution occurred around 120km and then it improved towards the end of the sensing fibre, where the pump signal was strong. A $\sim$5 °C temperature resolution was achieved at 150km. This temperature resolution also occurs at $\sim$80km, hence a greater than 70km improvement, which equates to around 30dB gain as measured earlier (Figure 6.12).

6.4.4 Discussion

Using a counter-propagation Raman pump configuration proved to increase significantly the sensing range. However, the need to access both ends of the fibre is a potential limitation. In order to further explore the use of Raman amplification with the CBS, a pulsed Raman pump configuration was explored, as reported in the next section.

6.5 Temperature Sensor with Pulsed Raman Amplification

An alternative approach to avoid MI in the presence of Raman gain is to use the so called delayed pulsed Raman amplification technique, first demonstrated at Southampton University with direct detection of the Brillouin signal. This section explains its application to the coherent detection system.

6.5.1 Introduction

The principle of the pulsed Raman amplification technique is to co-propagate a pulsed Raman pump with the probe pulse, such that it undergoes Raman amplification some distance down the sensing fibre, resulting in an increase of the local backscattered Brillouin signal and hence the range. In this technique, the probe pulse at 1533.2nm will be launched first, followed by the Raman pump pulse at 1450nm. The fibre dispersion allows the pump pulse (shorter wavelength) to travel faster than the probe pulse down the sensing fibre, provided that both pulses' wavelengths are in the anomalous dispersion regime. The two pulses overlap at a certain distance down the sensing fibre, determined by the initial delay. The gain experienced by the probe pulse is determined by the pump power and the walk off length (Equation 5.4), which is governed by the length of both pulses. The amplification of the probe pulse allows greater pulse energy to be achieved some distance down the sensing fibre. Eventually the faster exhausted pump pulse will be depleted, leaving the boosted probe pulse capable of propagating over a longer distance. Although the probe pulse width is limited by the required sensing spatial resolution, the pump pulse width may be considerably larger, hence a large amount of energy can be transferred to the probe pulse. In fact, by adjusting both pulses' powers and delay, the probe pulse may be amplified to the highest possible power, i.e. up to its threshold limit some distance from the fibre front end, so that it provides longer sensing range and better sensing performance. This technique was first demonstrated for the Rayleigh based OTDR [8] and then for direct detection of the Brillouin based sensor, the available pump power was the limiting factor [9].

6.5.2 Experimental Details and Measurements

In this experiment, the previous experimental set-up shown in Figure 6.2 was used. The CW Raman signal at 1450nm was pulsed using an AOM before being coupled to the probe signal, with an initial delay of about 50ns, which corresponds to an overlap position of the two pulses at around 50km down the sensing fibre. The maximum pulsed pump power, after AOM insertion loss (∼9dB), was about 120mW. To allow the backscattered light generated from all the sensing fibre to experience CW Raman gain during its journey to the detector, the pump pulse width can be adjusted to around double the fibre length[2]. With an available pump pulse power of 120mW and probe power of 80mW and 200ns pulse width, the pulsed Raman gain was obtained by measuring the Brillouin signal with/without the Raman pump, and for comparison purposes, the previous temperature resolution measurement along 100km was repeated with a 200ns pulse width. The probe and pump powers were ∼80mW and 120mW, respectively.

6.5.3 Experimental Results

For clarity, figure 6.17 illustrates the Raman gain induced on the probe pulse (200ns) as a result of overlapping with the reduced pump pulse (200ns) measured at the front end the sensing fibre.

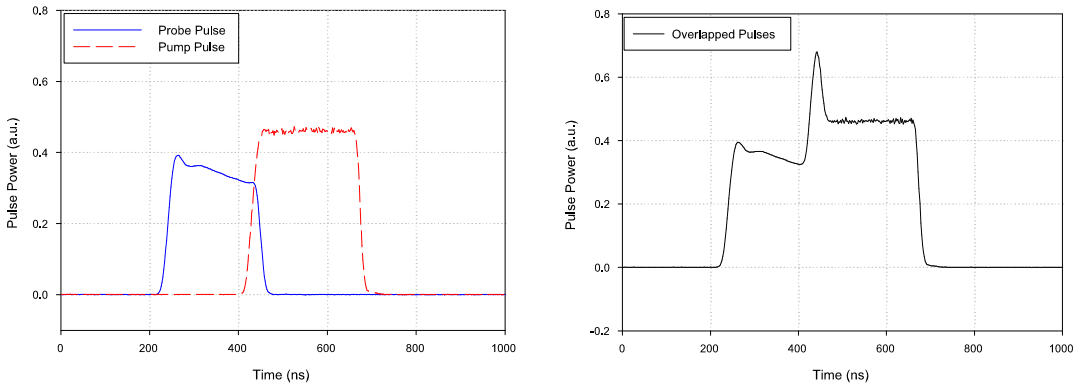

(a) *Probe and pump pulses measured separately.* (b) *Overlapped probe and pump pulses.*

Figure 6.17: *The probe and pump pulses overlapping effect measured in two conditions.*

[2]In a 100km sensing length, a Brillouin backscattered signal needs 1ms to arrive at the detector.

The probe pulse must lead with a suitable delay, according to the required overlap position down the sensing fibre. Figure 6.17(a) shows the two pulses at the front end of the sensing fibre measured separately with the probe pulse leading the pump pulse in time. Figure 6.17(b) shows the two pulses measured simultaneously when the pump pulse was allowed to overlap with the probe pulse. This initial overlap led to an increase in probe signal power. Figure 6.18 shows pulsed Raman gain along the 100km sensing fibre produced by the Raman pump pulse.

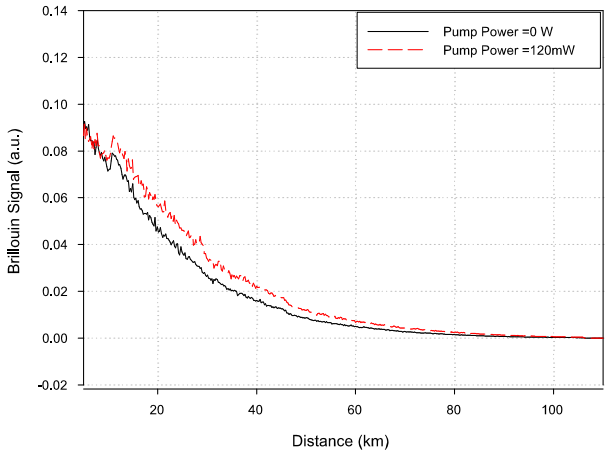

(a) *Brillouin signals with/without pulsed Raman amplification measured at peak frequency.*

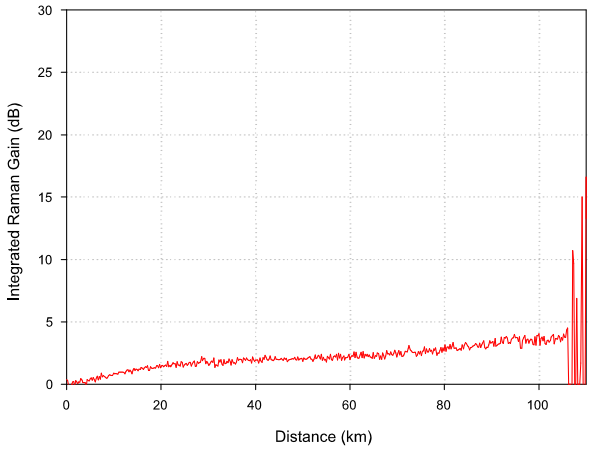

(b) *Integrated Raman gain in pulsed Raman amplification.*

Figure 6.18: *Integrated pulsed Raman gain along the sensing fibre for 80mW and 120mW probe and pump power, respectively.*

The Raman gain along the sensing fibre was obtained by taking the ratio of the amplified Brillouin signal to that of the Brillouin signal without Raman gain as shown in Figure

6.18(a). The average integrated Raman gain dependence on the pump power (∼120mW) was approximately 4dB at the end of the sensing fibre (Figure 6.18(b)), which is in close agreement with the Raman gain ratio obtained using the CW co-propagating technique (Page 149).

6.5.4 Discussion

The result of measuring temperature change with Brillouin frequency and power along the 100km sensing fibre using this technique reveals no significant improvements due to low pump power. However, the expected improvement corresponding to available pump power was achieved i.e. ∼3dB/100mW. It was concluded from this technique that the reduced power of the pulsed pump signal is the main limiting factor. However, this technique is anticipated to achieve significant improvement provided higher pump power is used to compensate for the pulsing loss.

6.6 50km Simultaneous Temperature and Strain Measurement Utilising Co-propagating Raman Pump Configuration

6.6.1 Introduction

Of the three techniques investigated, only two can be utilised if access is restricted to one end of the sensing fibre. Of these two, the CW co-propagating pump provided the most significant improvement in resolution using the Brillouin frequency shift. This section now explores temperature and strain resolutions that can be achieved over 50km using both the frequency and power measurement of the Brillouin signal in the presence of a CW co-propagating Raman pump.

6.6.2 Experimental Details and Measurements

The experimental arrangement for measuring temperature and strain simultaneously utilising co-propagating Raman amplification with CBS is shown in Figure 6.19.

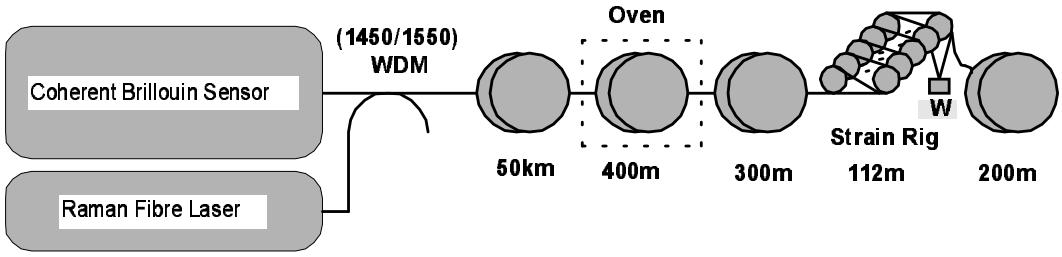

Figure 6.19: *Schematic diagram of the experimental set-up for measuring temperature and strain simultaneously using Raman amplification.*

The details of the experimental arrangement have been described in Section 6.3.2. However, the 980nm pump in the preamplifier was replaced by one with higher power. The Raman pump signal at 1450nm with ∼1.5nm linewidth and up to 1000mW of CW output power was coupled to the probe pulse using a 1450/1550nm wavelength division multiplexer. The sensing fibre was arranged as shown in Figure6.19. The first 50km remained on the original spools at room temperature. The next 400m was loosely coiled

and placed in an oven to allow heating whilst ensuring zero strain. The subsequent 300m were used as a reference and maintained at room temperature with zero strain. The following 112m section was passed around 8 pairs of pulleys and loaded with weights suspended at the end of the fibre. The last 200m was used as a second reference length and maintained at room temperature with zero strain. The Brillouin spectra were built from 20 separate backscatter traces, each averaged 2^{15} times, and taken every 10MHz, starting at 11.05GHz. Each individual spectrum was fitted to a Lorentzian curve to identify the peak of the Brillouin frequency shift. The Brillouin power was measured by numerical integration of the Brillouin spectral components and normalised using a measurement at room temperature/zero strain, to account for fibre/splice loss. The changes in the Brillouin frequency shift were also referenced to the room temperature/zero strain values. Using the previously ascertained values of temperature and strain coefficients governing frequency shifts and power change (Table 4.1), the temperature and strain along the sensing fibre can be written using equations 2.15 and 2.16, and the temperature and strain errors can be obtained using equations 2.17 and 2.18, respectively [10][11].

A 60 °C oven temperature and 1850$\mu\varepsilon$ strain were applied to the heated and strained sections, respectively. Distributed temperature and strain measurements were then made over a 50km sensing range, followed by detailed measurements around the heated and strained sections using the optimum probe and pump power combination (10mW and 1000mW respectively) with pulse widths of 50ns. Finally the Brillouin frequency shift and power were measured along the sensing length and the RMS errors evaluated every 10km over a distance of 500m and converted to the corresponding temperature and strain resolution.

6.6.3 Experimental Results

Figure 6.20 shows the measured Brillouin frequency shift and the measured Brillouin power along the sensor length of 50km using the co-propagating Raman pump configuration with optimised probe and pump power.

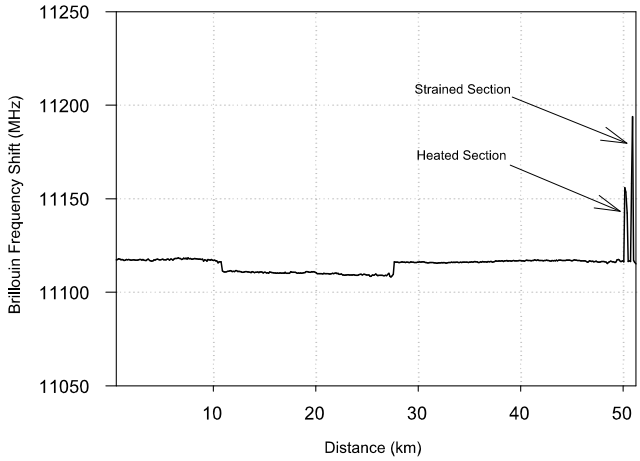

(a) *Brillouin frequency shift along the entire sensing fibre. Both the heated and strained sections are visible.*

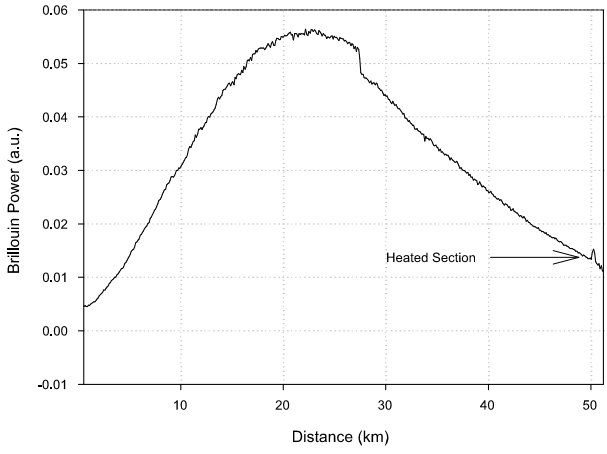

(b) *Brillouin power change along the entire sensing fibre. The heated section is visible 50km down the sensing fibre.*

Figure 6.20: *Brillouin frequency shift and power change over 50km sensing length with the presence of Raman gain.*

The frequency measurement in Figure 6.20(a) indicates the boundaries between different fibre sections, where the difference in frequency shift along the fibre at room temperature is attributed to differences in either the winding tension or intrinsic fibre properties. The frequency measurements show the shift due to both heating and strain close to the far end of the sensing fibre. The amplified power trace is shown with a maximum occurring

around 24km, as shown in Figure 6.20(b). It is evident that the signal power at the far end is greater than at the front end (∼3dB), showing that the Raman gain more than compensates for the two-way fibre loss of 20dB (50km×2×0.2dB/km).

Figure 6.21 shows an enlargement of the normalised frequency shift and power change at the heated and strained sections at the far end of the sensing fibre.

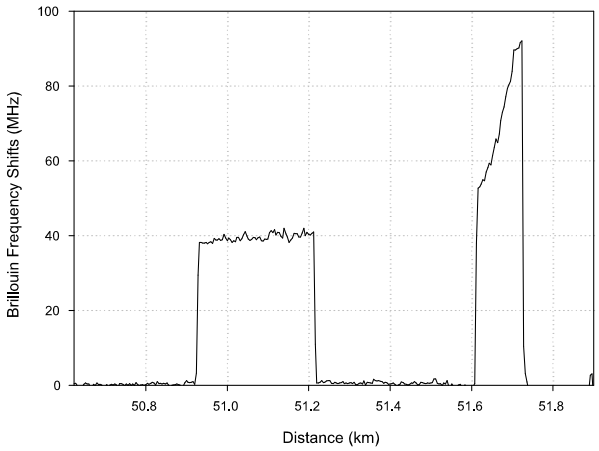

(a) *Brillouin frequency shift around the heated and strained sections.*

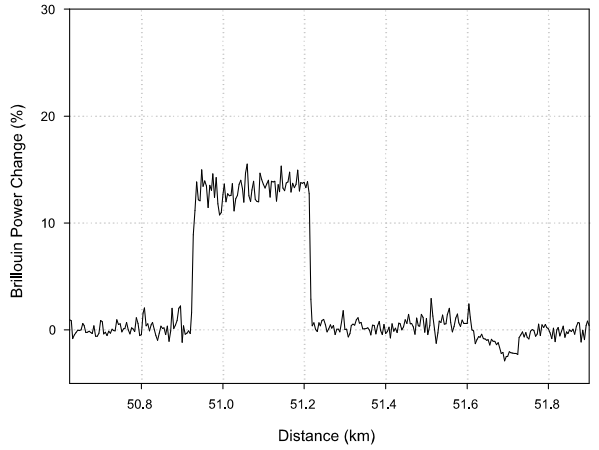

(b) *Normalised Brillouin power change around the heated and strained sections.*

Figure 6.21: *Referenced Brillouin frequency shift and normalised power change around both heated and strained sections at the far end of the sensing fibre.*

Using the normalised frequency shift and the percentage power change of figures 6.21(a) and 6.21(b) for the region around the heated and strained sections respectively. The derived temperature and strain profile were obtained using equations 2.15 and 2.16, as shown in Figure 6.22.

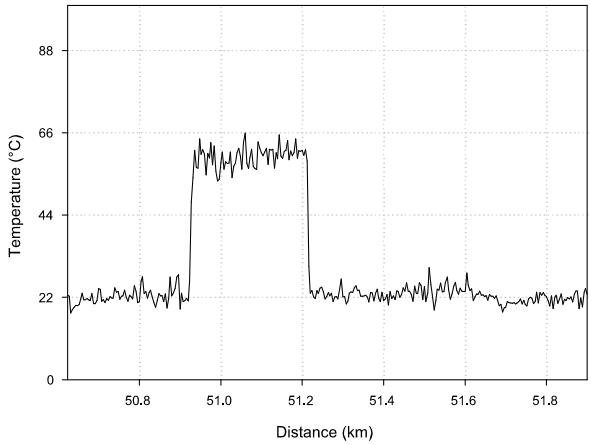

(a) *Derived temperature profile.*

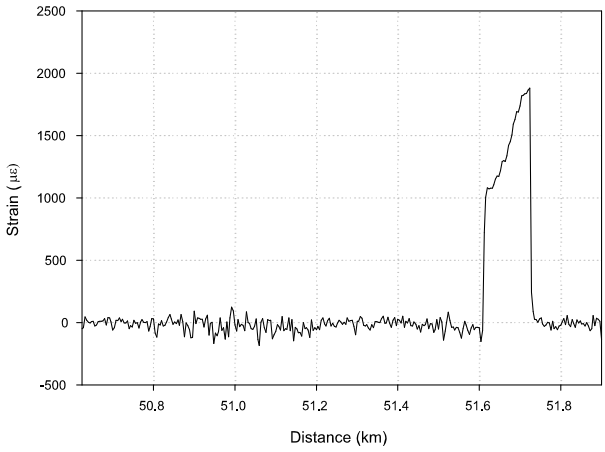

(b) *Derived strain profile.*

Figure 6.22: *Derived temperature and strain profiles based upon the measured data in Figure 6.21.*

The variation in strain over the strained region is attributed to the friction in the pulley system. It can be seen that there is a little cross-talk between strain and temperature. The RMS strain noise at the heated fibre (Figure 6.22(b)) is higher than the noise in the 300m reference fibre. The RMS noise on the frequency shift and the power traces over the heated section was measured, and the corresponding temperature and strain resolution, were calculated using equations 2.17 and 2.18, respectively.

A temperature resolution of ∼3.5 °C and a strain resolution of ∼85$\mu\varepsilon$ were calculated. The frequency and power resolutions along the fibre were also evaluated at 10km intervals, averaged over a length of 500m; these values were used to derive the temperature and strain resolutions, as shown in Figure 6.23.

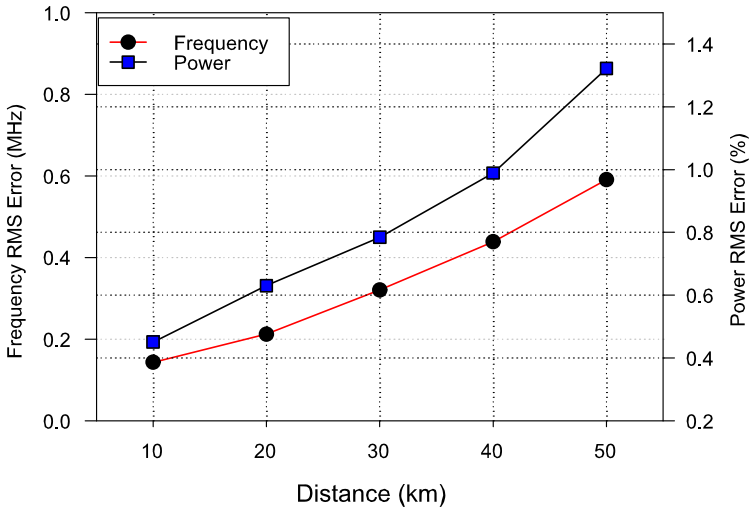

(a) *Brillouin frequency (left) and power (right) resolution.*

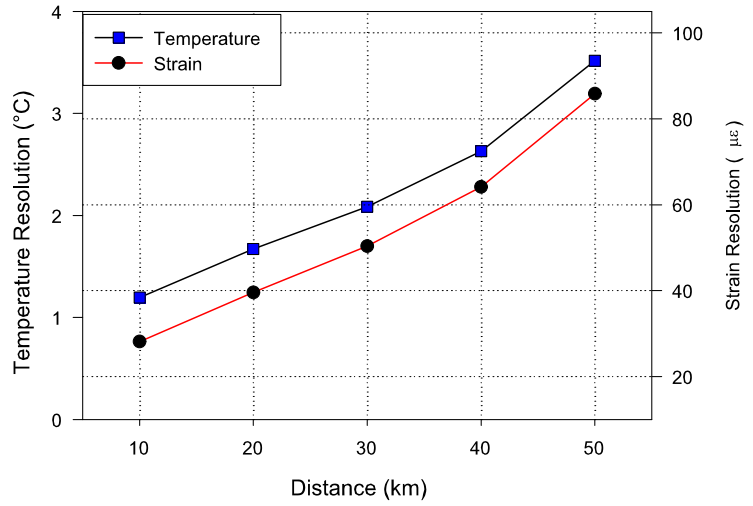

(b) *Temperature (left) and strain (right) resolution.*

Figure 6.23: *(a) Brillouin frequency and power RMS error taken every 10km over a range of 500m. (b) the corresponding temperature and strain resolutions based upon the measured data of figure 6.23(a).*

Figure 6.23(b) indicates temperature and strain resolutions of ∼1.5 °C and ∼40$\mu\varepsilon$, and ∼3.5 °C and ∼85$\mu\varepsilon$ at sensing lengths of 20km and at 50km, respectively. It can be seen clearly from Figure 6.23(b) that the two curves representing temperature and strain resolution follow the power RMS error curve shown in Figure 6.23(a). This indicates

clearly that the noise on the power trace is still responsible for more than 90% of the temperature and strain errors, which confirms the previous conclusion that power measurements remain the limiting factor on the accuracy of simultaneous temperature and strain measurements.

6.6.4 Discussion

In general, the sensing performance has been improved significantly using the co-propagating Raman pump configuration. The Raman pump amplifies both the outgoing probe pulse and the backscattered signal, leading to a significant improvement specially on the accuracy of the Brillouin power measurement. This technique benefits from combining the advantages of co-propagating optical Raman amplification, coherent detection and spontaneous Brillouin measurements, which led to the best results ever reported in terms of temperature and strain resolution, sensing range and spatial resolution. Furthermore it maintains the advantage of requiring access to just one end of the sensing fibre.

6.7 Combined Brillouin Frequency and Power Measurements Beyond 50km

The investigation of combined frequency and power measurements of the spontaneous Brillouin signal was then extended to cover a range up to 100km, and the merits of the investigated Raman pump configurations were quantified. The RMS frequency and power errors along the 100km, taken at 20km intervals and averaged over a length of 5km, were evaluated with/without Raman amplification at the optimum combination of probe and pump power with a spatial resolution of 20m. The RMS errors were obtained for the three Raman pump configurations and converted to the corresponding temperature errors. The results are shown in Figures 6.24 and 6.25, respectively, and summarised in Table 6.1.

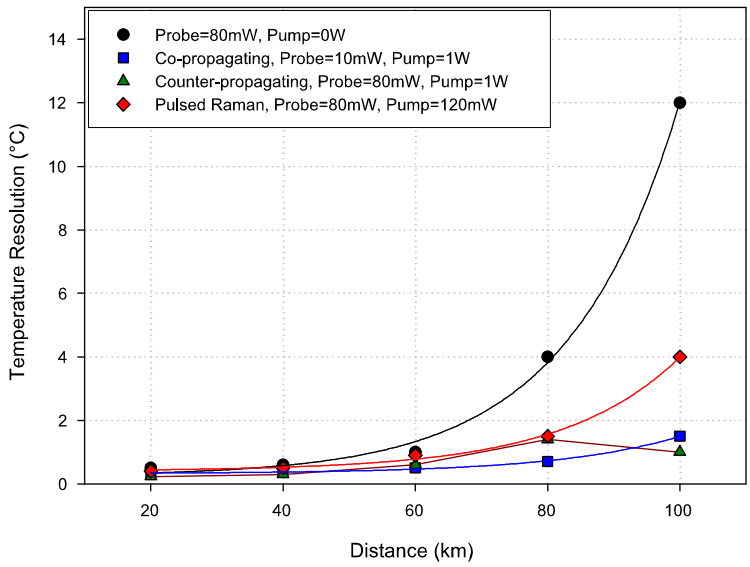

Figure 6.24: *Temperature resolution based on Brillouin frequency measurement along 100km using different Raman pump configurations.*

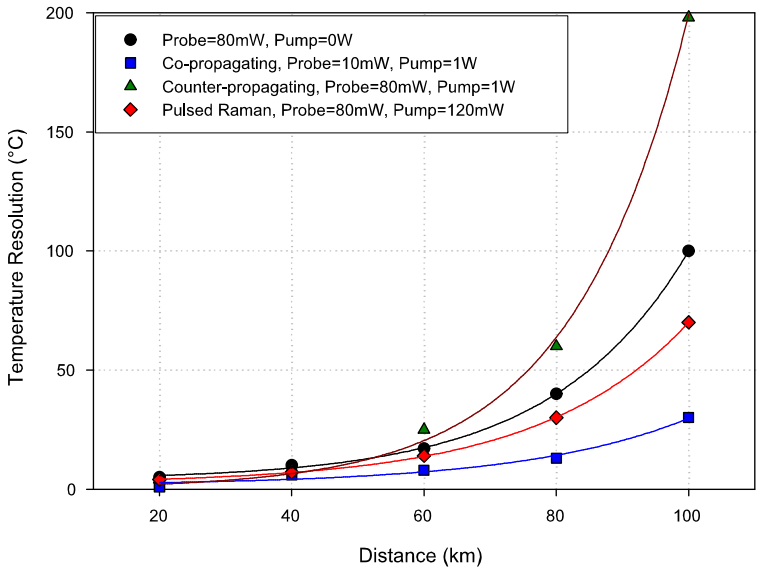

Figure 6.25: *Temperature resolution based on Brillouin power measurement along 100km using different Raman pump configurations.*

Table 6.1: *Equivalent temperature resolutions for frequency and power measurement of 100km using different Raman pump configurations. (Frequency=Frequency based measurements, Power=Power based measurements).*

Raman Pump Configuration	**Probe Power** (mW)	**Pump Power** (mW)	**Temperature Resolution** (*Frequency*) (°C)	**Temperature Resolution** (*Power*) (°C)
No Pump	80	0	12	100
Co-Propagation	10	1000	1.7	30
Counter-Propagation	80	1000	1	200
Pulsed Pump	80	120	4	75

In the co-propagating Raman pump configuration, the improvement on the temperature resolution was found to be around 7 fold compared to measurement without Raman amplification using Brillouin frequency shift, i.e. the temperature resolution improved from ∼12 °C to ∼1.7 °C, and with Brillouin power measurement, temperature reso-

lution improved from ∼100 °C to ∼30 °C. In the counter-propagating Raman pump configuration, using Brillouin frequency shift, the temperature resolution was ∼2 °C at 80km, and improved to less than 1 °C at 100km. However, the temperature resolution at 100km derived from the Brillouin power measurement was severely degraded from ∼100 °C to more than ∼200 °C. This is attributed to a combination of Raman amplifier noise and/or possible broadening effects due to the onset of MI, sufficient to distort the power measurement but still allowing accurate determination of the frequency measurement. These problems are circumvented by using the pulsed Raman pump technique, but because the attenuation produced by the AOM significantly restricted the Raman pulse power, only a moderate improvement was demonstrated: from ∼12 °C to ∼4 °C or ∼100 °C to ∼75 °C for the frequency and power measurements, respectively.

6.8 Conclusions

Distributed optical Raman amplification was explored and combined with the CBS to compensate for fibre loss, weakness of Brillouin signal and limited input pulse power. Using different configurations of Raman pump resulted in a significant improvement on sensing range and performance. In the co-propagating Raman pump configuration, the probe power needs to be reduced significantly to avoid nonlinear effects. Approximately 7 fold improvement on temperature resolution at 100km was achieved using Brillouin frequency measurements with 20m spatial resolution. This technique was used to measure temperature and strain simultaneously along 50km of SMF with 5m spatial resolution, where the best ever reported temperature and strain resolutions of $\sim$3.5 °C and $\sim 85\mu\varepsilon$ were achieved, respectively. An increase in the dynamic range of approximately 30dB in the counter propagation case was achieved, which equates to an increase in sensing range of approximately 75km using Brillouin frequency shift based measurements. A temperature resolution of 5 °C at a 150km sensing range, and better than 1 °C at a 100km sensing range were achieved with a spatial resolution of 50m and 20m, respectively. However, at higher pump power, temperature resolution based on Brillouin power measurement was severely degraded due to nonlinear effects. The performance improvement using the delayed pulse Raman pump technique was limited by the reduced pump power available as a consequence of modulator loss. The CW co-propagating Raman pump configuration is relatively simple and provides an effective means to extend the range of such a sensor. It maintains the advantage of requiring access to only one end of the sensor.

Bibliography

[1] Y. Sun, J. W. Sulhoff, A. K. Srivastave, J. L. Zyskind, T. A. Strasser, J. R. Pedrazzani, C. Wolf, J. Zhou, J. B. Judkins, R. P. Espindola and A. M. Vengsarkar, "80nm Ultra-wideband Erbium-doped Silica Fiber Amplifer," *Electronics Letters*, vol. 33, no. 22, p. 1965, November 1997.

[2] N. A. Olsson and J. P. Van Der Ziel, "Characteristics of a Semiconductor Laser Pumped Brillouin Amplifier with Electronically Controlled Bandwidth," *IEEE Journal of Lightwave Technology*, vol. LT-5, no. 1, p. 147, January 1987.

[3] D. M. Spirit and L. C. Blank, "Raman Assisted Long Distance Optical Time Domain Reflectometry," *Electronics Letters*, vol. 25, no. 25, p. 1687, December 1989.

[4] Y. T. Cho and T. P. Newson, "Brillouin-Based Distributed Fibre Temperature Sensors at 1.53 μm Using Raman Amplification," *15^{th} International Conference on Optical Fiber Sensors Technical Digest (OFS)*, p. 305, May 2002.

[5] H. S. Seo, K. Oh, "Optimization of silica fiber Raman amplifier using the Raman frequency modeling for an arbitrary GeO_2 concentration in the core'," *Optics Communications*, vol. 181, p. 145, 2000.

[6] G. P. Agrawal, *Nonlinear Fiber Optics*, 2nd ed. Academic Press, 1995.

[7] Y. T. Cho, "An Investigation into Using Optical Amplifiers for Enhancing Brillouin Based Optical Time Domain Reflectometry," PhD Thesis, University of Southampton, 2004.

[8] H. H. Kee, G. P. Lees and T. P. Newson, "Extended Range Optical Time Domain Reflectometry System at 1.65 μm Based on Delayed Raman Amplification," *Optics Letters*, vol. 23, no. 5, p. 349, March 1998.

[9] Y. T. Cho, M. N. Alahbabi, M. J. Gunning and T. P. Newson, "50 km Single-Ended Spontaneous Brillouin-Based Distributed Temperature Sensor Exploiting Pulsed Raman Amplification," *Optics Letters*, vol. 28, no. 18, p. 1651, September 2003.

[10] S. M. Maughan, H. H. Kee and T. P. Newson, "Simultaneous Distributed Fibre Temperature and Strain Sensor using Microwave Coherent Detection of Spontaneous Brillouin Backscatter," *Measurement Science and Technology*, vol. 12, p. 834, February 2001.

[11] J. D. C. Jones, "Review of Fibre Sensor Techniques for Temperature-Strain Discrimination," *12th International Conference on Optical Fiber Sensors Technical Digest (OFS)*, vol. 16, p. 36, October 1997.

Chapter 7

Conclusions

7.1 Summary of Thesis

This thesis has presented both theoretical and experimental research work on maximising the range and improving the sensing performance of Brillouin based distributed temperature and strain optical sensors, based on the coherent detection of spontaneous Brillouin scattering. It was the principal aim of this research to address the factors that limit performance in order to surpass previous achievements in sensing range, measurand resolution, spatial resolution and overall sensing performance, and this has been achieved. The work done and results achieved are now summarised.

An optimisation of the CBS was performed, where around 15dB improvement on the Brillouin backscattered power was achieved. Along with improvement of the backscattered signal, its measurement and processing methods were investigated and optimised accordingly. This has led to a longer sensing range and better measurand resolutions with less averaging time compared to the previous system. In spite of ASE reduction through the gating process and with the currently available components, the main source of system noise has been identified as the ASE noise generated from the preamplifier, which is crucial to sensor set-up. However, with good optical filtering, such noise may be reduced.

Using the optimised sensor and its new microwave detection system, a high spatial resolution (2m) temperature measurement over 30km of SMF with temperature error of less than 1.6 °C was achieved. The optimised sensor along with its microwave detection system was also used for the first time to characterise the Brillouin spectrum in special fibres designed and fabricated to suppress SBS in high power fibre laser systems. Such a measurement opens the way for new applications of this sensor.

Brillouin power measurement limits the range and accuracy of simultaneous temperature and strain measurements. As a result, two other techniques for separating the measurands simultaneously over 23km sensing range, while avoiding Brillouin power measurements, were investigated and compared. These utilise frequency analysis of fibre exhibiting multiple peaks and a combined Raman power and Brillouin frequency measurement in standard fibre. At present, neither technique offers any advantage over the Brillouin frequency and power measurement technique, but there is scope for improvement.

Spontaneous Brillouin power is proportional to the input pulse energy. An investigation of the nonlinear effects that limit pulse power were conducted. Stimulated Brillouin scattering occurs at significantly higher optical powers than SRS, with threshold powers of the order of some watts for SBS compared to hundreds of milliwatts for SRS for a pulse <390ns. For a pulse width of ∼25ns, self-phase modulation occurs at relatively lower power compared to both SRS and SBS. Modulation instability was found to have the lowest threshold in standard SMF exhibiting positive dispersion at 1550nm. However, by using NZ-DSF MCF which has negative dispersion at 1550nm, the MI effect is avoided, hence higher input power up to ∼900mW can be safely used, where longer sensing range and better sensing performance are expected, but at the expense of using special fibres.

To improve the performance of sensors using SMF, the possibility of using Raman amplification was investigated. Different configurations of optical Raman pump were originally investigated with the CBS. It was found that with a co-propagating Raman pump configuration, the probe power needed to be reduced to avoid nonlinear effects, such as MI. The optimum probe and pump power for 100km sensing range measurements was found to be ∼10mW and ∼1W, respectively. Improvements of 7 and 3 fold on temper-

ature resolution based on Brillouin frequency and power measurements were achieved respectively. Using a co-propagating pump configuration, simultaneous measurement of temperature and strain was carried out along 50km, with 3.5°C and 85$\mu\varepsilon$ temperature and strain resolutions achieved respectively, with 5m spatial resolution, the best result ever reported. In the counter-propagating Raman pump configuration, the frequency based measurement was improved significantly, but the Brillouin power sensitivity to temperature was degraded due to MI and/or Raman ASE. Using the Brillouin frequency shift, distributed temperature measurements were carried out for a sensing range up to 150km, with a probe and pump power of ∼80mW and 1W, respectively. At ∼100km the temperature resolution was better than 1°C, with 20m spatial resolution, and at 150km, 5°C temperature resolution was achieved with spatial resolution of 50m. A pulsed Raman technique was investigated but the reduced pump power due to Raman pulsing limited the performance.

Combining Raman amplification with the coherent detection of spontaneous Brillouin scattering demonstrates significant improvement on sensing range and accuracy.

7.2 Future Work

Research and work on optical Brillouin based distributed temperature and strain sensors has focused on the optimisation of sensor performance in terms of sensing range, spatial resolution, temperature and strain resolution, measurement time, reliability and cost. Further improvements on CBS are possible by researching the following:

Negative Dispersion Fibres for Long Range Distributed Sensors

As expected, MCF shows no signs of modulation instability, which suggests that higher powers can be safely used. The next nonlinear threshold is expected to be SRS. This needs to be investigated further, but an order of magnitude improvement in pulse energy is possible.

Preamplifier and LO Noise

The major source of sensor noise was ASE coming from the EDFA preamplifier. Future use of optical filtering is required. For example, a narrow optical filter (∼2GHz of Bandwidth) will reduce the noise by around 9dB compared to the current BG filter (∼15GHz Bandwidth). Additional narrow optical filters may be used to filter Raman ASE. At present the LO noise is below the noise level of the preamplifier noise. However, if the preamplifier noise is reduced, then LO noise needs to be investigated.

Higher Raman Pump Power

If a Raman pump source with higher power is used, the sensing performance is expected to improve further, i.e. with the co-propagating pump configuration the Raman pump power could be higher than 1W, with reduced probe power <10mW, and with a pulsed Raman pump technique, higher pump power can be launched into the sensing fibre, giving longer sensing range and better sensing performance.

Data Processing

With the current data acquisition system, data measurement and processing currently takes more time than necessary. Theoretically, the time for complete measurement and data analysis of a 100km fibre could be reduced by at least an order of magnitude, using a faster data acquisition system.

Temperature and Strain Measurements with Higher Spatial Resolution

The microwave detection system can recover a signal with a pulse width greater than ∼10ns (∼1m spatial resolution). For higher spatial resolution measurements the 1GHz BPF bandwidth needs to be increased along with the use of a faster response time RF rectifier.

Remote Amplification

Some preliminary investigation of Remote amplification has been made, remotely sited erbium or Raman amplifiers have been recently implemented by the group, initially using the direct detection technique. This should now be explored further using the advantages of coherent detection.

7.3 Key Achievements

This thesis has researched methods to improve sensing range and performance of coherent Brillouin based distributed temperature and strain sensors. The main achievements are:

- Simplification and optimisation of the CBS. This has led to an improvement of about 15dB on the Brillouin backscattered power, which led to a longer sensing range and improved sensing performance.
- Demonstration of a new microwave detection system for long range measurement with high spatial resolution, with 1.6 °C over a range of 30km and 2m spatial resolution was achieved.
- Demonstration of the use of the high spatial resolution sensor for the first time to characterise special fibres designed and fabricated to suppress SBS.
- Demonstration for the first time of the feasibility of using combined Raman power and Brillouin frequency to measure temperature and strain simultaneously.
- Identification of the best technique to measure temperature and strain simultaneously for a sensing range >30km.
- Identification of modulation instability as the nonlinear effect with the lowest power threshold, demonstrating that it can be avoided by using NZ-DSF MCF.
- Demonstration for the first time of the use of optical Raman amplification with the coherent detection Brillouin based sensor, where a temperature measurement over 150km was demonstrated, the longest distributed temperature sensing range ever reported.
- Demonstration of the longest single ended sensing range of simultaneous measurement of temperature and strain (50km) with the best measurand and spatial resolution ever reported over such a range.

The results achieved represent a significant advance in distributed temperature and strain Brillouin based sensors.

Appendix A

List of Publications

A.1 Journal Papers

1. M. N. Alahbabi, Y. T. Cho and T. P. Newson, "Simultaneous Measurement of Temperature and Strain Over 50km using Spontaneous Brillouin Scattering and Raman Amplification". *Submitted to Measurement Science and Technology*, June 2005.

2. M. N. Alahbabi, Y. T. Cho and T. P. Newson, "Fiber Sensor Utilizes Both Raman and Brillouin Scattering". *Will be published in the Photonics Spectra Magazine*, July/August 2005.

3. M. N. Alahbabi, Y. T. Cho and T. P. Newson, "Simultaneous Temperature and Strain Measurements using Combined Spontaneous Raman and Brillouin Scattering". *Optics Letters*, vol. 30, no. 11, p. 1276, June 2005.

4. M. N. Alahbabi, Y. T. Cho and T. P. Newson, "150km Range Distributed Temperature Sensor Based on Coherent Detection of Spontaneous Brillouin Backscatter and in Line Raman Amplification". *Journal of the Optical Society of America B (JOSA B)*, vol. 22, no. 6, p. 1321, June 2005.

5. Y. T. Cho, M. N. Alahbabi, G. Brambilla and T. P. Newson, "Distributed Raman Amplification Combined with a Remotely Pumped EDFA Utilized to Enhance the Performance of Spontaneous Brillouin-based Distributed Temperature Sensors". *IEEE Photonics Technology Letters*, vol. 17, no. 6, p. 1256, June 2005.

6. M. N. Alahbabi, P. C. Wait,Y. T. Cho, A. H. Hartog and T. P. Newson, "Influence of Modulation Instability on Distributed Optical Sensors Based on Spontaneous Brillouin Scattering". *Journal of the Optical Society of America B (JOSA B)*, vol. 21, no. 6, p. 1156, June 2004.

7. M. N. Alahbabi, Y. T. Cho and T. P. Newson, "100km Distributed Temperature Sensor Based on Coherent Detection of Spontaneous Brillouin Backscatter". *Measurement science and Technology*, vol. 15, no. 8, p. 1544, August 2004.

8. M. N. Alahbabi, N. P. Lawrence, Y. T. Cho, and T. P. Newson, "High Spatial Resolution Microwave Detection System for Brillouin-Based Distributed Temperature and Strain Sensors". *Measurement science and Technology*, vol. 15, no. 8, p. 1539, August 2004.

9. Y. T. Cho, M. N. Alahbabi, M. J. Gunning and T. P. Newson, "Enhanced Performance of Long Range Brillouin Intensity Based Temperature Sensors Using Remote Raman Amplification". *Measurement Science and Technology*, vol. 15, no. 8, p. 1548, August 2004.

10. M. N. Alahbabi, Y. T. Cho and T. P. Newson, "Comparison of the Methods for Discriminating Temperature and Strain in Spontaneous Brillouin-based Distributed Sensors". *Optics Letters*, vol. 29, no. 1, p. 26, January 2004.

11. Y. T. Cho, M. N. Alahbabi, M. J. Gunning and T. P. Newson, "50-km Single-ended Spontaneous Brillouin-based Distributed Temperature Sensor Exploiting Pulsed Raman Amplification". *Optics Letters*, vol. 28, no. 18, p. 1651, September 2003.

A.2 Conference Presentations

12. M. N. Alahbabi, Y. T. Cho and T. P. Newson, "50km Simultaneous Distributed Temperature and Strain Measurements Based on Coherent Detection of Spontaneous Brillouin Backscatter and Raman Amplification". *The 17th International Conference on Optical Fiber Sensors*, p. 84, May 2005.

13. Y. T. Cho, M. N. Alahbabi, G. Brambilla and T. P. Newson, "Distributed Raman Amplification Combined with a Remotely Pumped EDFA Utilized to Enhance the Performance of Spontaneous Brillouin-based Distributed Temperature Sensors". *The 17th International Conference on Optical Fiber Sensors*, p. 72, May 2005.

14. M. N. Alahbabi, Y. T. Cho and T. P. Newson, "Simultaneous Distributed Measurements of Temperature and Strain Using Spontaneous Raman and Brillouin Scattering". *Second European Workshop on Optical Fiber Sensors (EWOFS)*, SPIE Vol. 5502, p. 488, June 2004.

15. M. N. Alahbabi, Y. T. Cho and T. P. Newson, "Comparison Between Standard SMF and Non-Zero Dispersion Shifted Fibre LEAF for Long Range Simultaneous Temperature and Strain Measurements". *Second European Workshop on Optical Fiber Sensors (EWOFS)*, SPIE Vol. 5502, p. 484, June 2004.

16. Y. T. Cho, M. N. Alahbabi and T. P. Newson, "Brillouin-based OTDR with Measurement Range of 85km Using Combined EDFA and Raman Amplification". *Conference of Lasers and Electro-Optics Technical Digest (CLEO)*, CWM5, May 2004.

17. M. N. Alahbabi, N. P. Lawrence, Y. T. Cho and T. P. Newson, "High Spatial Resolution Microwave Detection System for Long Range Brillouin-Based Distributed Sensors". *The 16th International Conference on Optical Fiber Sensors*, p. 334, October 2003.

18. M. N. Alahbabi, Y. T. Cho and T. P. Newson, "100km Distributed Temperature Sensor Based on Coherent Detection of Spontaneous Brillouin Back-scatter". *The 16th International Conference on Optical Fiber Sensors*, p. 338, October 2003.

19. Y. T. Cho, M. N. Alahbabi, M. J. Gunning and T. P. Newson, "Enhanced Performance of Long Range Brillouin Intensity Based Temperature Sensors Using Remote Raman Amplification". *The 16th International Conference on Optical Fiber Sensors*, p. 392, October 2003.

20. M. N. Alahbabi, Y. T. Cho and T. P. Newson, "81km Temperature Sensor Based on Spontaneous Brillouin Scattering and Coherent Detection". *PHOTONEX 03-UOMRS*,UK, ORC Database, no. 2720, May 2003.

21. M. N. Alahbabi, Y. T. Cho and T. P. Newson, "Long Range Temperature Sensor Based on Brillouin Frequency Shift". *PREP2003*, p. 73, April 2003.